

RIKAGAKU KENKYUSHO

the Institute of Physical and Chemical Research

Yamato-machi, Saitama Pref., JAPAN

'67

IPCR cyclotron
Progress Report 1967

Vol. 1

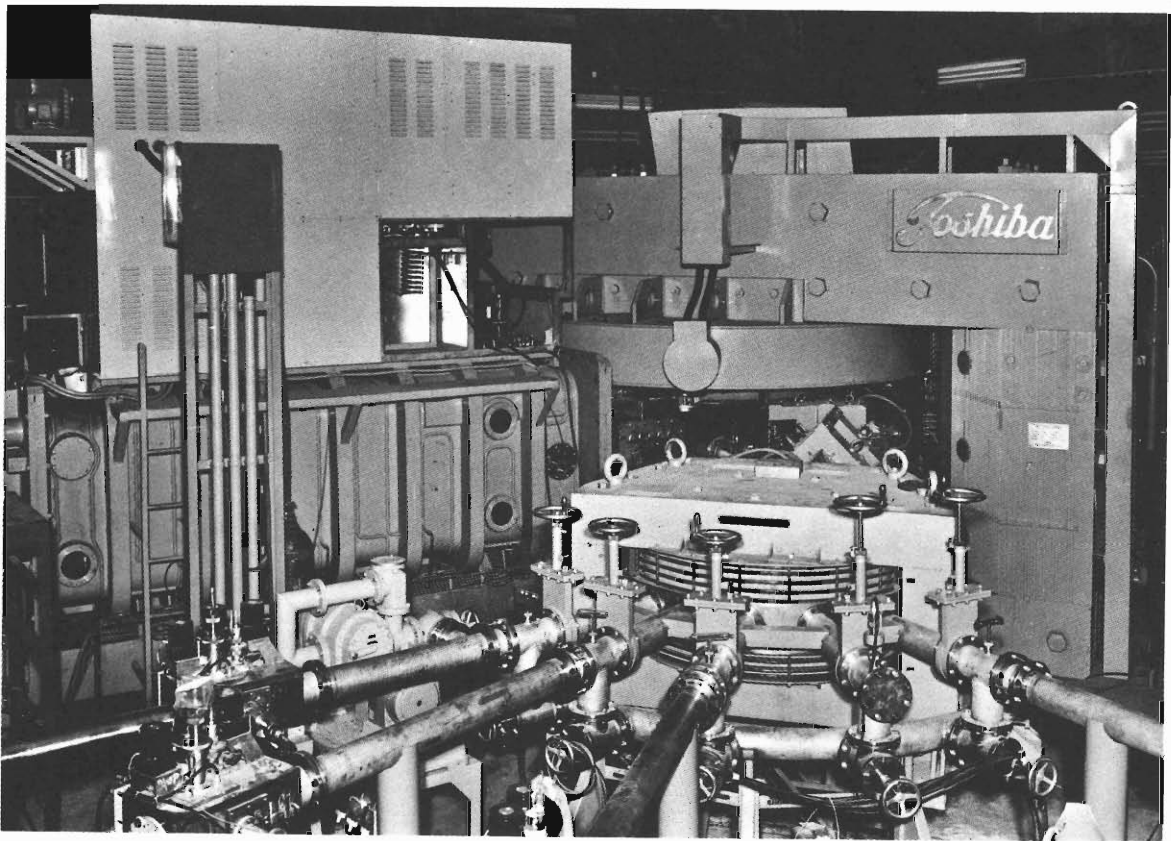
Edited by Administration Committee of the IPCR Cyclotron

IPCR Cyclotron Progress Report 1967

Vol. 1

The Institute of Physical and Chemical Research
"RIKAGAKU KENKYUSHO" Yamato-machi, Saitama Pref., JAPAN
November, 1967

Dedicated to the Memory of
Dr. Yoshio NISHINA
(1890~1951)



The cyclotron. The yoke of magnet is seen on the right and the oscillator on the left. On the foreside of the photo the beam switching magnet and five courses of beam pipe are seen.

All rights reserved. This report or any part thereof may not be reproduced in any form (including photostatic or microfilm form) without written permission from the publisher.

CONTENTS

	Page
1. INTRODUCTION	1
2. MACHINE OPERATION	2
3. MACHINE DEVELOPMENT	4
3-1. Outline of the IPCR Cyclotron	4
3-2. Beam focusing System	10
3-3. Circulation System of ^3He Gas	13
3-4. On the Multicharged Heavy Ion Source	16
3-5. Design of the focusing Magnetic Channel	19
4. ACCELERATOR PHYSICS	25
4-1. Initial Motion of Ions	25
4-2. Investigation on Electromagnets	29
Hysteresis Effect of Field Distribution	
5. NUCLEAR PHYSICS	33
Scattering and Reaction	
5-1. The $^{27}\text{Al}(^3\text{He}, ^3\text{He})^{27}\text{Al}$ and $^{27}\text{Al}(^3\text{He}, \alpha)^{26}\text{Al}$ Reaction	33
5-2. Elastic and Inelastic Scattering of ^3He from Ni Isotopes	37
5-3. Elastic Scattering of ^3He from Ca	41
5-4. Coulomb Excitation with Alpha-particles	44
6. NUCLEAR PHYSICS	50
Nuclear Spectroscopy and its Applications	
6-1. Measurements of Internal Conversion Electrons	50
6-2. Nuclide Analysis using Nuclear Reactions	53

7.	NUCLEAR INSTRUMENTATIONS AND TECHNIQUES	54
7-1.	The 75 cm Scattering Chamber	54
7-2.	An Air-core Beta-ray Spectrometer	58
7-3.	A Broad Range Magnetic Analyzer	60
7-4.	Data Processing System	62
7-5.	A Charge Spectrometer	65
8.	RADIOCHEMISTRY	66
8-1.	Charged-particle Activation Analysis	66
8-2.	Recoil Chemistry	67
9.	RADIATION CHEMISTRY AND RADIATION BIOLOGY	70
9-1.	LET Effects in the Radiation Chemistry and Radiation Biology	70
10.	SOLID STATE PHYSICS	72
10-1.	Radiation Damage in Solids	72
11.	RI PRODUCTION AND ITS APPLICATIONS	73
11-1.	The Irradiation System	73
11-2.	Safe Handling of irradiated Targets	75
11-3.	Preparation and Isolation of Carrier-free ^{76}As from ^{78}Se	76
11-4.	Preparation of ^{18}F -labelled Compounds	77
12.	RADIATION MONITORING	81
12-1.	Radiation Monitoring Station	81
12-2.	Health Physics	83
13.	LIST OF PERSONNEL	87

Fig. 1 (3-1)	Scheduled range of particle energy of the IPCR cyclotron	6
Fig. 2 (3-1)	Final field distributions obtained by the measurement with model magnets	7
Fig. 3 (3-1)	Magnet and acceleration chamber	8
Fig. 4 (3-1)	Oscillator and stem tank	9
Fig. 1 (3-2)	Layout of the beam transport	12
Fig. 1 (3-3)	The diagram of the circulation system	14
Fig. 2 (3-3)	The diagram of gas flow	15
Fig. 1 (3-4)	Ion source and block diagram for power supply	16
Fig. 2 (3-4)	Ion source for bench test	17
Fig. 3 (3-4)	Spectrum of nitrogen ion beam from nitrogen gas discharge ...	18
Fig. 4 (3-4)	Spectrum of oxygen and carbon ion beam from CO ₂ discharge	18
Fig. 1 (3-5)	Measured beam spread and the expected focusing effect of the channel	21
Fig. 2 (3-5)	Field induced by an infinitely long bar ($\mu = \infty$) placed in the uniform magnetic field	22
Fig. 3 (3-5)	(a) Schematic diagram of the focusing channel	23
	(b) Field distribution in the median plane of 1/3 scale magnetic channel	23
Fig. 4 (3-5)	The design of channel indicating the position adjusting mechanism	24
Fig. 1 (4-1)	The central cyclotron region, showing the ion source, feeler, and dees	26
Fig. 2 (4-1)	(a) The case of west dee injection. (b) The distance from the ion source to the first turn vs. the normalized dee voltage	27

Fig. 3 (4-1)	Beam density vs. radius. (a) In the case of west dee injection. (b) In the case of east dee injection	28
Fig. 1 (4-2)	General view of the switching and analyzing magnets for the IPCR cyclotron beam	30
Fig. 2 (4-2)	Variation of the field distribution along the beam path in air gap depending on the cases of increasing and decreasing the field strength	31
Fig. 3 (4-2)	Improvement on the field distribution by attaching the iron pieces to an edge of the pole	32
Fig. 1 (5-1)	Pulse height spectra of ^3He and α -particles obtained at $\theta_{\text{lab.}} = 30^\circ$ from the bombardment of ^{27}Al with 24.2 MeV ^3He particles	34
Fig. 2 (5-1)	Angular distribution, expressed as σ / σ_R , for the elastic scattering of 24.2 and 31.5 MeV ^3He particles	35
Fig. 3 (5-1)	Angular distribution of α -particles for the $^{27}\text{Al}(^3\text{He}, \alpha)^{26}\text{Al}$ reaction leaving ^{26}Al in the ground and third excited states ...	36
Fig. 1 (5-2)	Angular distribution of the elastic scattering	38
Fig. 2 (5-2)	Pulse height spectrum	39
Fig. 3 (5-2)	Angular distribution of the inelastic scattering	40
Fig. 1 (5-3)	Angular distribution of the elastic scattering	42
Fig. 2 (5-3)	A preliminary fit of the angular distribution	43
Fig. 1 (5-4)	Gamma-ray spectrum of ^{181}Ta	46
Fig. 2 (5-4)	Gamma-ray spectrum of Ag	47
Fig. 3 (5-4)	Gamma-ray spectrum of ^{197}Au	48
Fig. 4 (5-4)	Energy levels in ^{197}Au	49
Fig. 1 (6-1)	Momentum spectrum of the conversion electrons from ^{198}Au	52
Fig. 1 (7-1)	Sectional view of chamber	55
Fig. 2 (7-1)	Side view of chamber	56

Fig. 3 (7-1)	Top view of chamber	57
Fig. 1 (7-3)	Upper drawing shows a designed magnetic field configuration in the median plane of magnets and typical particle trajectories. In the lower side calculated values are tabulated	61
Fig. 1 (7-4)	DDP-124 PHA system configuration	64
Fig. 1 (9-1)	Relation between optical density (Fe^{3+}) and total charge input	71
Fig. 1 (11-1)	Irradiation system for RI production	74
Fig. 1 (11-4)	Thick-target saturation activities for the $^{16}\text{O} + \alpha \longrightarrow ^{18}\text{F}$ and the $^{16}\text{O} + ^3\text{He} \longrightarrow ^{18}\text{F}$ reactions in O_2	78
Fig. 2 (11-4)	Equipment for preparing anhydrous HF^{18} by charged particle bombardment of an oxygen stream	79
Fig. 3 (11-4)	Elution curve of H^{18}F from a silver bombardment vessel	80
Fig. 1 (12-1)	Record of radiation monitoring at the station 85m apart from the cyclotron	82
Fig. 1 (12-2)	Machine leakage radiation (neutron and gamma)	85
Fig. 2 (12-2)	Residual activity pattern (I)	86
Fig. 3 (12-2)	Residual activity pattern (II)	86

1. INTRODUCTION

Before the World War II, two cyclotrons of 26" and 60" were constructed in IPCR, the abbreviated name of the Institute of Physical and Chemical Research, "RIKAGAKU KENKYUSHO" in Japanese.

In those days the 60" cyclotron was the largest in the Far East. The old IPCR cyclotron of 26" was first successfully operated in 1937 under the supervision of the late Dr. Yoshio Nishina, and since then an extensive program of experimental researches by use of this device had been launched. Just after the War, both machines were destroyed and thrown into the Tokyo Bay by the occupation army.

In 1952 a small cyclotron of 26" was reconstructed and we began our research works on a small scale. A larger cyclotron of 63" was constructed on a new site when our institute was moved to Yamato-machi, Saitama Prefecture, Japan, about 13 km distant from the old site, Honkomagome, Tokyo. We started operation of the new machine from the fall of 1966.

The new machine is an ordinary type cyclotron capable of accelerating various particles to a wide range of energy and particularly useful for accelerating heavy ions. The subjects of research using this cyclotron are not only related to nuclear physics, but also cover a wide field of science, namely, radiochemistry, radiation chemistry, radiation biology, solid-state physics and radioisotope production.

The first volume of IPCR Cyclotron Progress Report reviews the present status of the new cyclotron in general and contains the summaries of research, technical development and other activities involving the cyclotron, which were carried out from January to June, 1967. The cyclotron was operated as a research tool for the members of our institute during this period. The operation of the machine is undertaken by the Administration Committee of the IPCR cyclotron.

The construction of the machine was supervised by the Cyclotron Construction Committee of this institute (Chairman: Dr. Hiroo Kumagai). The financial support for the construction of machine and the research works were mainly given by the Government. Here, we should like to express our thanks to those who backed up the project of the IPCR cyclotron.

Acknowledgment must also be made to the members of the Japan Atomic Energy Committee, and Mr. Haruo Nagaoka, former President of the Institute, without whose continued support and interest the IPCR cyclotron could not have been realized.



Fumio Yamasaki, Chairman
Administration Committee of
the IPCR Cyclotron

2. MACHINE OPERATION

The first beam was obtained from the IPCR cyclotron on Oct. 4, 1966. The beam of N^{4+} was accelerated to 56 MeV and deflected on Jan. 12, 1967, whose intensity at the exit radius was about $5 \mu A$. Since Feb. 6, 1967, the cyclotron has been used for research works. There occurred no serious fault but some minor failures were found and repaired. These are:

- (1) Vacuum discharge which was mainly caused by the soft solder on the part of liner.
- (2) RF voltage breakdown at the shorting bar.
- (3) Mechanical failure at the moving parts of the liner and the shorting bar. (See 3-2.)
- (4) Gas discharge at some undesirable portions in the ion source and in its feeder.

The beam energy and the beam intensity have not yet reached the target values. The maximum conditions now attained are: the alpha-particle energy is 40 MeV and the deflected current of 3He is about $30 \mu A$. There are several points which must be improved; one is the vacuum spark of RF voltage which limits the dee-ground peak voltage under 100 kV, while its target value being 130 kV, and the other is the mismatching between the deflected beam and the beam transport system. Beams travel through a long path (about 115°) in the fringing field of the B-constant magnet and neither magnetic nor electric channel device is applied. This design was adopted to facilitate the beam extraction under a wide range of the magnetic field strength ($0.5 \sim 2 \text{ Wb/m}^2$). It caused, however, a remarkable spread of horizontal beam divergence, and only about 20% of deflected beam was caught by the beam transport system. To solve this problem, a magnetic channel which might be used over the wide range of field strength was designed (See 3-5). The source of heavy ion (See 3-4) was operated successfully. This has, however, not yet been used for research works, because the stability is not so reliable as to operate continuously under the cyclotron condition. For about a half of the running time, 3He ions are accelerated and their energy covers from 12 MeV to 40 MeV. The performance of gas circulation system is good and the intensity of analyzed 3He beams is enough for the nuclear scattering experiment (See 3-2, 5-1, 5-2, and 5-3).

The machine is operated on a 2 shifts 24 hours per day system. Every two weeks or every month, the operating schedule is planned. Scheduled running days and available days for each research subject, and days used for maintenance are given in Table 1 (2). Of these subjects, only the alpha-particle beam of 11 MeV for the Coulomb excitation study was difficult to obtain. For the other subjects, however, no serious problem on beam intensity nor on beam quality remained at the last stage of this period. Since the available machine time, which includes the time needed for the beam handling, was about 80% as shown in Table 1 (2), a more efficient use of research group is desirable.

Table 1 (2).

Machine time from Feb. 6 to July 12 (Total 157 days)

	Subjects	Days scheduled	Days available
5-1	$^{27}\text{Al}({}^3\text{He}, \alpha)$	23	21
5-2	$^{58,60}\text{Ni}({}^3\text{He}, {}^3\text{He}')$	21	19
5-3	$\text{Ca} + {}^3\text{He}$	18.5	16
5-4	Coulomb excitation	10	5
6-1	Nuclear spectroscopy	4.5	3
7 and 11	Radiochemistry and radioisotope production	8	7
9-1	LET effects	6	6
10-1	Radiation damage	1	1
6-2	Analysis of nuclide	1.5	1.5
4-1	Initial motion	12	12
3	Machine development	14	14
	Maintenance	13	13
	And others	9.5	
	Total	142	118.5 (83.5%)

3. MACHINE DEVELOPMENT

3-1. Outline of the IPCR Cyclotron

The cyclotron¹⁾ was installed at the Institute of Physical and Chemical Research, (RIKAGAKU KENKYUSHO, Yamato-machi, Saitama Prefecture, Japan). The design is an extension of the variable energy ordinary cyclotron at the Institute for Nuclear Study (INS), the University of Tokyo.²⁾ The main difference lies in the new program to accelerate heavy ions. The kinds of particles and the ranges of energy expected to be obtained with this machine are illustrated in Fig. 1 (3-1).

The cyclotron, of course, accelerates protons, deuterons, (tritons), ³He ions and alpha-particles of different energies. Multiply-charged ions of carbon, nitrogen and oxygen will be accelerated over a wide energy range as shown in Fig. 1 (3-1), if a suitable ion source is developed and a sufficient RF voltage is obtained.

To carry out such a variety of operations, the cyclotron was designed to have several notable features as follows*.

Magnet Firstly, the magnet is required to produce magnetic induction ranging from 0.5 Wb/m² to 2.0 Wb/m².³⁾ Experimental studies performed with model magnets gave a solution to make the variation of the field distribution with excitation is so small as shown in Fig. 2 (3-1). The profile of pole piece^{3),4)} is of such a shape as to keep the magnetic induction nearly uniform inside the pole piece iron and the Rose shim was omitted. Four sets of circular current shims installed on the pole faces are used for the field shaping.

Radio frequency system The frequency of the oscillator is required to cover the range from 6 MC to 13.5 MC.⁵⁾ For this purpose, the shorting bar on the Lecher type stem and the liners facing the dees were designed to be movable. They co-operate to achieve the variation of resonance frequency. The coupling loop between the resonating tank and the oscillator tube must also be moved and the coupling condenser must be changed in a wide change of frequency.

For operation at a higher frequency than 12 MC, some large scale changes of the system are inevitable, such as the removal of moving liners and the exchange of plate loop. This kind of drastic change has not yet been tried. To enlarge the range of energy, a large value of RF voltage will be required and the target value of the dee-earth voltage may be 130 kV. However, under the present status it has been limited by vacuum spark to the value less than 90 kV.

An outline of the cyclotron is given in Figs. 3 and 4 (3-1) and in Table 1 (3-1).

Table 1 (3-1): Design specifications of the IPCR cyclotron

Type of magnet :	No sector, ordinary type
Pole tip diameter :	160 cm
Gap between pole tips :	26 cm
Exit radius :	74 cm
Gaps between dee and movable liners :	3.0 ~ 5.5 cm
Maximum magnetic induction :	2.0 Wb/m ²
Frequency range of oscillator :	5.2 to 12 (13.3) MC
Maximum dee - earth voltage :	80 (120) kV
Expected particles and their energy:	
p	3 ~ 16 MeV or higher
d	6 ~ 20 MeV (25 MeV)
a	12 ~ 40 MeV (48 MeV)
N ⁴⁺	56 ~ (100 MeV)

* The main part of the machine was manufactured by Nippon Atomic Industrial Group Co. Ltd. (NAIG) in co-operation with Tokyo Shibaura Electric Co. Ltd. (TOSHIBA).

References

- 1) Cyclotron Design Group: Reports I.P.C.R. (in Japanese), 41, 113 (1965)
- 2) S. Kikuchi, et al.: J. Phys. Soc. Japan, 15, 41 (1960)
- 3) S. Motonaga, et al.: Reports I.P.C.R. (in Japanese), 40, 1 (1964).
- 4) H. Kumagai: Nucl. Inst. and Meth., 6, 213 (1960).
- 5) Y. Chiba, M. Odera and T. Fujisawa: Reports I.P.C.R. (in Japanese), 40, 67 (1964).

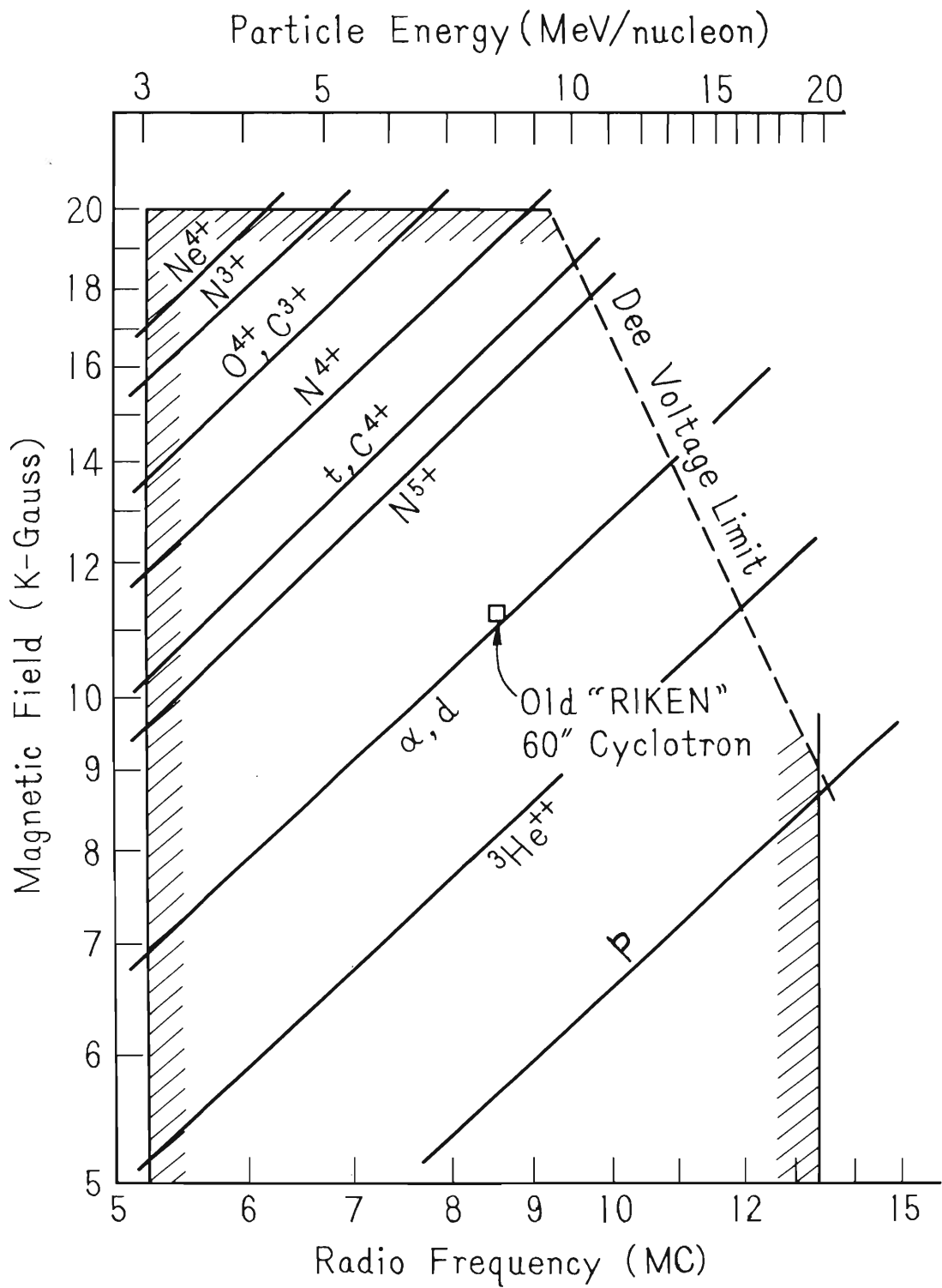


Fig. 1 (3-1) Scheduled range of particle energy of the IPCR cyclotron.

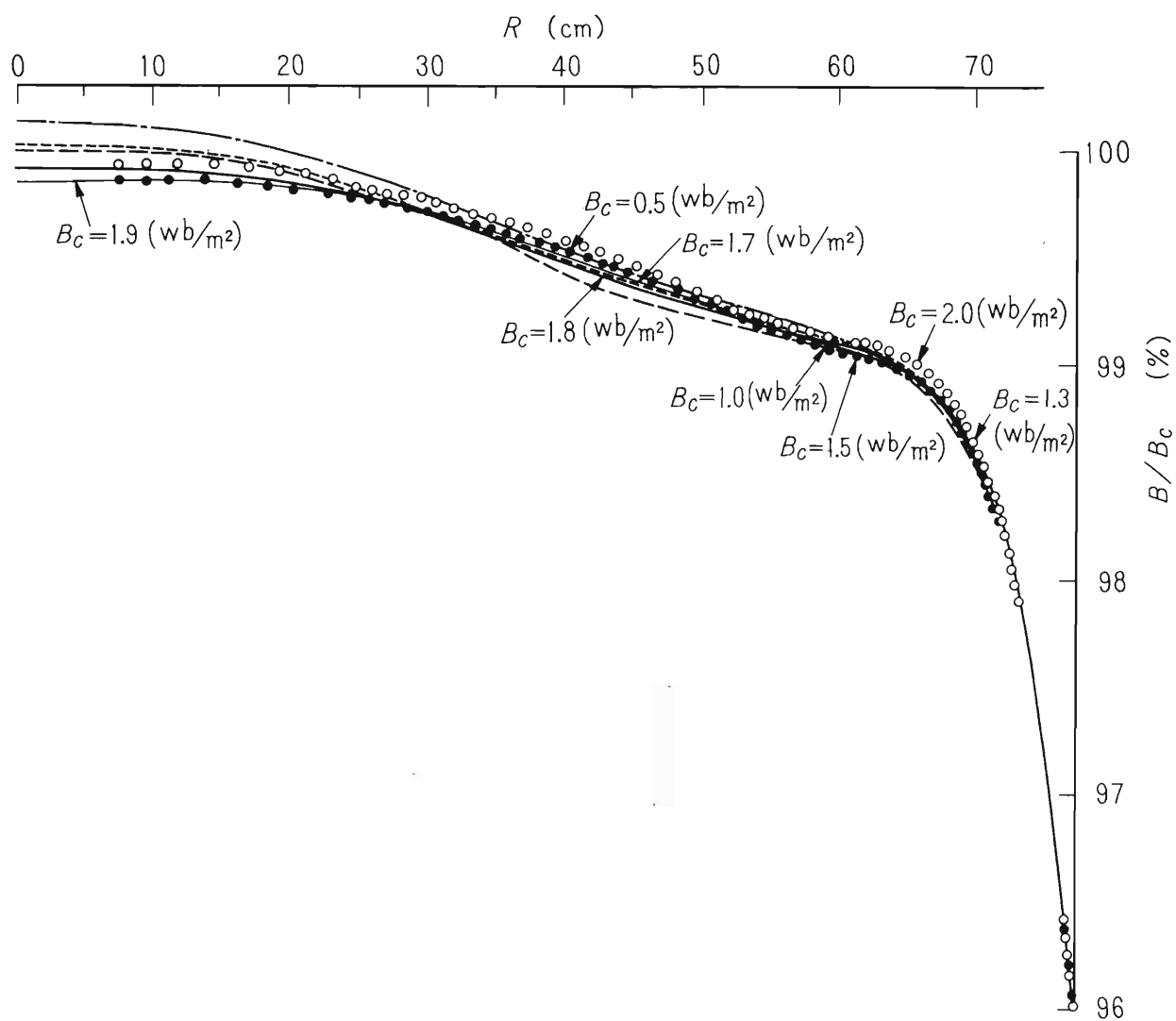
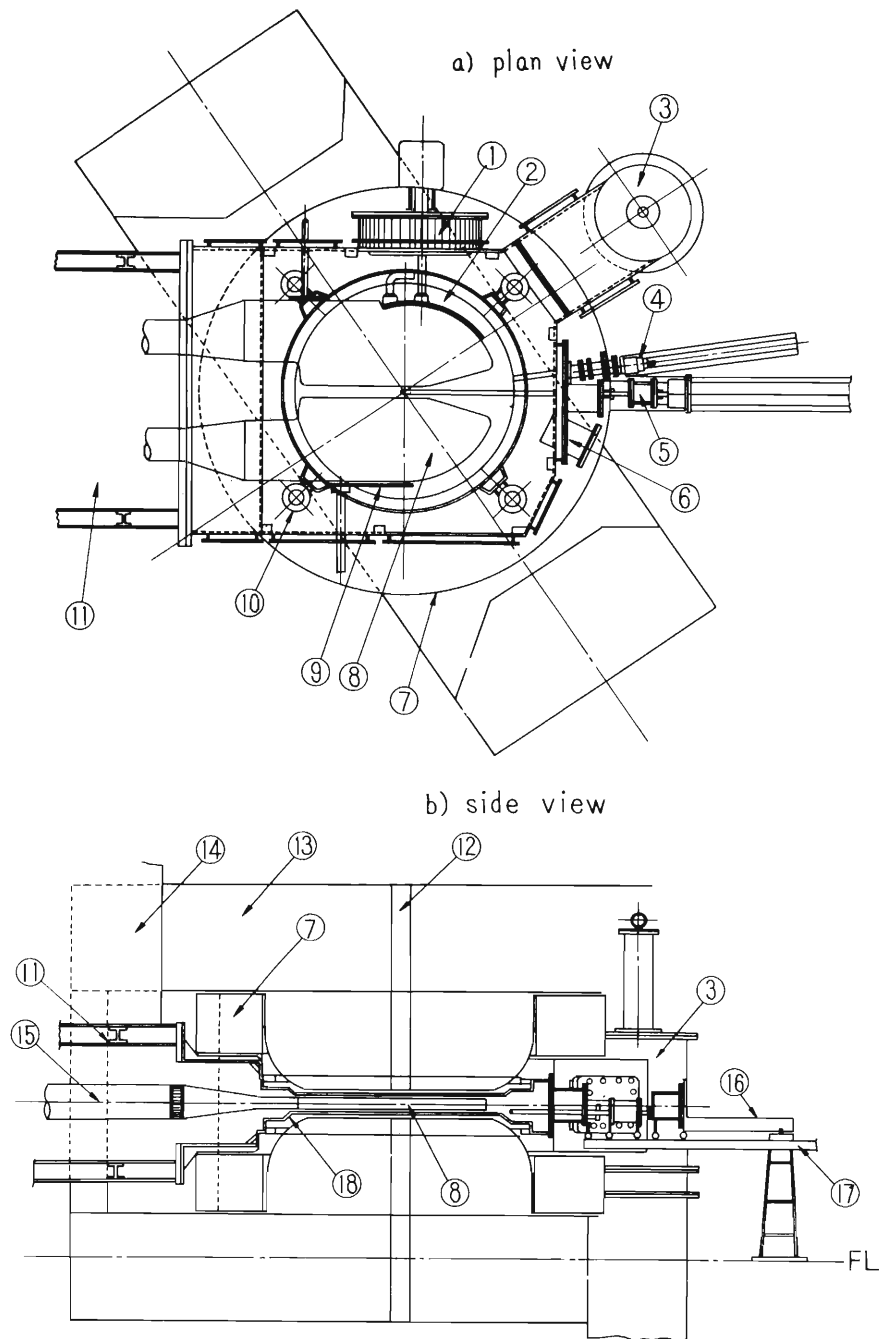
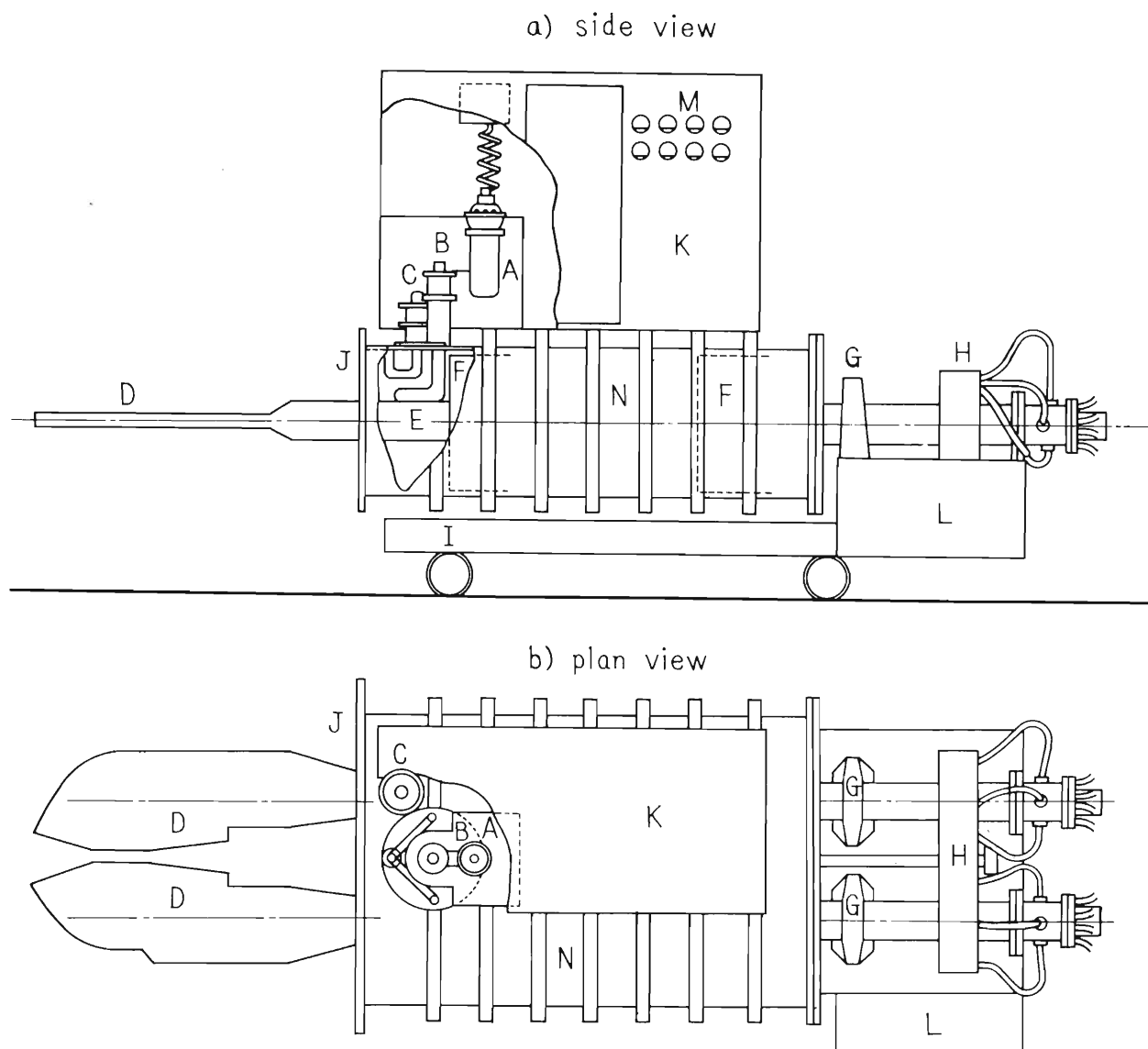


Fig. 2 (3-1) Final field distributions obtained by the measurement with model magnets.



- (1) Radio frequency shorting condenser, (2) Deflector, (3) Vacuum pump,
 (4) Beam probe, (5) Ion source positioning mechanism,
 (6) Gate valve for activation probe, (7) Coil, (8) Dee,
 (9) Capacity compensator, (10) Movable liners driving shaft,
 (11) stem tank, (12) Hole for vertical ion source,
 (13) Upper yoke of magnet, (14) Oscillator house,
 (15) Dee stem, (16) Ion source supporting bed,
 (17) Rail for the ion source motion, (18) Movable liner.

Fig. 3 (3-1) Magnet and acceleration chamber.



A: Oscillator tube, B: Plate loop, C: Cathode loop, D: Dee, E: Dee stem, F: Shorting plate, G: Stem supporting gimbal, H: Dee positioning mechanism and cooling pipe connectors, I: Stem tank carriage, J: Large flange for the connection of tank to acceleration chamber, K: Oscillator house, L: Rack for water flow relays and valves, M: Meter panel, N: Stem tank shell

Fig. 4 (3-1) Oscillator and stem tank.

3-2. Beam focusing System

S. Motonaga, H. Kamitsubo, M. Hemmi,
N. Nakanishi, and K. Matsuda

(1) Introduction

The beam focusing system for the IPCR cyclotron is described briefly. Much attention was paid to a beam analyzing system in the design to obtain high resolution beam together with flexibility for further development.

Some modifications and changes will be made in the near future when enough experience about the beam behavior is gained.

Now, these systems are working with cyclotron beam but have not yet fulfilled all kind of requirements for the cyclotron beam as described in § 2.

(2) General Layout and Operation

Fig. 1 (3-2) shows a general layout of the focusing system now under installation. The beam is deflected by an A.C. deflector, focused with a pair of the quadrupole magnets Q-0 and directed into a switching magnet SW, which bends it into one of the five experimental courses. These courses have been used for various experiments of nuclear physics, solid state physics, nuclear activation and radiation chemistry. We can get at present a beam in any desired direction and position.

The third course leads the beam to the analyzing system of high resolution which consists of two magnetic beam analyzers with the deflection angles of 80 and 35 degrees. A magnetic reaction particle analyzer of broad energy range type is now under construction. When a pair of quadrupole magnets Q-2 is provided along this course beyond SW magnet as shown in Fig. 1 (3-2) the beam on the target in the scattering chamber is remarkably intensified.

We can normally obtain $0.3 \sim 0.7 \mu\text{A}$ beam of ${}^3\text{He}$ ion with about 0.2% energy resolution, which corresponds to the deflected beam of $10 \sim 20 \mu\text{A}$ and focus it into the area of 2 mm x 4 mm.

In the near future, quadrupole magnets (Q5 – Q10) and a distribution magnet; DS will be provided.

(3) Beam Analyzing Magnet and Clearing Magnet

For a high precision measurement in the nuclear reaction study, there is an undesirable effect that the analyzed beam has low energy components due to resultant edge scattering at the exit slits of the analyzer magnet. To reduce this effect, an analyzing system with two magnets are proposed. One is called a main beam analyzing magnet and the other a beam clearing magnet.

As a beam analyzed up to 0.1% energy resolution by the main beam analyzing magnet passes through the beam clearing magnet and reaches the target in the scattering chamber, the exit slit of the beam clearing magnet has only one baffle on the low energy side to stop a part of beam contaminated by the edge scattering.

The characteristics of beam focusing system magnets are shown in Table 1 (3-2).

Table 1 (3-2). Characteristics of beam focusing system magnets

	Switching magnet	Beam analyzing magnet	Beam clearing magnet	Quadrupole magnet
Type	H-frame, semi-circular pole	H-frame, sector Edge angle 90°	H-frame, sector Edge angle 90°	Doublet
Pole gap (cm)	4	5	6	10.5
Deflection angle and pole dimensions	94 cm dia., 45°, 25°, 0°, -20°, -35° bending angle	26.0 cm wide 160 cm radius, 80° deflection angle	25.0 cm wide 160 cm radius, 35° deflection angle	Circle of 6.315 cm radius, 1.20 a a=1/2 gap
Effective beam radius	127 cm	160 cm	160 cm	—
Effective beam width	8 cm	15 cm where $B/B_0 = 2 \times 10^{-4}$ (3 kG, 8 kG)	—	6 cm
Maximum field or gradient	13.5 kG	8 kG	9 kG	930 G

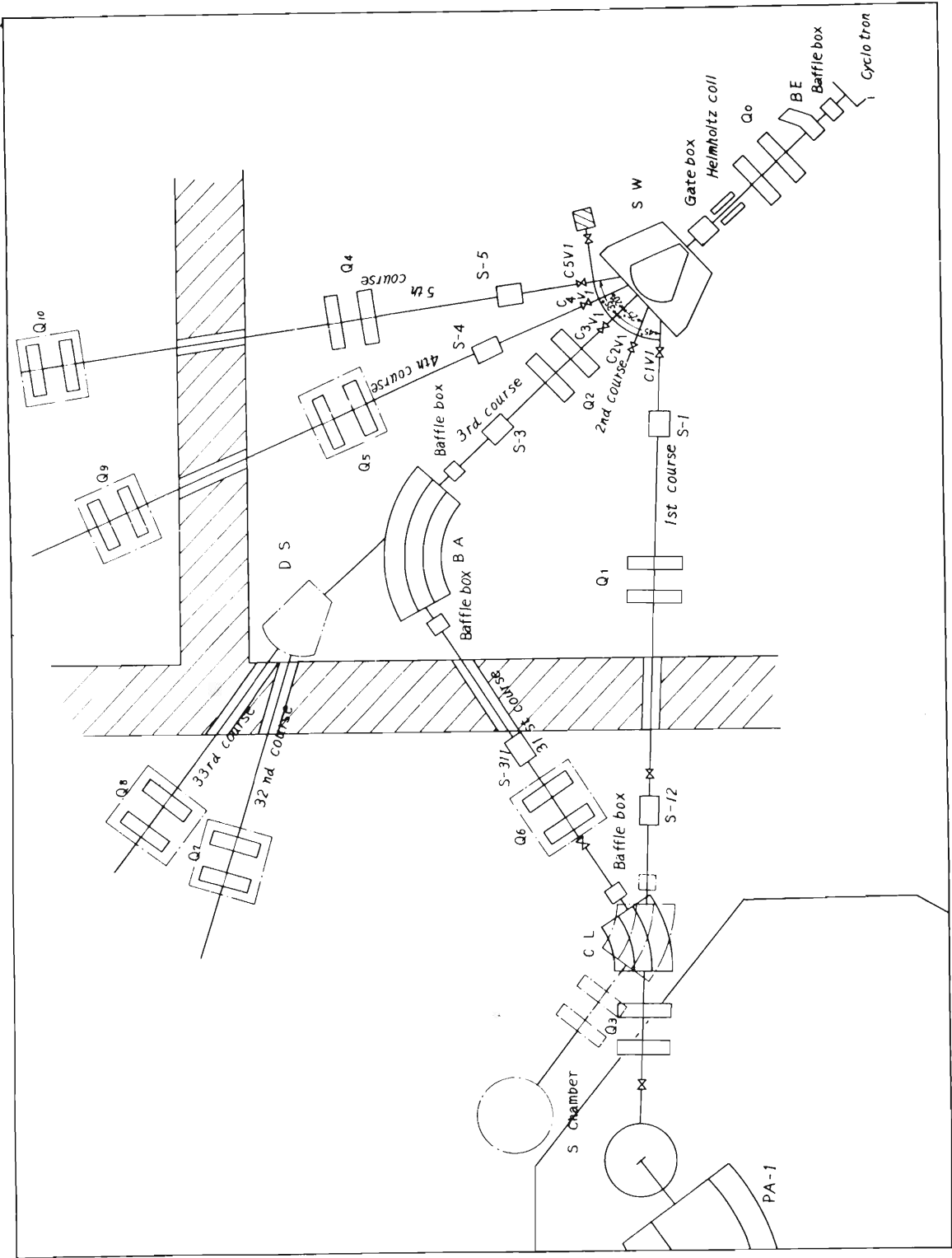


Fig. 1 (3-2) Layout of the beam transport.

3-3. Circulation System of ^3He Gas

T. Tonuma, S. Nakajima, and I. Kohno

The high cost of ^3He gas necessitates the use of a circulation system to recover any gas not accelerated or trapped in the cyclotron and to provide its purification for re-use as ion source. The system consists of a rotary pump which has vacuum tight intake, exhaust, and a charcoal trap cooled by liquid nitrogen as shown in Fig. 1 (3-3). And there are many hand and solenoid valves which are designed for protecting the circulation system from the leakage of ^3He gas.

(1) The characteristics of charcoal trap

An activated charcoal trap is used which adsorbs little ^3He gas and much air at the temperature of liquid nitrogen. We use 200 grams of charcoal, and the quantities of ^3He gas and air adsorbed by one gram of charcoal are given in Table 1 (3-3).

Table 1 (3-3). Adsorbed quantities of air and ^3He gas into charcoal trap

	Liq-N ₂ temp. (-183°C)	Room temp. (20°C)
Air	140 cc STP/g	5.3×10^{-2} cc STP/g
^3He	1.75 cc STP/g	0

A ^3He gas flow required as the ion source is from 70 lus to 100 lus (about from 6 cc/min to 8 cc/min) and the rate of contamination of air must be below 5 %¹⁾ when $^3\text{He}^{2+}$ is produced. Thus, the amount of air mixed with ^3He gas in the ion source has to be kept less than 3~5 lus. But it has been found from a preliminary experiment that after passing through the charcoal trap, the purity of ^3He gas is maintained above 99.9 % for a long time. Therefore, in the circulation system it is particularly necessary to keep the leakage between the output of the charcoal trap and the ion source below 3~5 lus.

(2) Pumping system

The two mechanical booster pumps serve as the main backing for the existing cyclotron diffusion pumps. Their output is connected to the ^3He circulation system placed in the control room (Fig. 2 (3-3)). The 50 l/min rotary pump in the circulation system, which is used during ^3He operation, as a fore pump of the cyclotron evacuating system instead of normal one, recovers the gas and forces it to the ion source through a charcoal trap dipped in liquid nitrogen.

Seven liters of ^3He gas S.T.P. has been consumed in five months. The consumption is mainly due to mistake in operation and exhaust in removing air already trapped in the charcoal trap. The leakage of ^3He gas in normal operation is negligible.

There occurs sometimes a trouble that, during operation, water collected in a gas pipe near the charcoal trap changes into ice and chokes the gas inlet to the ion source. Considerable amounts of substance showing activity of short life were found in the trap.

Reference

- 1) N.I. Venikov and N.V. Starostim: *Pribory i Tekhnika Eksperimenta*, No. 2, p. 25 (1963).

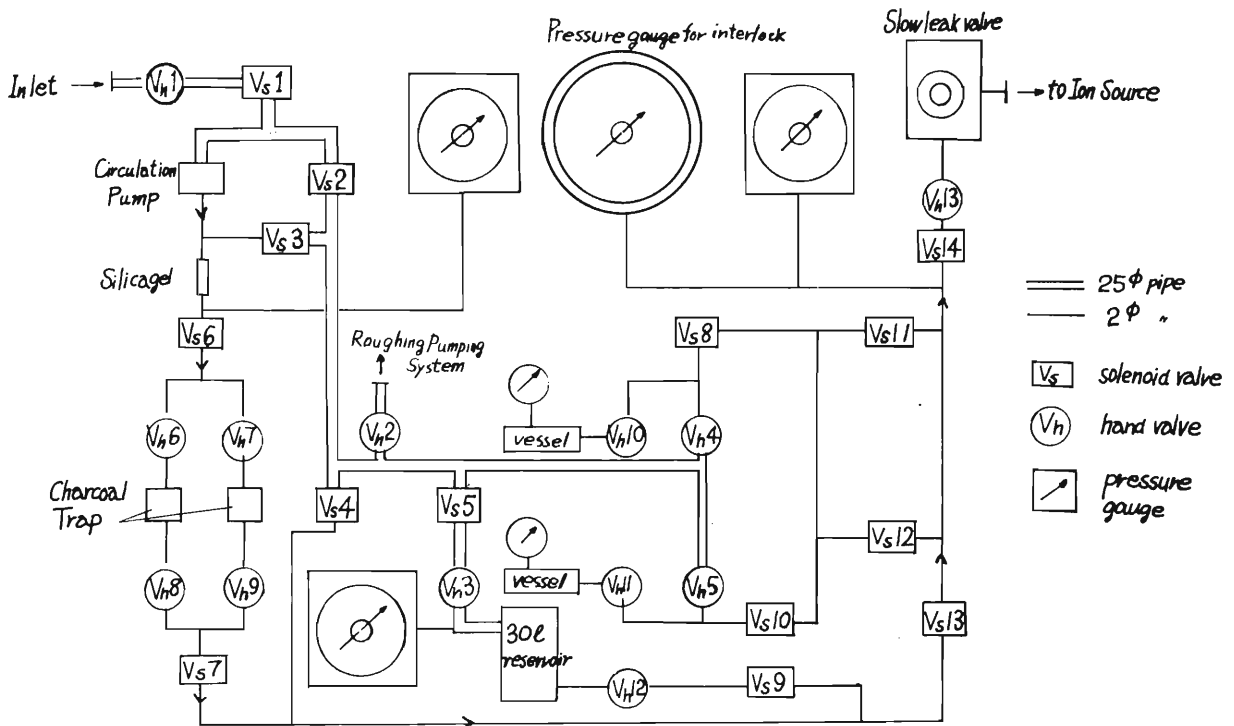


Fig. 1 (3-3). The diagram of the circulation system.

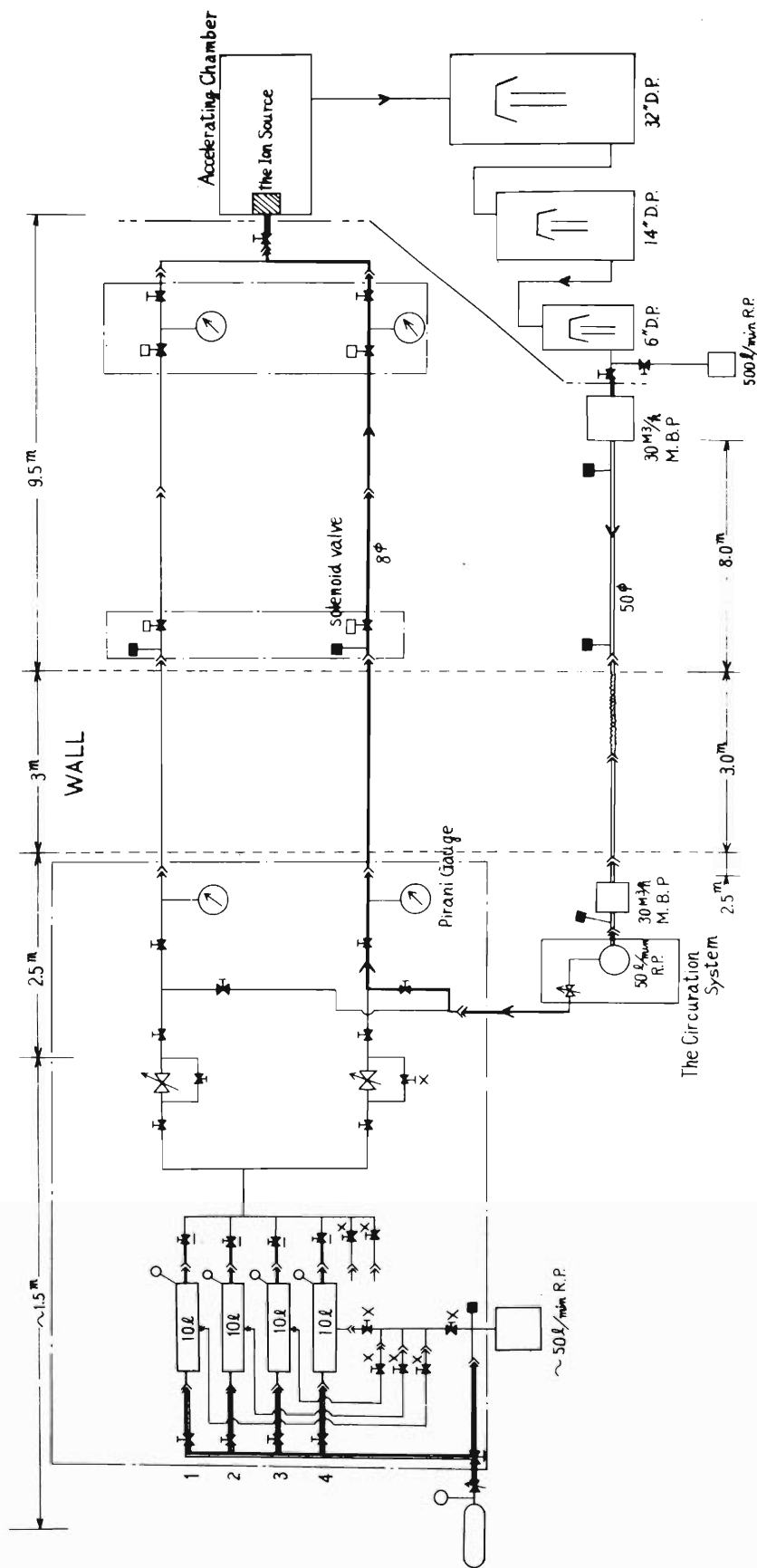


Fig. 2 (3-3). The diagram of gas flow.

3-4. On the Multicharged Heavy Ion Source

I. Kohno, T. Tonuma, and S. Nakajima

The performance of a multicharged heavy ion source for the 160 cm variable energy cyclotron, has been examined by the bench test. A hot cathode of electron bombarded type is used as the ion source. The charged state yield of ions and the source stabilities are investigated for various gases, i.e. oxygen, carbon dioxide, and nitrogen. Ion source constructions are shown in Figs. 1 and 2 (3-4). An anode is made of graphite having a length of 8 mm without cooling. A cathode is made of tungsten having a size of 8 mm in diameter and 11 mm in length, and is shielded by graphite for reducing thermal radiation loss. The source is operated at an arc voltage of 300 to 500 V and an arc current of 3 to 6 A, and the gas consumption is about 0.5 to 1.0 cc/min. The ion beam extracted from ion source is analyzed by a 180° mass-spectrometer, and the charged state spectra of carbon, nitrogen, and oxygen ions, are shown in Figs. 3 and 4 (3-4). The ratio of C^{3+} , O^{3+} and N^{3+} to the total output are 15 %, 15 % and 20 % respectively, and that of N^{4+} is about 2 %.

The same type heavy ion source has been installed in 160 cm cyclotron and a deflected beam $2\mu A$ of N^{4+} was obtained, but operation of this ion source in the cyclotron condition is somewhat unstable. The reason is now under investigation.

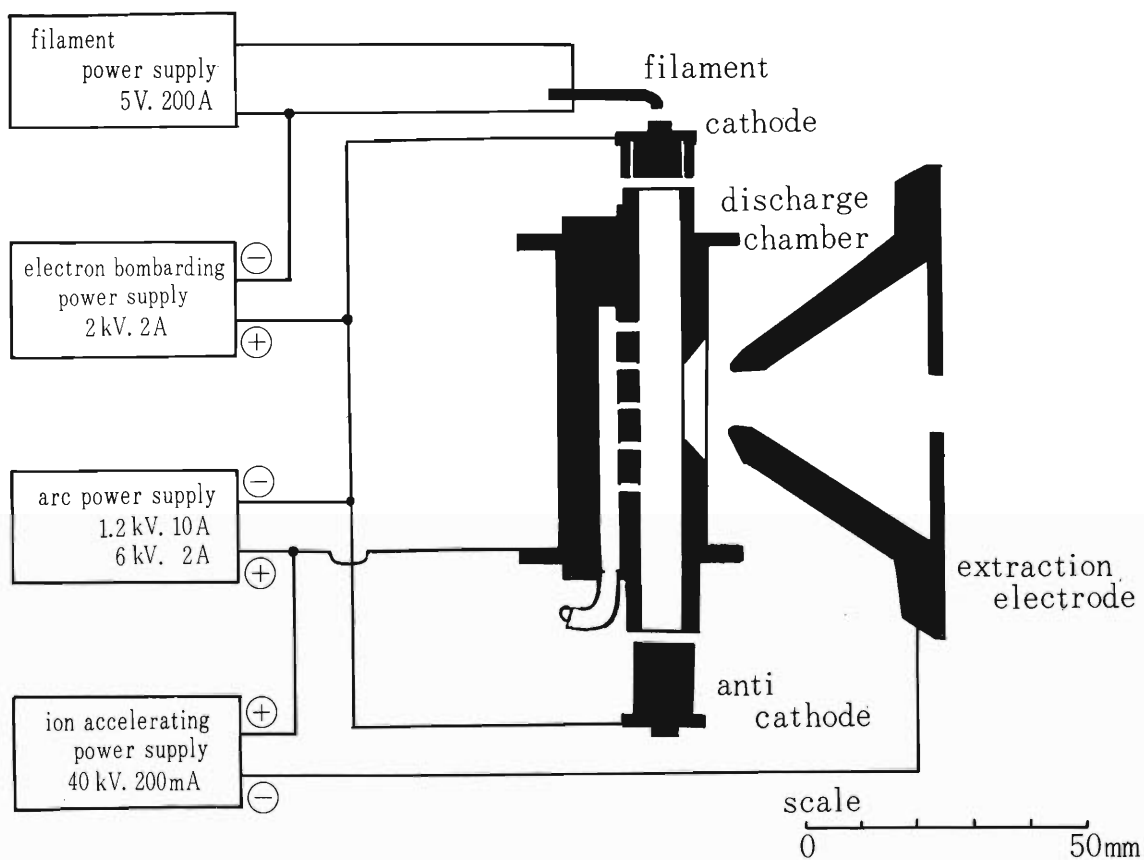
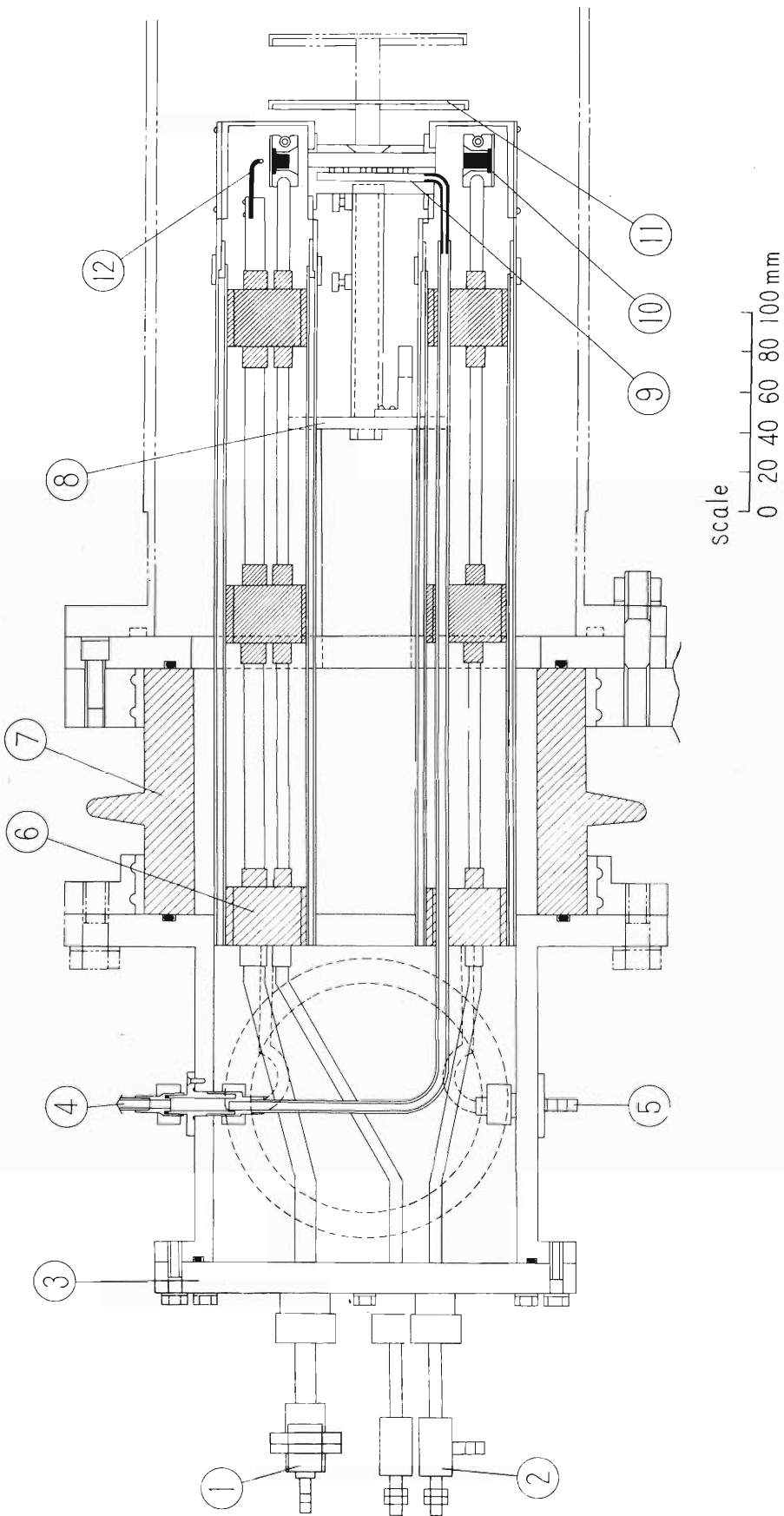


Fig. 1 (3-4). Ion source and block diagram for power supply.



(1) Filament lead (Cu), (2) Cathode lead (Cu), (3) Acrylite plate, (4) Gas inlet (Brass), (5) Cooling oil, (6) Spacer, (7) Insulator for high-tension, (8) Insulator for extracting electrode, (9) Discharge chamber, (10) Cathode, (11) Extracting electrode holder, (12) Filament.

Fig. 2 (3-4). Ion source for bench test.

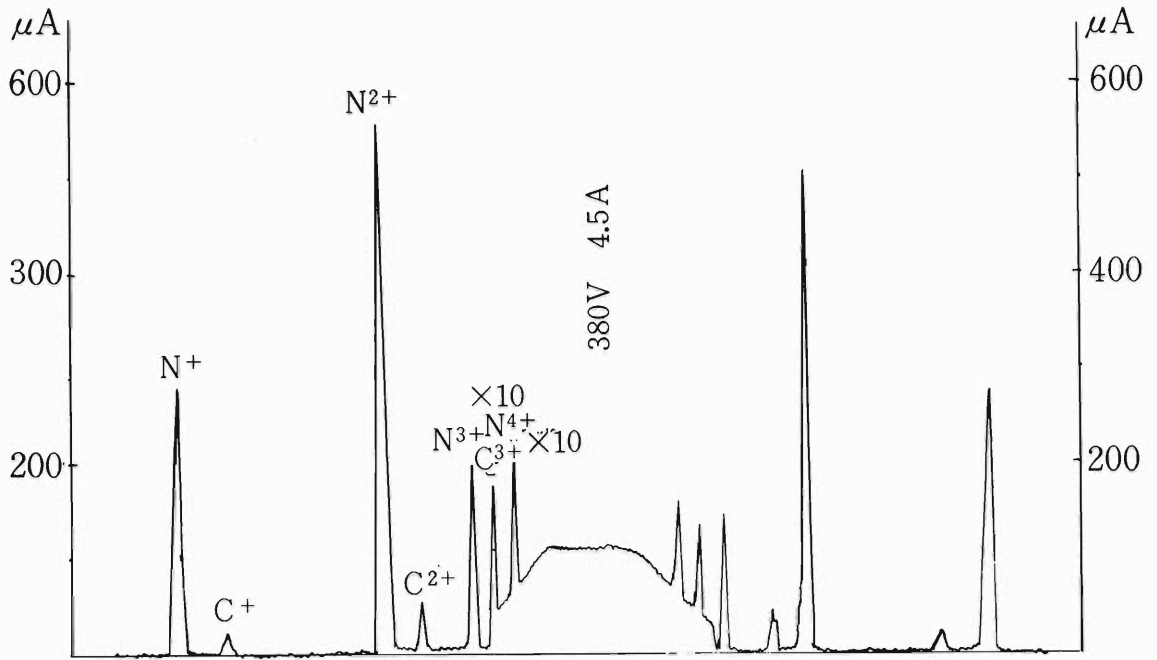


Fig. 3 (3-4). Spectrum of nitrogen ion beam from nitrogen gas discharge.

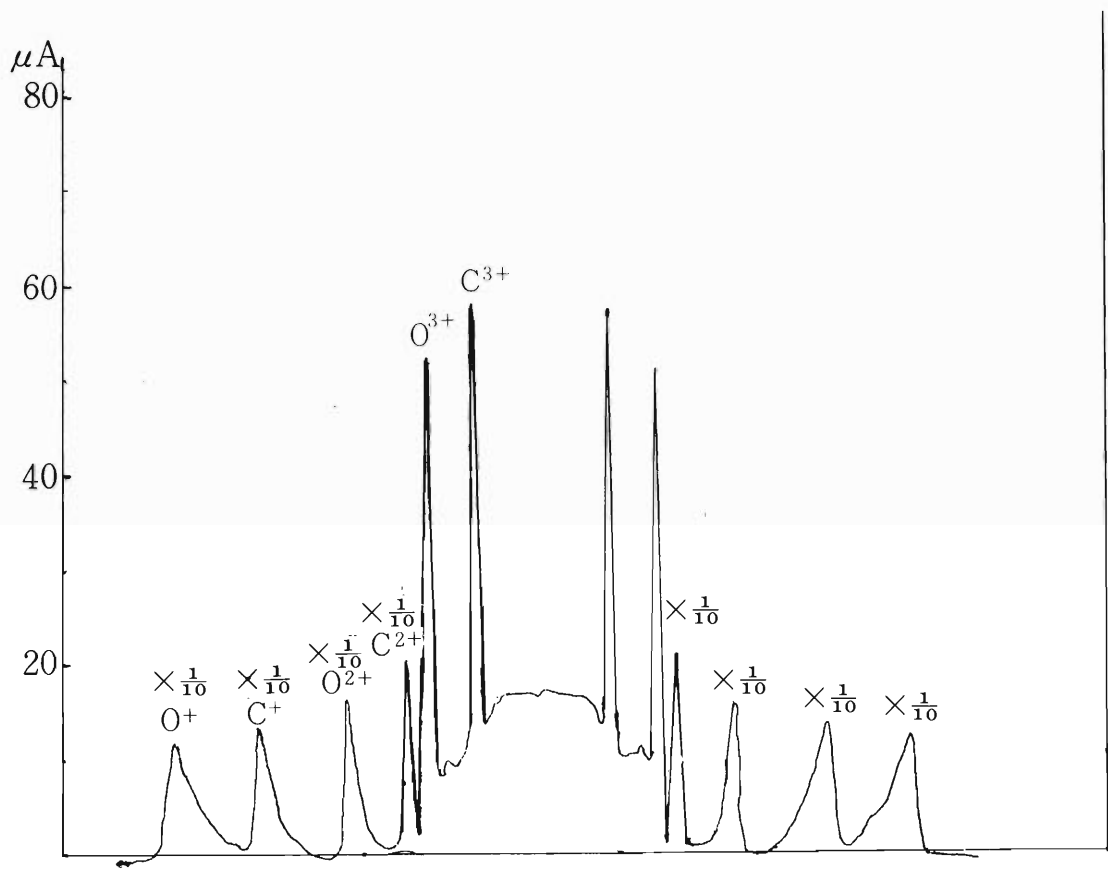


Fig. 4 (3-4). Spectrum of oxygen and carbon ion beam from CO_2 discharge.

3-5. Design of the focusing Magnetic Channel

Y. Miyazawa, T. Tonuma, M. Hemmi,
O. Terajima and M. Odera

(1) Introduction

In the IPCR cyclotron the ordinary magnetic channel which shields the fringing field of the main magnet along the path of beam is not used. Proposed maximum field for the acceleration of heavy ions is very high, and it is expected to be difficult to maintain a definite orbit with the ordinary type magnetic channel for the wide range of variable energy. At present, therefore, electrostatically deflected beam travels a very long path in the fringing field without magnetic shielding and is extracted from the acceleration chamber port azimuthally 180 degrees apart from the entrance of the deflector.

Naturally the beam spreads out radially. Transversal profile of the beam was measured at the early stage of machine conditioning and is indicated in Fig. 1 (3-5). As is clear in the figure the beam spread is rather rapid in down stream. The adverse effect of the beam spread is twofold. Firstly, owing to the finite acceptance width of the beam focusing system only a small amount of the deflected current blows into the beam piping. Secondly, the admitted beam has a rather large divergence. It is equivalent to have an object point very near to the 1st focusing quadruple-magnet. To get a small-sized image of good quality a small portion of the extracted beam has not to be discarded in the beam focusing system or strong focusing ability is needed.

To avoid these difficulties several methods are proposed. The machine is already vigorously in use, and the beam handling system has a fixed configuration. A correcting means is not permitted to alter the beam orbit greatly. The cyclotron and the focusing system have a number of parameters to be adjusted. Therefore, these means should not be a burden to the operating crew much more. Following is the one which has finished the model study and the preliminary calculation of the orbit. It will be installed in the accelerating chamber this autumn. It will not change the center orbit but make the present beam profile to shrink radially and reduce the radial divergence at the exit of the accelerating chamber. This needs little adjustment in the operation once set.

(2) Concept of B constant magnetization and its application to a focusing system

Magnetization of an infinitely long bar of circular cross section can be analytically solved. Magnetic induction at the outside of the bar is represented by

$$B_y = R^2 \frac{yz}{(y^2 + z^2)^2} B_0 \quad (1)$$

$$B_z = -R^2 \frac{y^2 - z^2}{(y^2 + z^2)^2} B_0 \quad (2)$$

Here B_0 is the uniform magnetic induction originally present. Y and Z axes are as indicated in Fig. 2 (3-5). In Fig. 2 (3-5), field pattern given by eqn. (2) is shown. Magnetic induction in the bar has only z component of $2 B_0$ in strength and is constant everywhere. This is the so-called B-constant property¹⁾, namely, the bar will not undergo local saturation, and the field pattern that it gives will not change until $2 B_0$ exceeds the magnetic saturation strength of that material. Therefore the focusing property of a system composed these bars will not be affected by external field.

We use a simple composition as shown schematically in Fig. 3 (3-5). XY-plane coincides with the median plane of the main magnet. The field shape which the channel gives can be easily synthesized from curves of Fig. 2 (3-5).

It gives radially increasing field of almost constant gradient.

When the channel is placed in such a way that the point of $\Delta B = 0$ is coincident with the center of the beam, the beam is focused radially toward the beam center and is defocused vertically. The focusing property is determined by the gradient or negative "n" value. Of course, the field of the main magnet is not uniform at the fringing field and the field gradient must be recalculated using the value of main magnet field distribution. But since the gradient of main magnet field at each bar does not change largely along the beam path, the recalculation is not difficult and the beam trajectory is easily obtained.

Also, the relative distribution of fringing field of this main magnet itself does not change very much against a wide range of its excitation owing to its special pole profiles.¹⁾ And so, once the field pattern and the focusing properties of the channel are determined, the trajectory of the particles is essentially invariant against the excitation of the magnet as long as the bar is not saturated.

This channel gives the disturbance or the bumps to the main field. Its quantity is also given by eqn. (2). By choosing the size and location of bars properly, the effect can be reduced to the order of $n \times 10^{-4}$ in the main field.

(3) Results of model study and calculation of beam trajectory

One-third scale channel is constructed and tested in the pole gap of a small magnet to make clear saturation property and finite length effect. Relative value of field strength is directly obtained using two Hall Methods developed in this laboratory²⁾, which simplify the measuring procedure. Fig. 3 (3-5) shows the results measured. Field pattern at 40 mm from the end of the channel maintains a constant gradient of 24 % per cm from low field to 1.3 Wb/m^2 . Calculated gradient is also plotted in that figure. Saturation of iron is expected to begin earlier at the lower field near the end than in the middle of the channel. Really, the constant gradient can be maintained until B_0 becomes 1.0 Wb/m^2 even at the end. Since the strength of fringing field at the point where the channel is to be placed hardly exceeds 1.0 Wb/m^2 , relative field gradient in the channel is practically constant for any excitation strength of the main magnet.

Trajectory of the beam is estimated for the uniform channel, the structure of which is shown in Fig. 4 (3-5). As n-value is not constant throughout the channel, the calculation is made by dividing the channel into several sections and constructing conversion matrix for each section. Particles which are 1 cm apart and placed at an angle of to the center trajectory at the entrance of the channel will move in the trajectory which is parallel to the equilibrium orbit and less than 3 cm apart from it, after traversing

through about 80 cm of the channel. Of course this length can be reduced using a certain different configuration. Improvement of this procedure and the method of supporting this device near the poles are now under examination.

Reference

- 1) H. Kumagai: Nucl. Instr. and Methods, 6, 213 (1960).
- 2) M. Hemmi et al.: Reports I.P.C.R. (in Japanese), 39, 170 (1963).
Proc. Intern. Symp. on Magnet Technology, p. 472 (1965)
(Stanford) U.S. Dept. Commerce, Springfield, Virg., U.S.A.

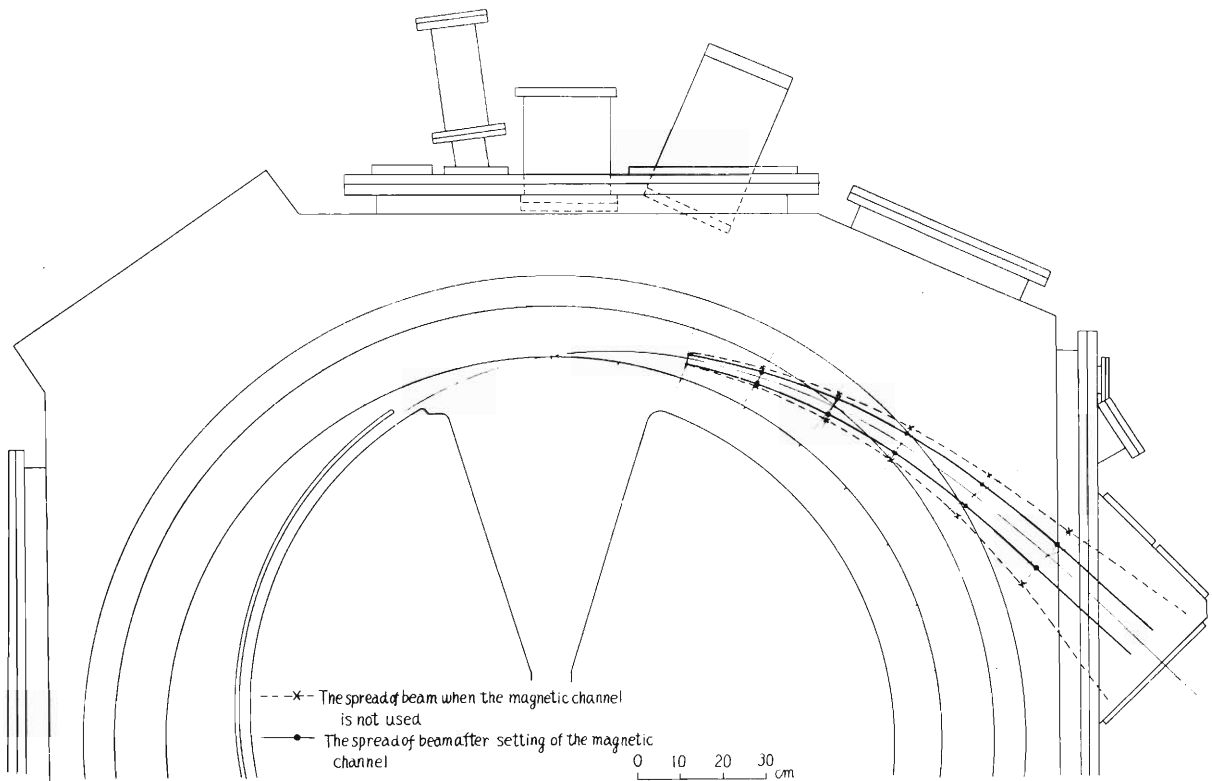


Fig. 1 (3-5). Measured beam spread and the expected focusing effect of the channel.

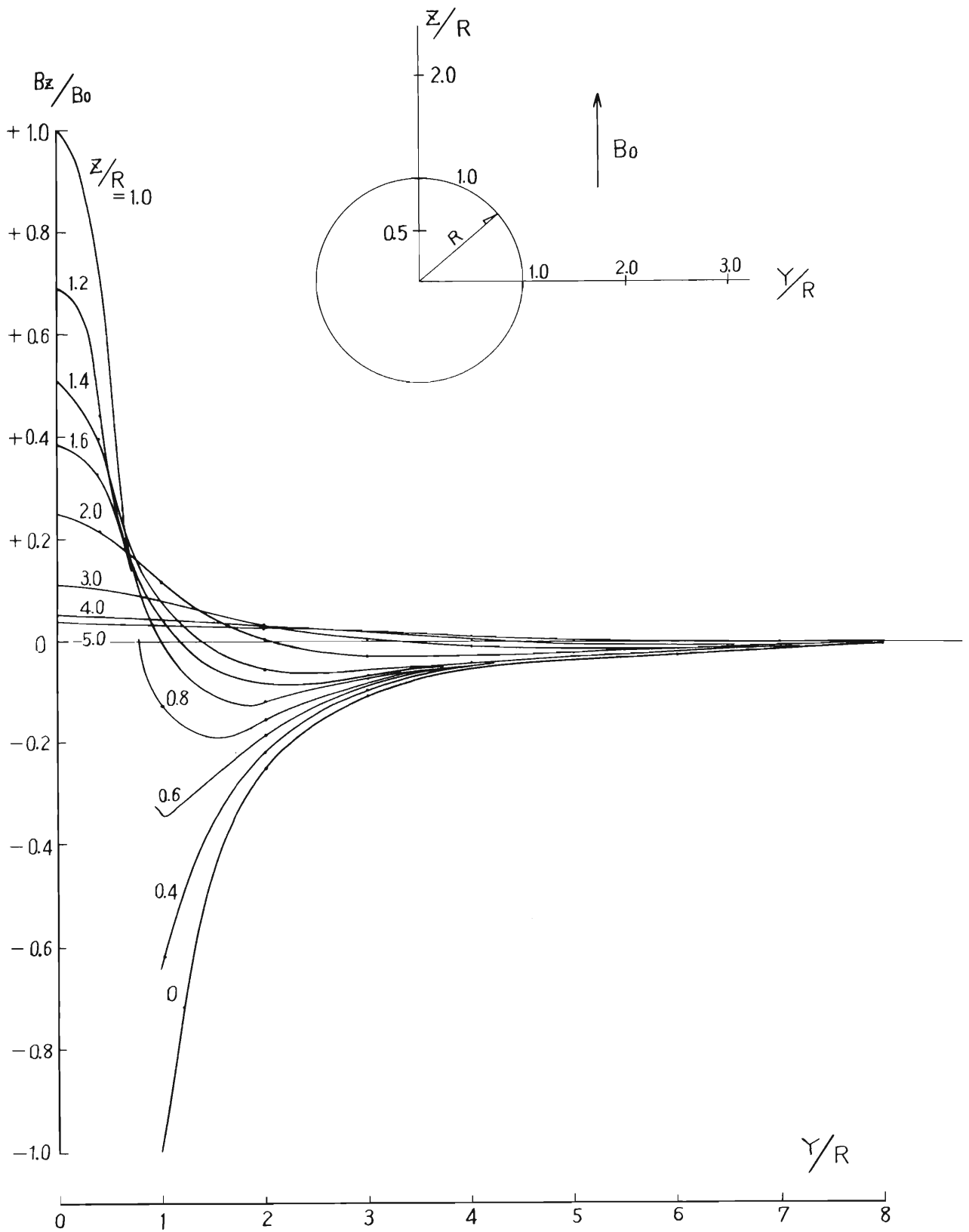


Fig. 2 (3-5). Field induced by an infinitely long bar ($\mu = \infty$) placed in the uniform magnetic field.

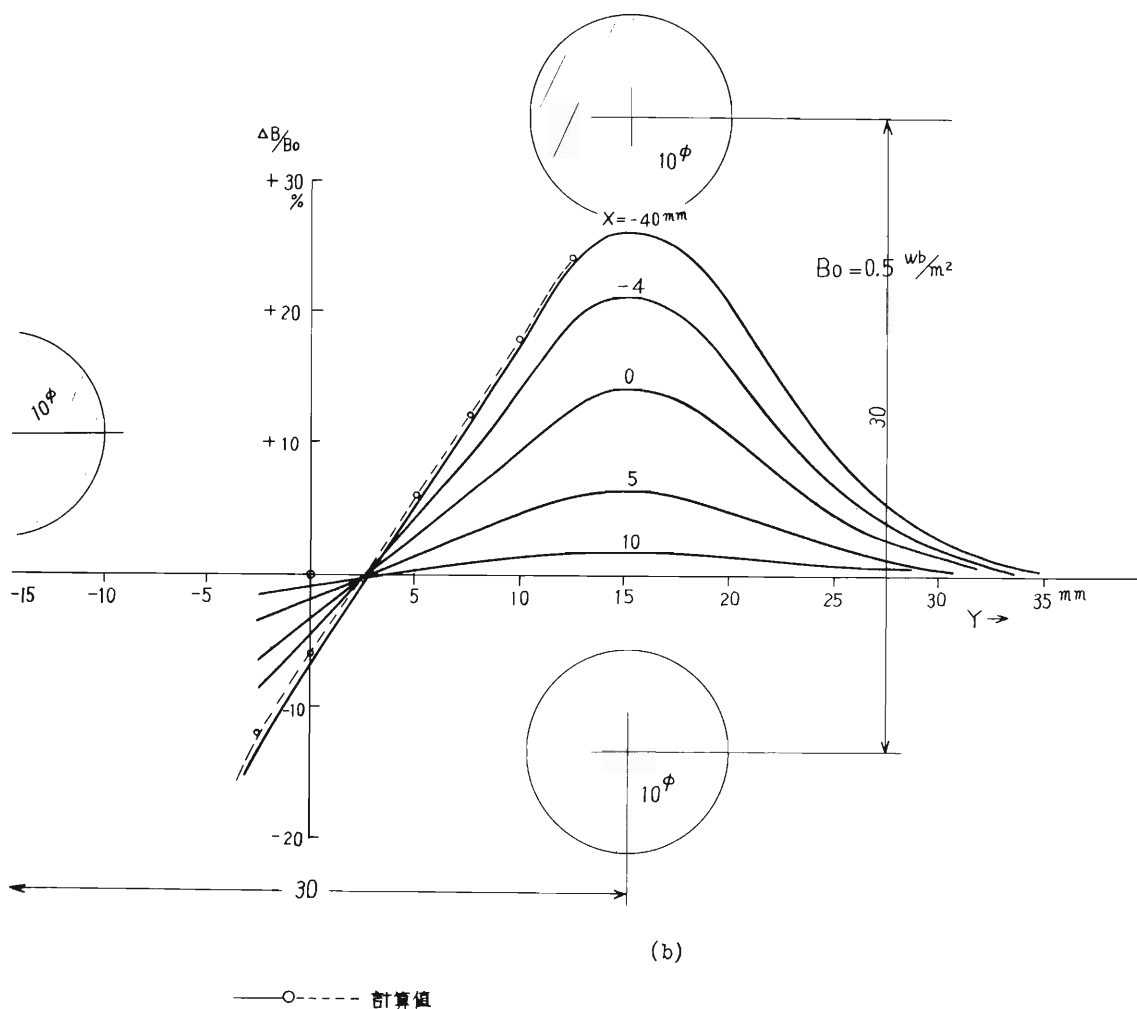
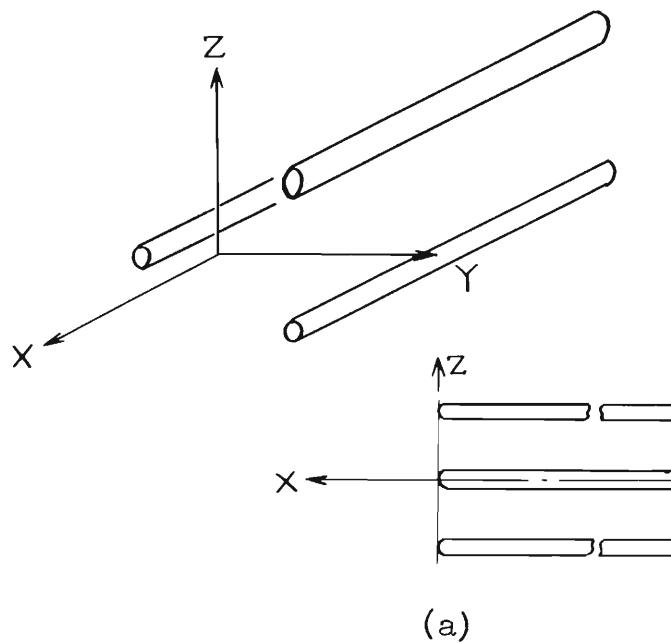


Fig. 3 (3-5). (a) Schematic diagram of the focusing channel.
 (b) Field distribution in the median plane of 1/3 scale magnetic channel.

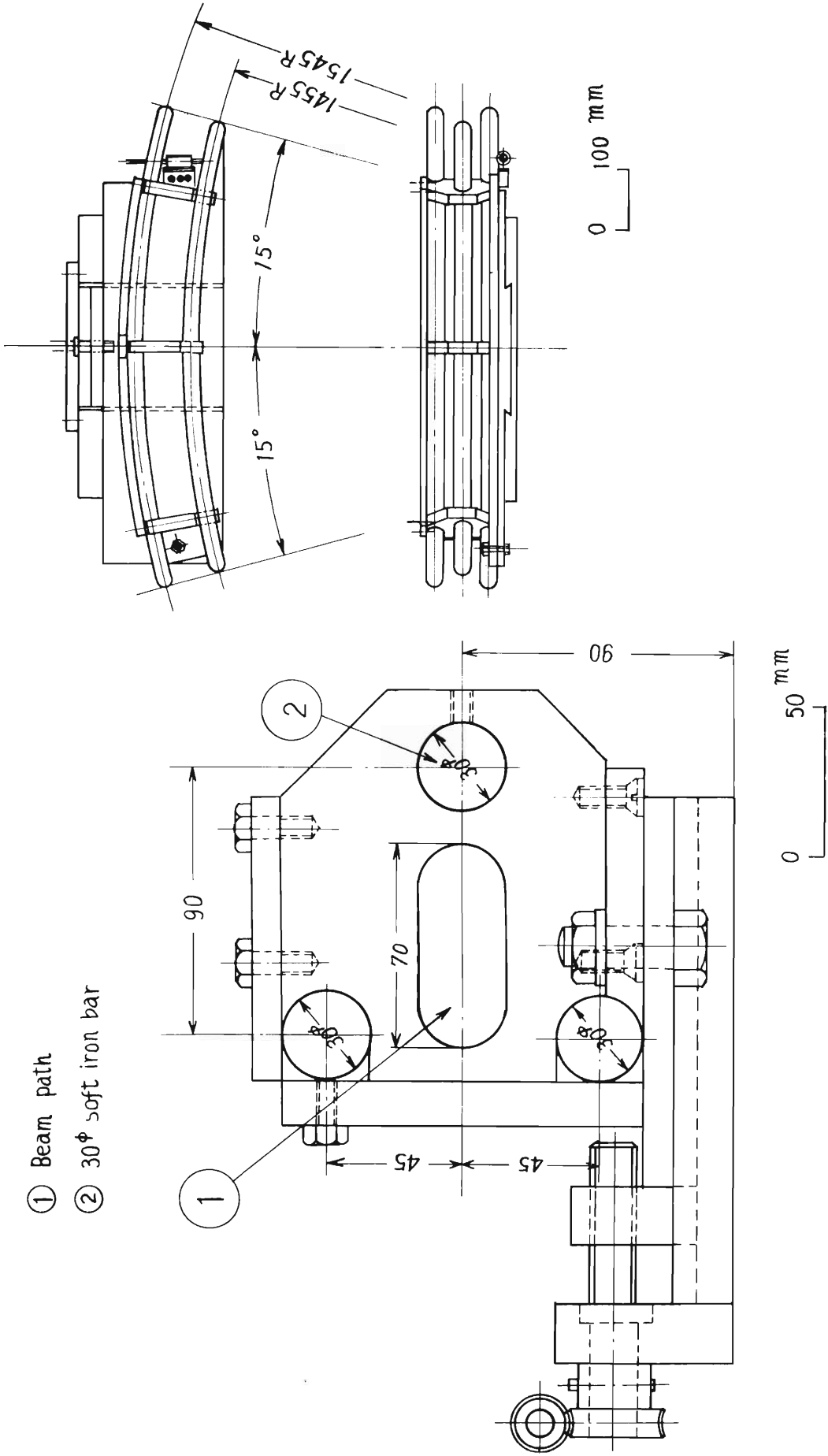


Fig. 4 (3-5). The design of channel indicating the position adjusting mechanism.

4. ACCELERATOR PHYSICS

4-1. Initial Motion of Ions

Y. Miyazawa, T. Tonuma, S. Motonaga, M. Hemmi,
A. Shimamura, T. Inoue and T. Karasawa

We began to study a beam trajectory in the central region. The IPCR cyclotron has two dees connected to form shielded Lecher line resonator and an ion source holder is inserted on the center line between dees. An usual beam probe, moves on 7.5 degree line and measures the beam current from 20 cm radius to maximum radius and that of deflected beam.

We made also a special beam probe. It can measure beams from the neighborhood of ion source to about 20 cm radius. A 2 mm diameter tungsten wire, vertically 70 mm long, moves along the center line between dees (A-B line in Fig. 2-a (4-1)). The radial distribution of the beam is measured in a form of differential trace. The tungsten wire is not cooled for the sake of simple construction and it can withstand large beam current above several mA. One of the radial plots is shown in Fig. 3-a (4-1). Beam bunch and turn separations are shown which linearly increase with dee voltage at early turn. When ions are reversely injected to east dee (usually to west dee), a beam distribution along the A-C line in Fig. 2-a (4-1) can be measured. The radial distributions on this line are expected to be spread broadly and one of the experimental results is shown in Fig. 3-b (4-1).

The electric and magnetic fields precisely determined in the central region are necessary for beam study and the electric field distribution between dees without feeler has been solved analytically. A configuration of the ion source and feeler, which are now used, is shown in Fig. 1 (4-1) and we tried three types of configurations; usual one with feeler, without feeler and with grid at the edge of the feeler. The distance d from the ion source to the first turn, in the case without feeler and injection to west dee, and the normalized dee voltage are shown in Fig. 2-b (4-1). Proton and ${}^3\text{He}^{++}$ are accelerated and dee voltages are divided by m/q . Linear dependence and agreement with calculation are shown.

A differential beam probe was used to measure the radial beam distribution from 30 cm to maximum radii but individual turns were washed out by poor regulation of dee voltage. The dee voltage stabilizer will be installed this autumn.

A three-finger probe was used for vertical distribution of beams from 20 to maximum radius. A large beam loss from 20 cm to 35 cm radii was found. The origin of the loss was searched but we cannot make it clear at present.

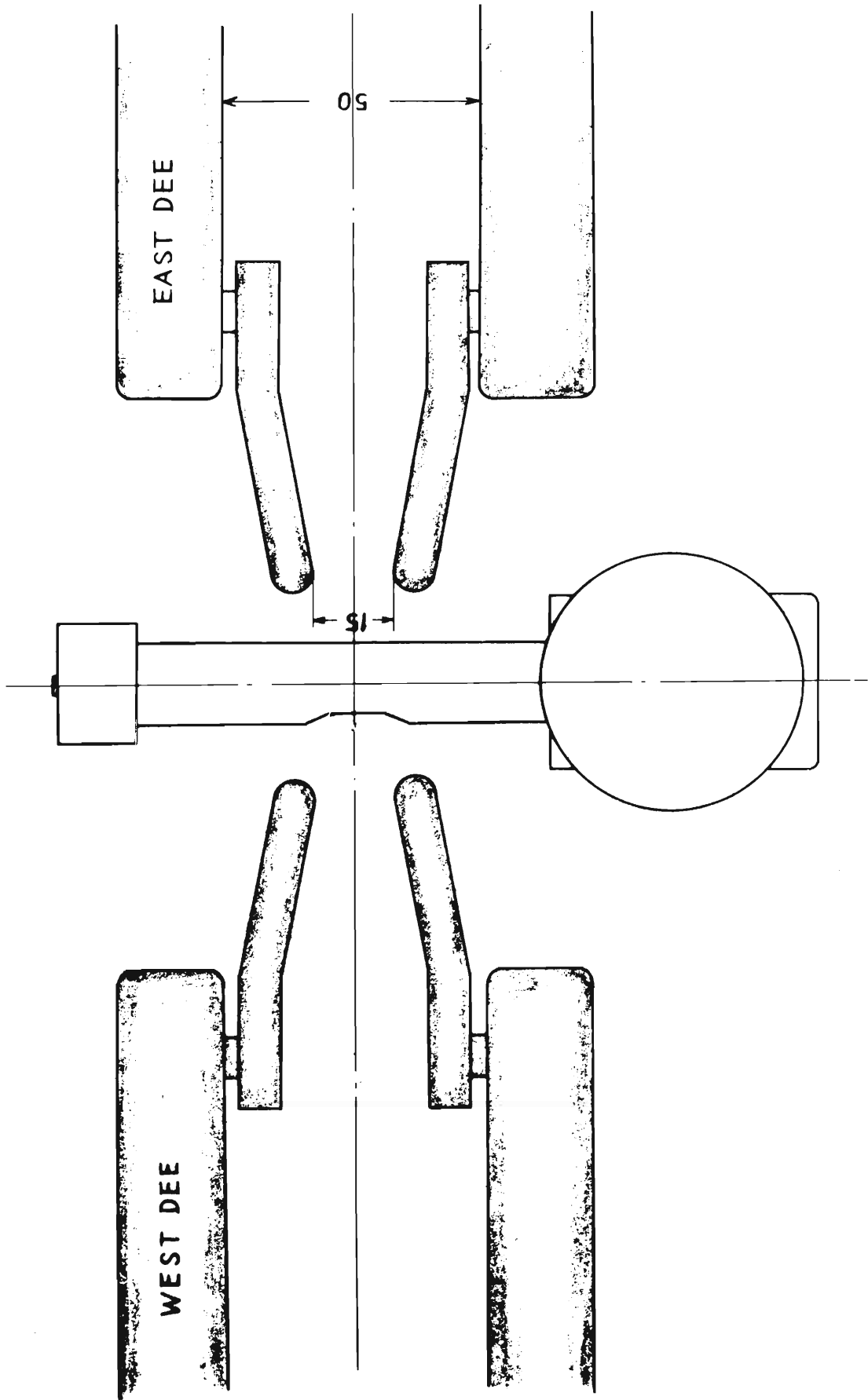


Fig. 1 (4-1) The central cyclotron region, showing the ion source, feeler, and dees.

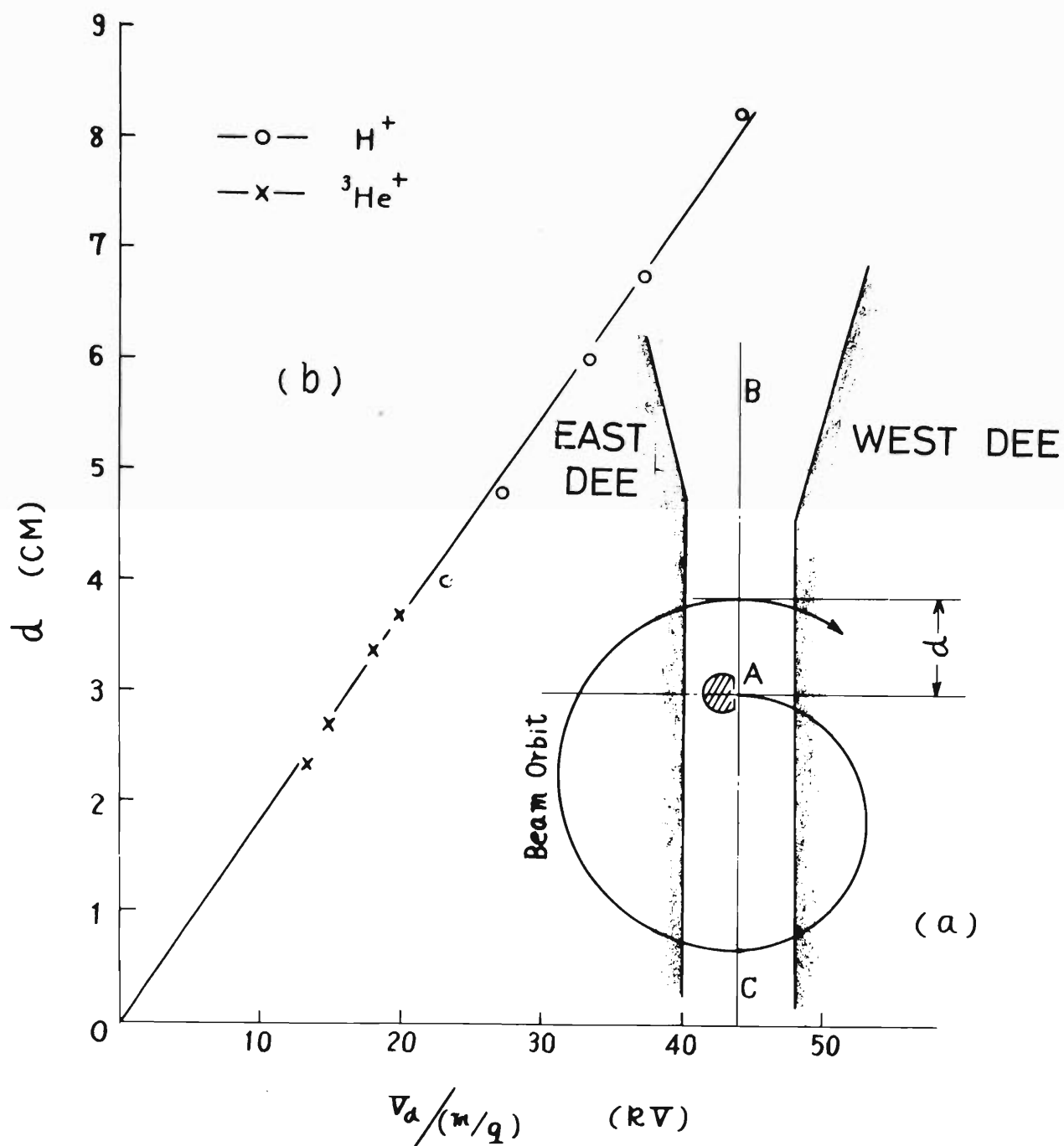


Fig. 2 (4-1) (a) The case of west dee injection. (b) The distance from the ion source to the first turn vs. the normalized dee voltage.

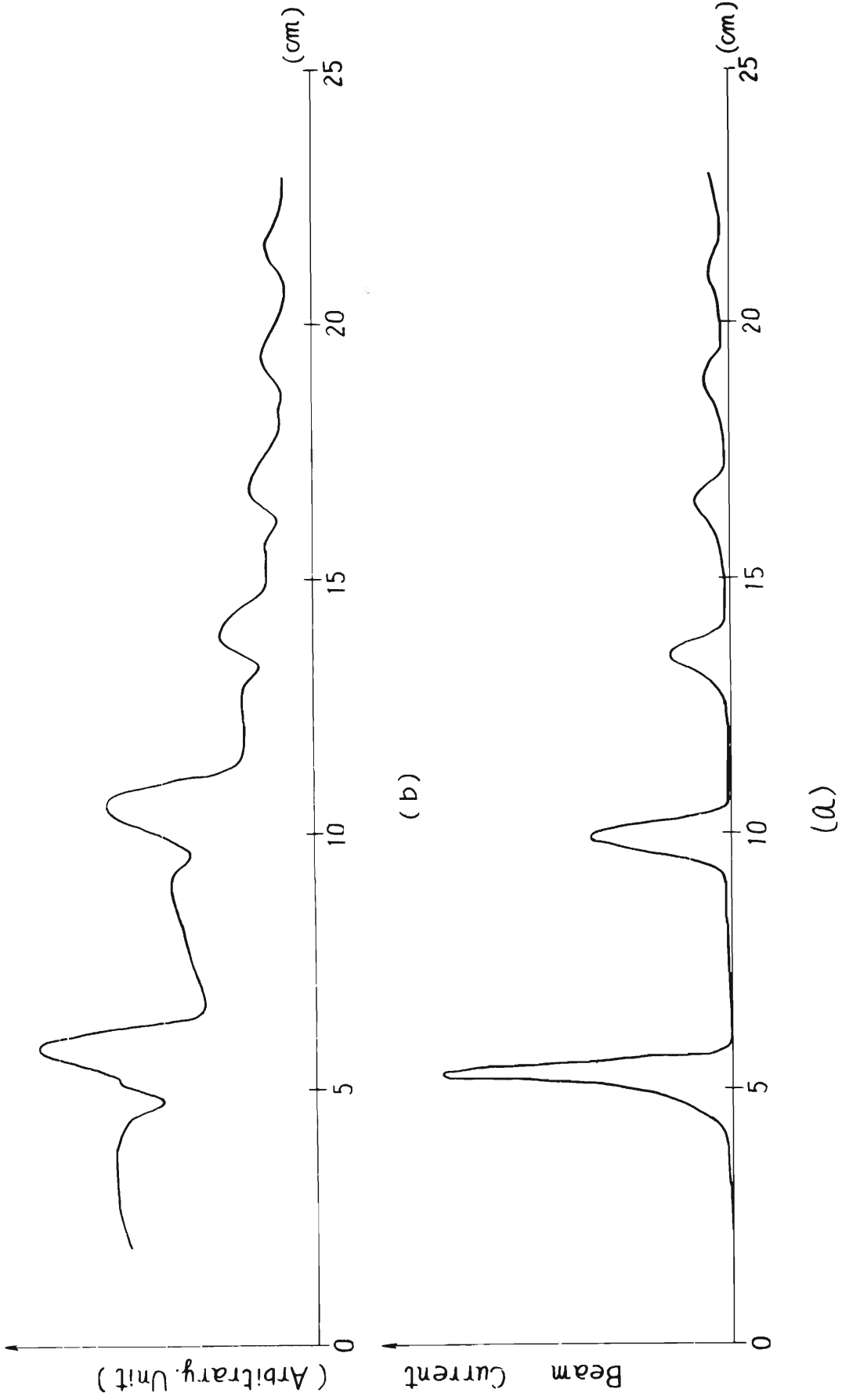


Fig. 3 (4-1) Beam density vs. radius. (a) In the case of west dee injection.
(b) In the case of east dee injection.

4-2. Investigation on Electromagnets

Hysteresis Effect of Field Distribution

S. Motonaga, K. Matsuda, N. Nakanishi,
M. Hemmi and H. Kumagai

Design of the electromagnets used for an accelerator and in a nuclear magnetic resonance research has been extensively developed in these several years.

For many experiments in physics it is necessary to have a magnetic field of the highest degree of homogeneity in spite of variations of the magnetic field strength. Such an electromagnet can be designed by using properly shaped magnetic pole pieces which make saturation effects minimized at any edges or sharp corners of the pole, and has been successfully installed in a few cyclotrons and many experimental equipments. (1,2,3,4)

If usual rectangular or cylindrical pole pieces are used, the edges of such pole pieces become saturated and the relative permeability varies in the different parts of pole pieces even for fairly low field. These effects spoil the homogeneity of the field and change the distribution of the field with the variation of magnetic field. It is the purpose of this study to show experimental results which illustrate how hysteresis effects of iron affect the magnetic field distribution even at a low field strength.

The hysteresis effect in the magnetic field is well recognized as due to the remanent field and as resulting from the difference in values of field strength in increasing and decreasing ampere-turns. However, the change in the field distribution due to the hysteresis effect was not yet analyzed in detail. This problem becomes serious when high homogeneity is required in order to make higher resolution experiments of charged particles from nuclear reactions.

The hysteresis effect of about 1×10^{-3} has been observed by the measurements of the field distribution of transporting and analyzing magnets for the cyclotron beam of 0.3 and 0.5 Wb/m² in field strength. In these magnets, the pole shape is nearly cylindrical or rectangular as shown in Fig. 1 (4-2), and thus the magnetic induction in the pole is not constant. Therefore it is thought that the hysteresis loop of iron is not the same at different parts of the pole and that the hysteresis effect appears remarkably in the field distribution in the air gap.

A typical result of measurements is shown in Fig. 2 (4-2). It is seen that the hysteresis effect appears near the edge. When the exciting current of the magnet is decreasing, the field near the edge is higher than that when it is increasing, which amounts to about 1×10^{-3} and 5×10^{-4} at 0.3 and 0.5 Wb/m², respectively.

To examine a variation of the field distribution due to such a hysteresis effect, measurements of the field distribution have been made by attaching the iron pieces of a B-constant profile to the entrance side of the pole as shown in Fig. 3 (4-2). Results of the measurements of the field distribution do not show remarkable improvement for the hysteresis effect. However, when a magnet pole is shaped after B-constant curve in all sides, it will be expected to approach a constant distribution of the magnetic induction in the pole iron and to reduce the hysteresis effect. Another reason for inhomogeneity depending on excitation is considered to come from the inhomogeneity of raw

material. We are intending to continue this kind of investigation for the further improvement of high resolution electromagnets.

References

- 1) H. Kumagai: Nucl. Instr. and Meth., 6, 213 (1960).
- 2) C. M. Braams: Nucl. Instr. and Meth., 26, 83 (1964).
- 3) A. Huber: Nucl. Instr. and Meth., 33, 125 (1965).
- 4) T. Karasawa, et al.: Proceedings of the International Symposium of Magnet Technology 1965.

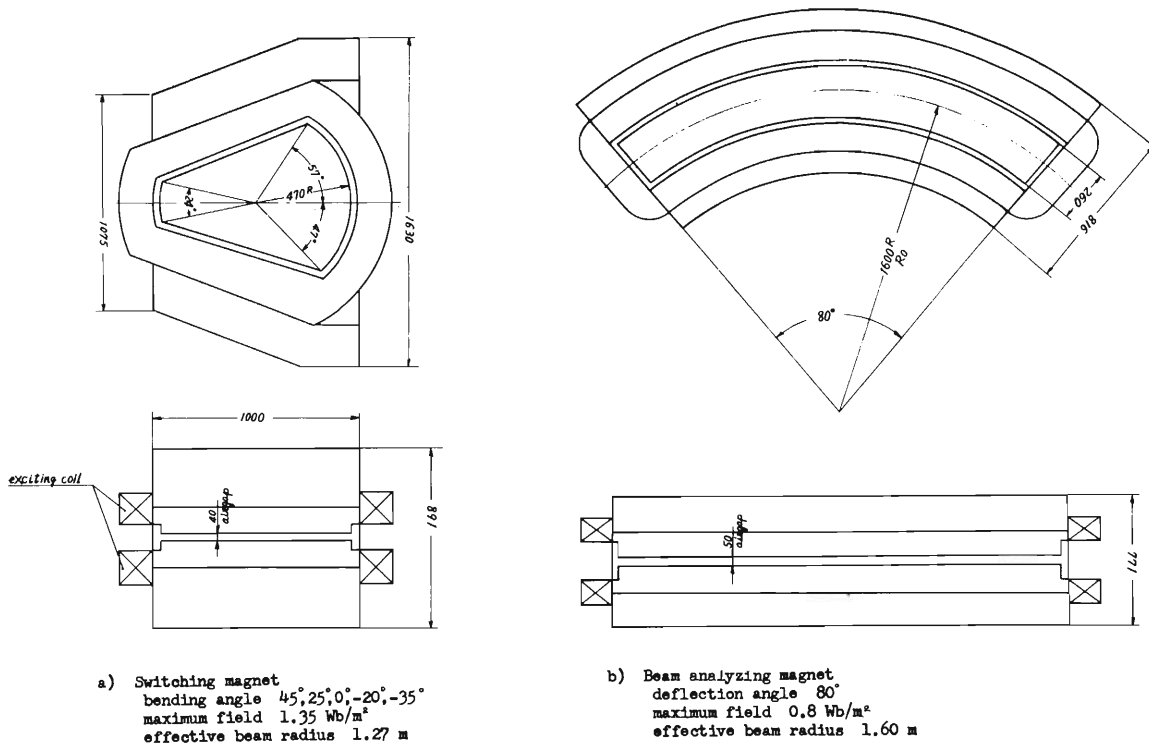


Fig. 1 (4-2) General view of the switching and analyzing magnets for the IPCR cyclotron beam.

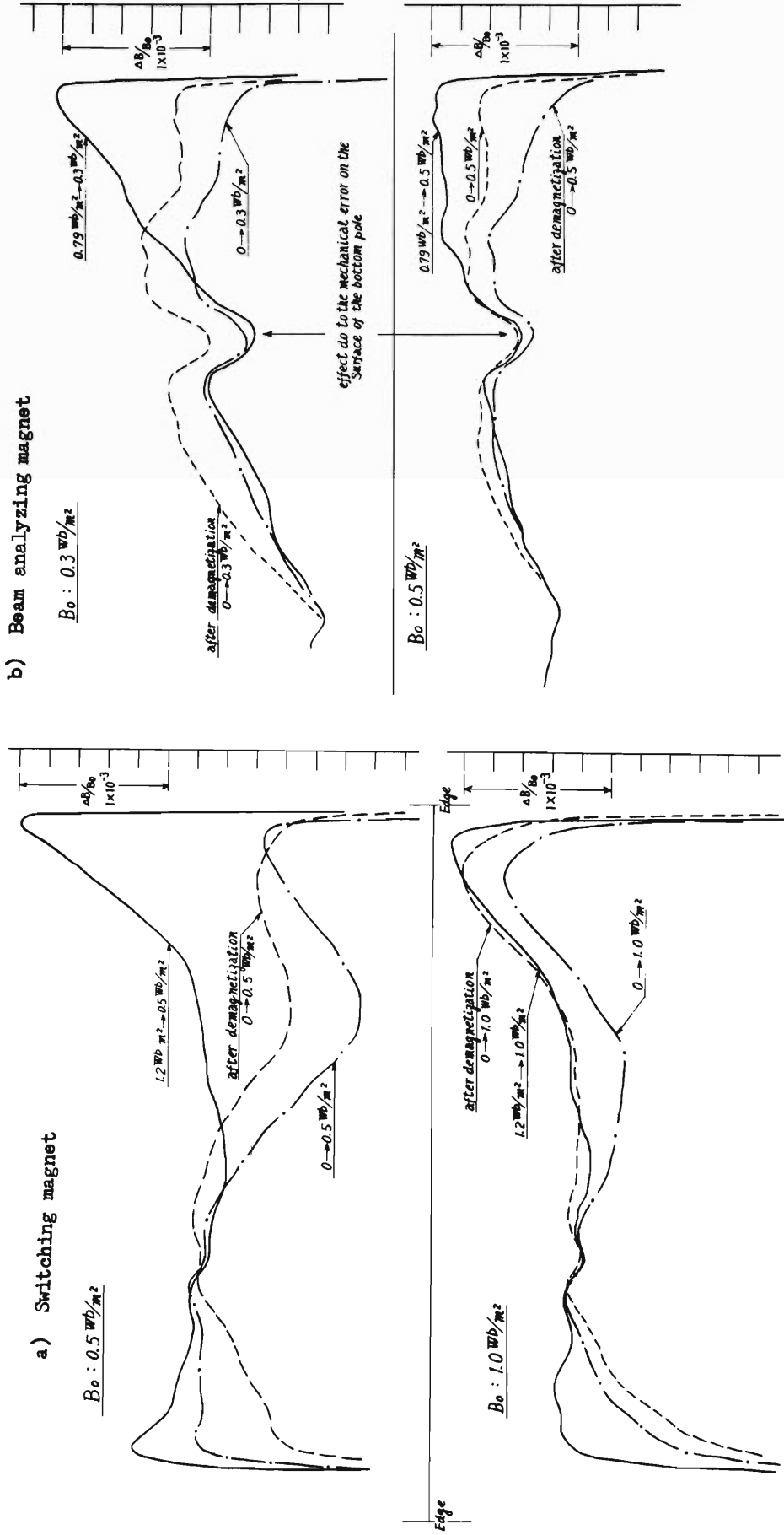


Fig. 2 (4-2) Variation of the field distribution along the beam path in air gap depending on the cases of increasing and decreasing the field strength.

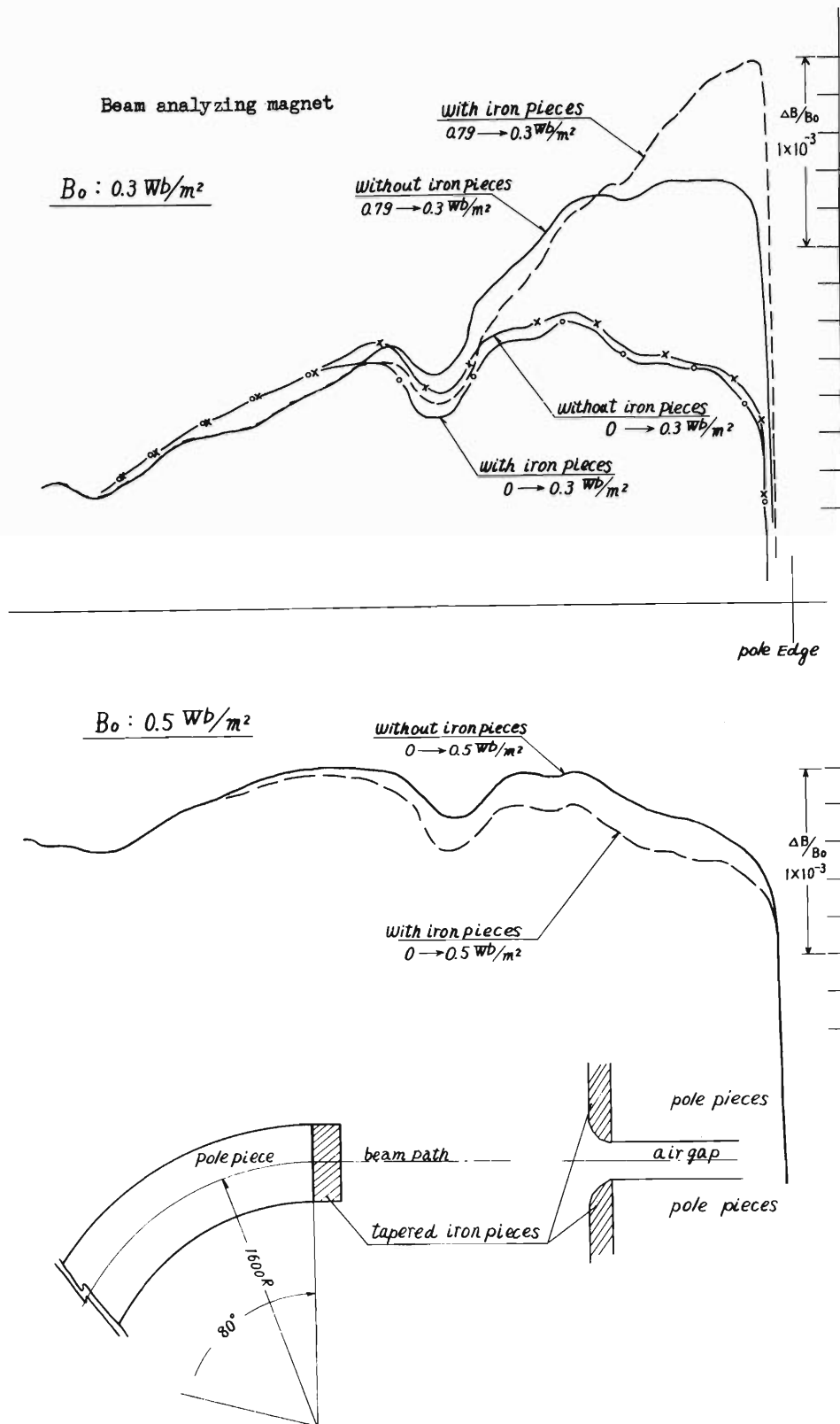


Fig. 3 (4-2) Improvement on the field distribution by attaching the iron pieces to an edge of the pole.

5. NUCLEAR PHYSICS

Scattering and Reaction

5-1. The $^{27}\text{Al} (^3\text{He}, ^3\text{He}) ^{27}\text{Al}$ and $^{27}\text{Al} (^3\text{He}, \alpha) ^{26}\text{Al}$ Reaction

M. Odera, I. Kohno, S. Takeda
and S. Nakajima

Differential cross sections of 21.3, 24.2 and 31.5 MeV ^3He particles elastically scattered by ^{27}Al in the angular range $15^\circ \sim 165^\circ$ have been measured, in order to obtain the accurate optical model parameters of ^{27}Al . Differential cross sections for $(^3\text{He}, \alpha)$ reactions were also measured.

An extracted ^3He beam from 160 cm cyclotron was energy analyzed, led into the 75 cm scattering chamber and focused on a target in a size of 1 mm x 8 mm. The energy resolution of the beam was 0.2% and the intensity was about $0.3 \mu\text{A}$. Thickness of target was $350 \mu\text{g}/\text{cm}^2$. Scattered particles were detected by silicon surface barrier detector and over all resolution was about 70 keV. In some angles the combination of the thin transmission type and the thick one was used to discriminate different kinds of particles. Fig. 1(5-1) is a pulse height spectrum. Excitation energies of residual nuclei are shown. Fig. 2 and Fig. 3(5-1) show the differential cross sections of elastically scattered ^3He and of α -particles. Distribution for the angles smaller than 100° of center of mass is in good agreement with hitherto-published data¹⁾. But, backward angular distributions of elastically scattered ^3He are apparently different with incident particle energy. At $E = 24.2$ MeV, backward rise is prominent, but at $E = 31.5$ MeV this is not seen. Forward angular distributions of various α -particles are very similar with each other for the peaks shown in Fig. 1(5-1), except for that of 0.418 MeV level. However, there is apparent difference in the backward distribution as shown in Fig. 3(5-1) in the case of transition to ground and 1.059 MeV state of ^{26}Al . These results suggest usefulness of the measurement of the backward angular distribution for the study of reaction mechanism and level structure.

Reference

- 1) D. J. Baugh, G. J. B. Pyle, P. M. Rolph and S. M. Scarrott: Nuclear Physics, A95, 115 (1967).
V. M. Pankratov and I. N. Serikov: Soviet Phys. JETP, 17, 604 (1963).

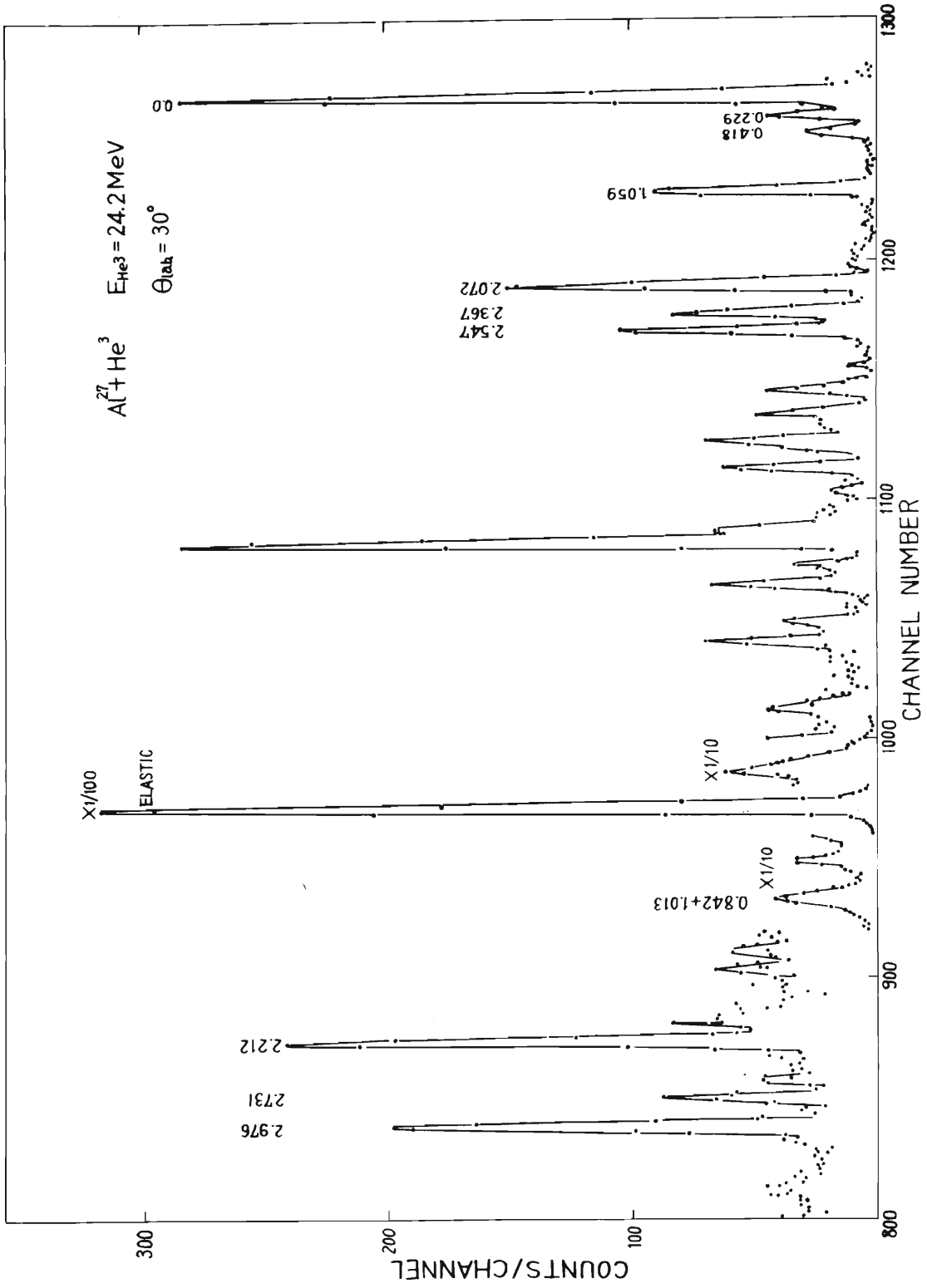


Fig. 1 (5-1) Pulse height spectra of ^3He and α -particles obtained at $\theta_{\text{lab}} = 30^\circ$ from the bombardment of ^{27}Al with 24.2 MeV ^3He particles.

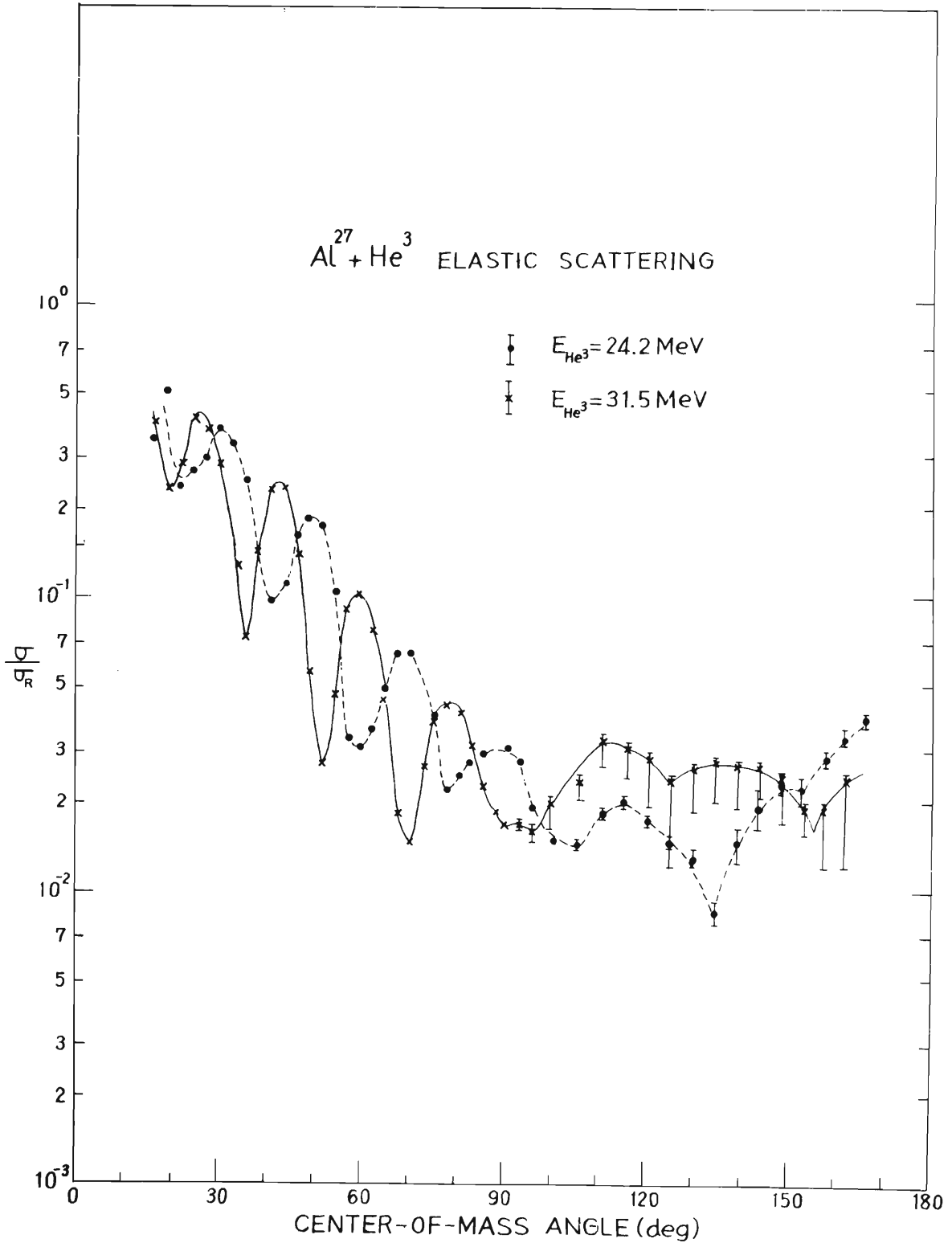


Fig. 2 (5-1) Angular distribution, expressed as σ/σ_R , for the elastic scattering of 24.2 and 31.5 MeV 3He particles.

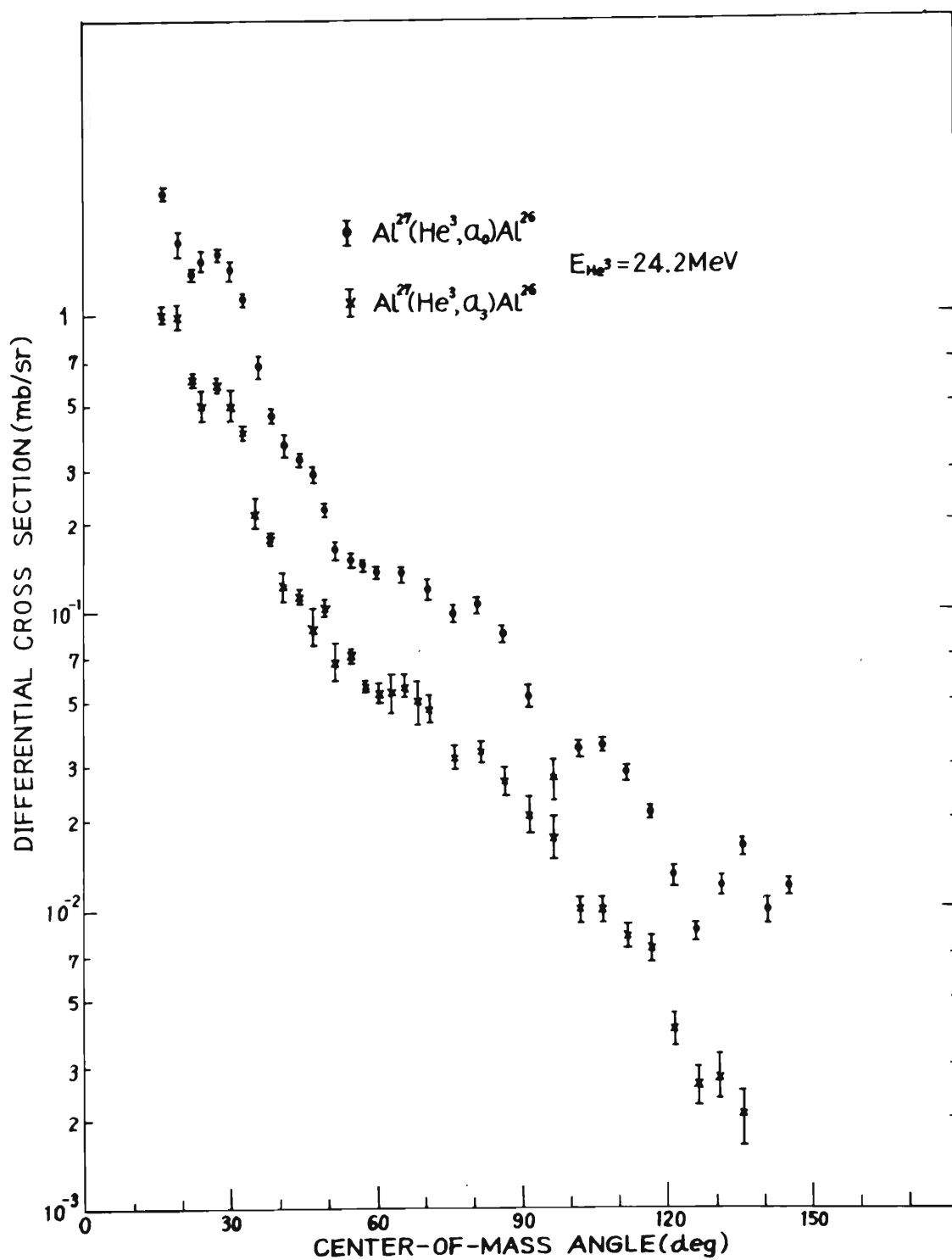


Fig. 3 (5-1) Angular distribution of α -particles for the $^{27}\text{Al}({}^3\text{He}, \alpha) {}^{26}\text{Al}$ reaction leaving ${}^{26}\text{Al}$ in the ground and third excited states.

5-2. Elastic and Inelastic Scattering of ^3He from Ni Isotopes

H. Kamitsubo, T. Fujisawa and T. Wada

The investigation of inelastic scattering gives a detailed information on the excitation mechanism and on the properties of the excited states. In the present work the elastic and the inelastic scattering to several lower states were measured over a wide range of energy. An external ^3He beam was energy analyzed, led into the 75 cm scattering chamber and focused on a target in the size of 1 mm x 2 mm. The energy resolution of the beam was about 0.2 % and the beam intensity was about $0.3 \mu\text{A}$. The scattered particles were detected by a single detector system of $1,000 \mu$ surface barrier unit, or a counter telescope system of 50μ transmission unit and $1,000 \mu$ lithium drifted unit. A small permanent magnet was put just before the detector system to reject the secondary electrons from the target. The overall resolution was about 70 keV without target thickness effects.

Targets of the separated isotopes were prepared by electrochemical deposition. An ambiguity of thickness due to target inhomogeneity was avoided as follows: forward angle scattering cross sections of ^3He were measured at 14.4 MeV and compared with calculated values of Coulomb scattering cross sections. Target thickness was thus determined within an accuracy of 5 percent.

Data were taken from 15° to 170° at 2.5° and 5° intervals. Typical angular distributions of elastic scattering from ^{58}Ni are shown in Fig. 1 (5-2) where differential cross sections are divided by the corresponding Rutherford cross sections. A spectrum of the scattered ^3He from ^{58}Ni is shown in Fig. 2 (5-2). As shown in the figure, levels at 1.45, 2.46, 3.04, 3.26 and 4.45 MeV are excited. Angular distributions of them are shown in Fig. 3 (5-2). A phase relation between three cross sections can clearly be observed. The measurements at other energies and with other targets are now in progress. The DWBA analysis of these data is being performed.

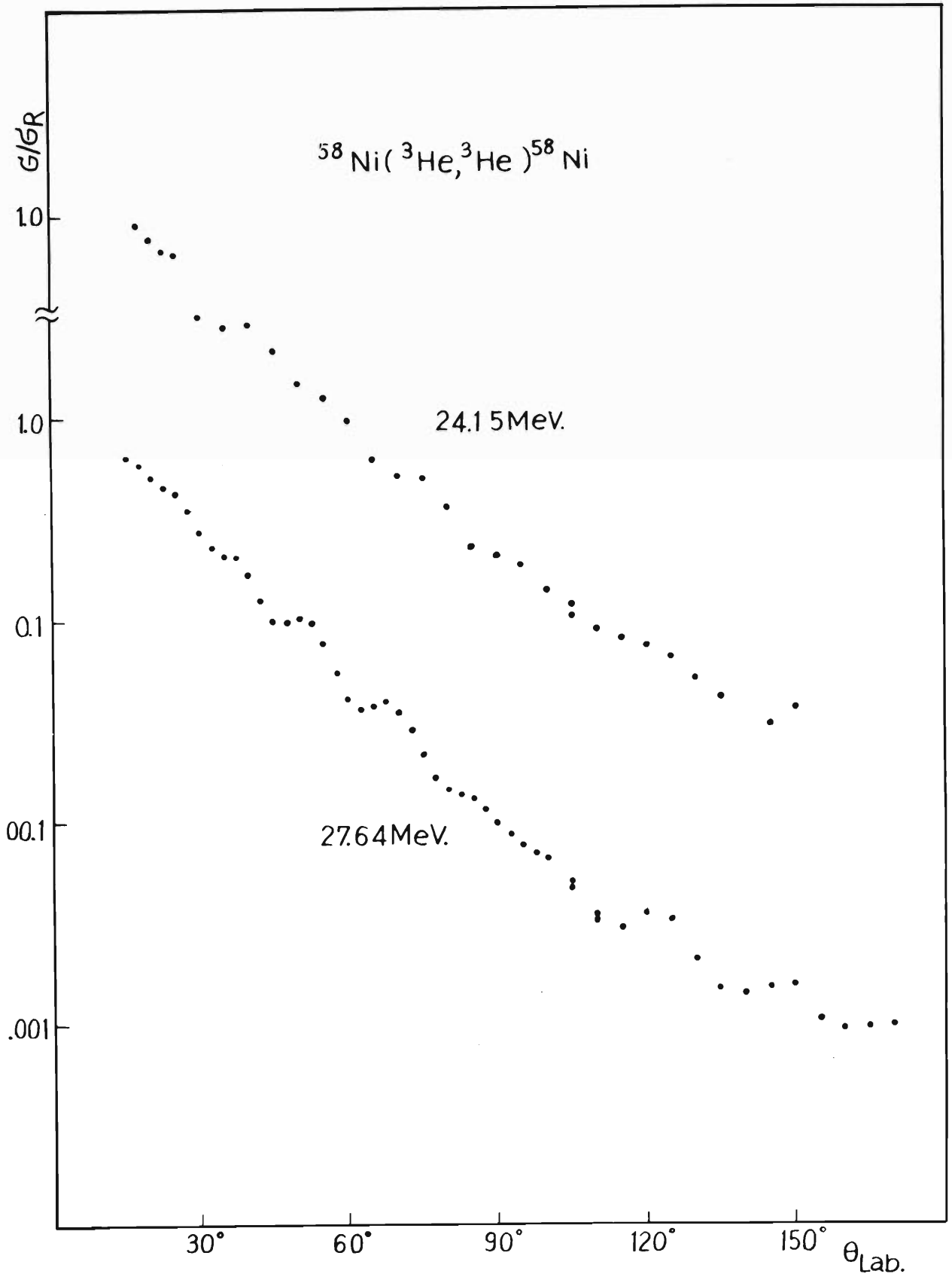


Fig. 1 (5-2) Angular distribution of the elastic scattering.

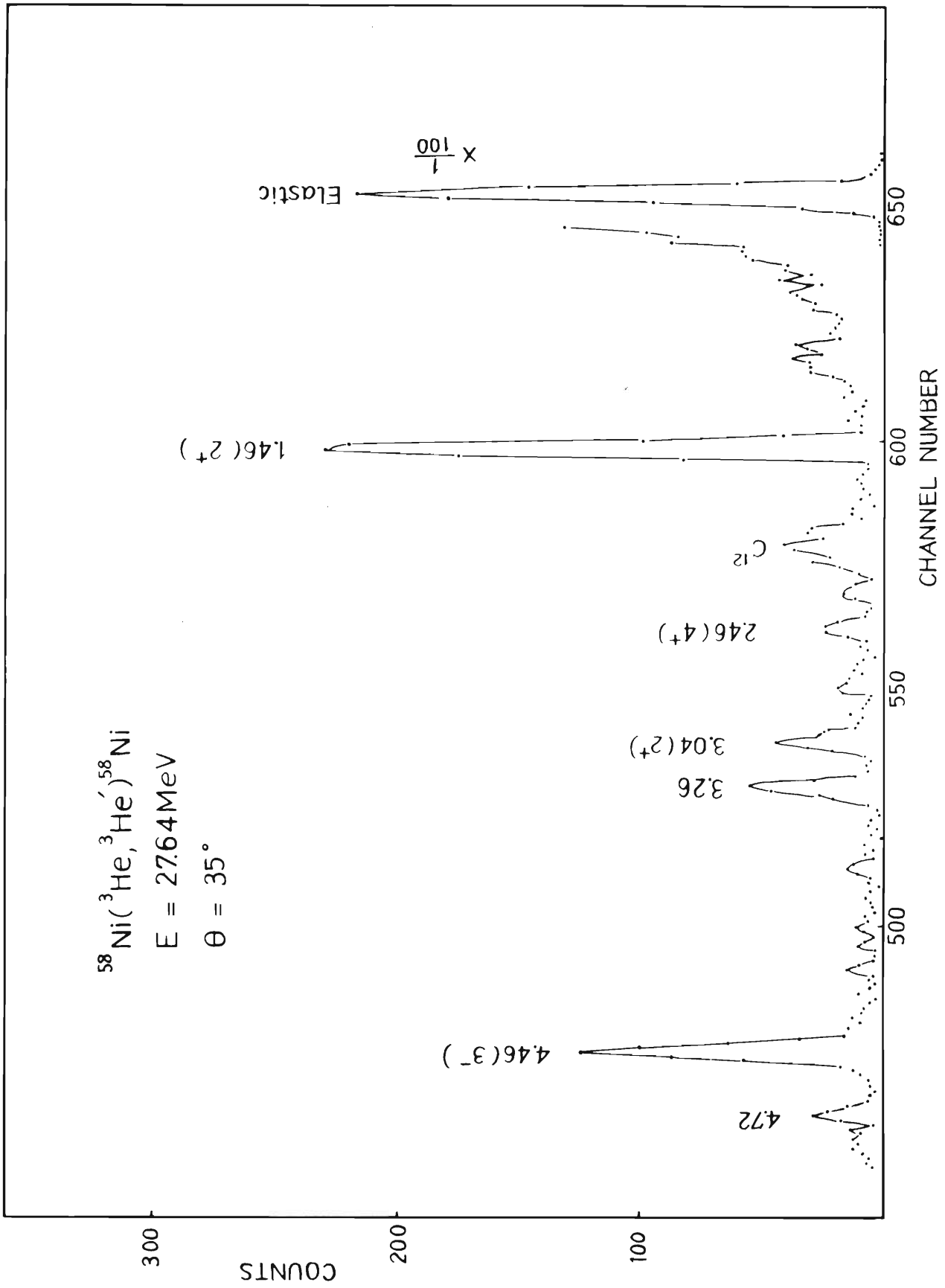


Fig. 2 (5-2) Pulse height spectrum.

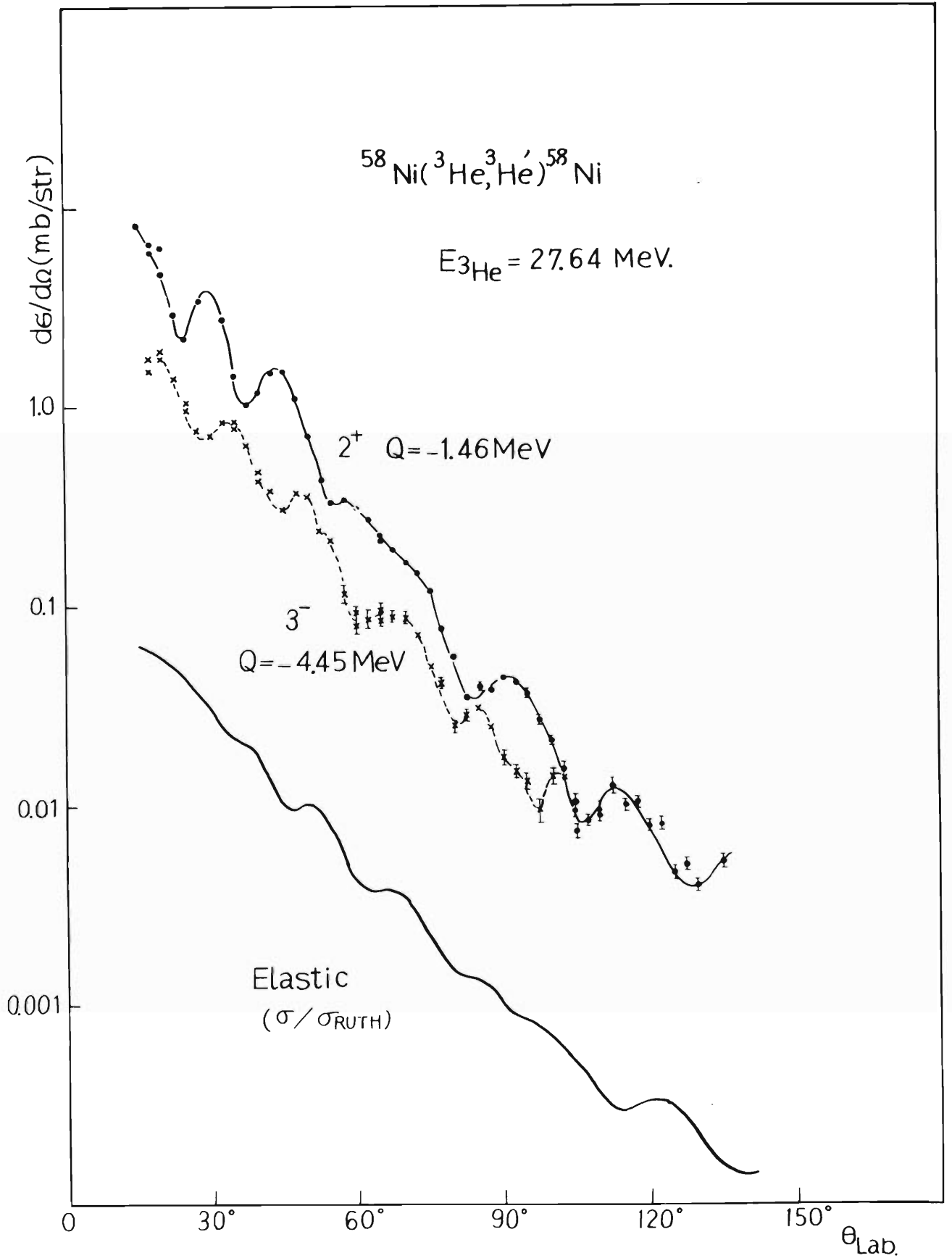


Fig. 3 (5-2) Angular distribution of the inelastic scattering.

5-3. Elastic Scatterings of ^3He from Ca

K. Matsuda, Y. Chiba, N. Nakanishi and Y. Awaya

The angular distribution of the elastic scattering of ^3He from natural calcium target was measured at four different incident energies, using the 75 cm scattering chamber and a solid detector telescope. This experiment was planned with two purposes. The first is the comparison with the elastic scattering of alpha-particles from Ca. The alpha-particles show an anomalous behavior at a backward angle, which cannot be explained by the simple optical model analysis. The experiment with ^3He , whose wave number corresponds to that of the anomalous alpha scattering, was considered as helpful to elucidate this strange effect. The second is to search the optical model parameters for the ^3He scattering. Recently, there have been published so many reports on the angular distribution of elastic ^3He and on the optical model analysis for ^3He . Few works, however, were performed on the energy dependence. Angular distribution at several different energies seems to be useful not only for the determination of the energy dependence of parameters, but also for the estimation of their magnitudes themselves. There is, for example, a well-known ambiguity on the real well depth.

The incident energies were 25.0, 30.0, 18.8 and 34.5 MeV. For the former two energies, the beam passing through the so-called 1st course (See 3-2) was used. In this case, the emitted particles were detected with a single surface barrier detector (ORTEC). It was found that the contamination of alpha-particles from the reaction of $^{40}\text{Ca} (^3\text{He}, \alpha) ^{39}\text{Ca}$ was not so small and at some angles the errors became very large. The poor resolution of the beam was then considered to be improved. Thus the analyzed beam (the 3rd course, see 3-2) was used in the experiments for the incident energies of 18.8, and 34.5 MeV. The scattering chamber had no front slit and a quadruple lens made an image of the defining slit of beam analyzer on the target. The dimension of the spot was about $3 \times 6 \text{ mm}^2$ and the energy resolution was about 0.2%. The obtainable intensity of ^3He beam in this case was $0.3 \sim 0.7 \mu\text{A}$. The self-support targets of calcium were made by evaporation and the thickness, which was about 1 mg/cm^2 , was determined from the measurements of weight and area.

The results are shown in Fig. 1(5-3). There was found no special backward anomalies in contrast to the alpha scattering. Optical analyses, using the INS code DWBA-2, have been tried. Very good agreements have not yet been obtained, since the automatic search routine is not available. Some of the results are shown in Fig. 2(5-3). The optical-model parameters are those of Bassel.

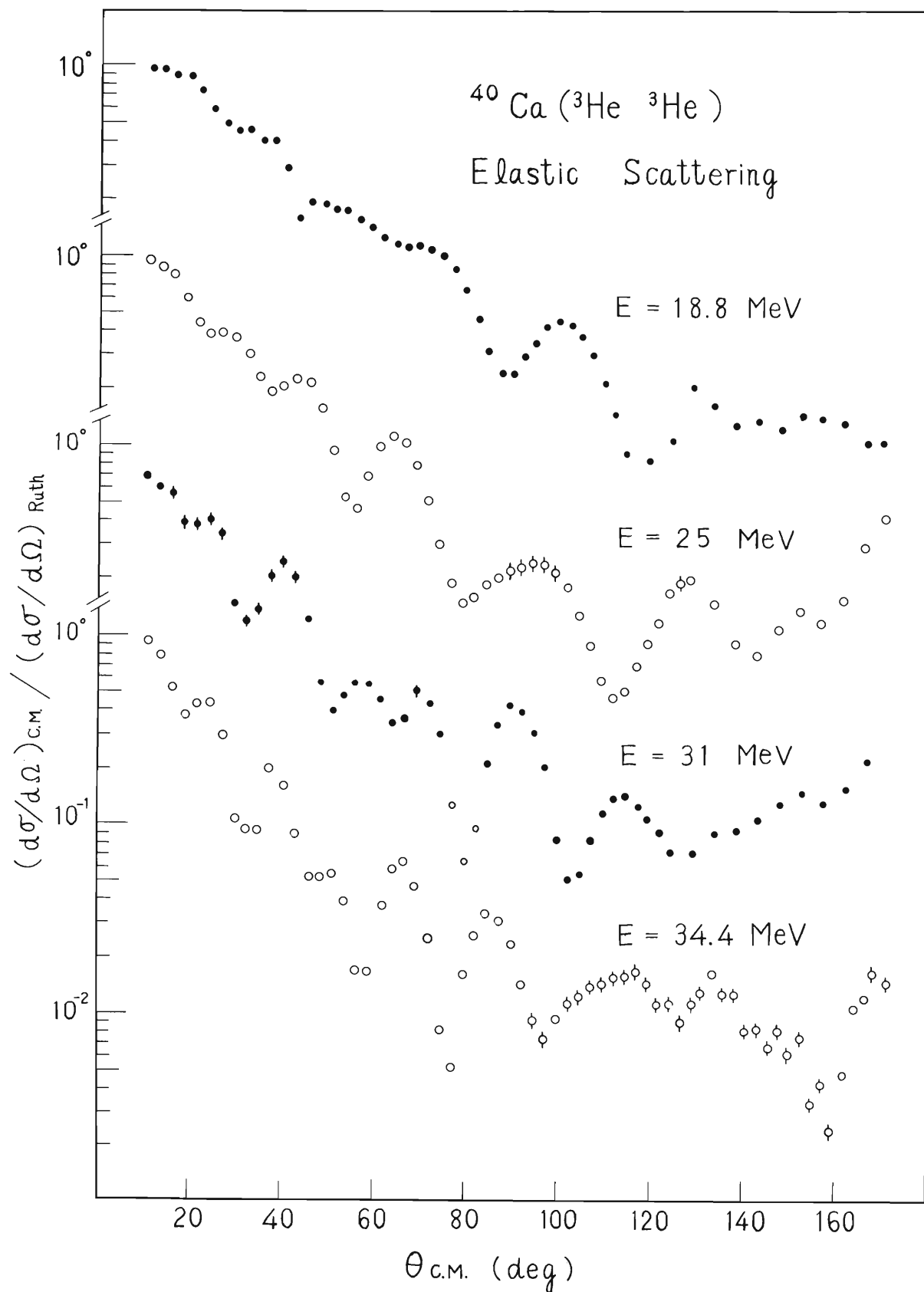


Fig. 1 (5-3) Angular distribution of the elastic scattering.

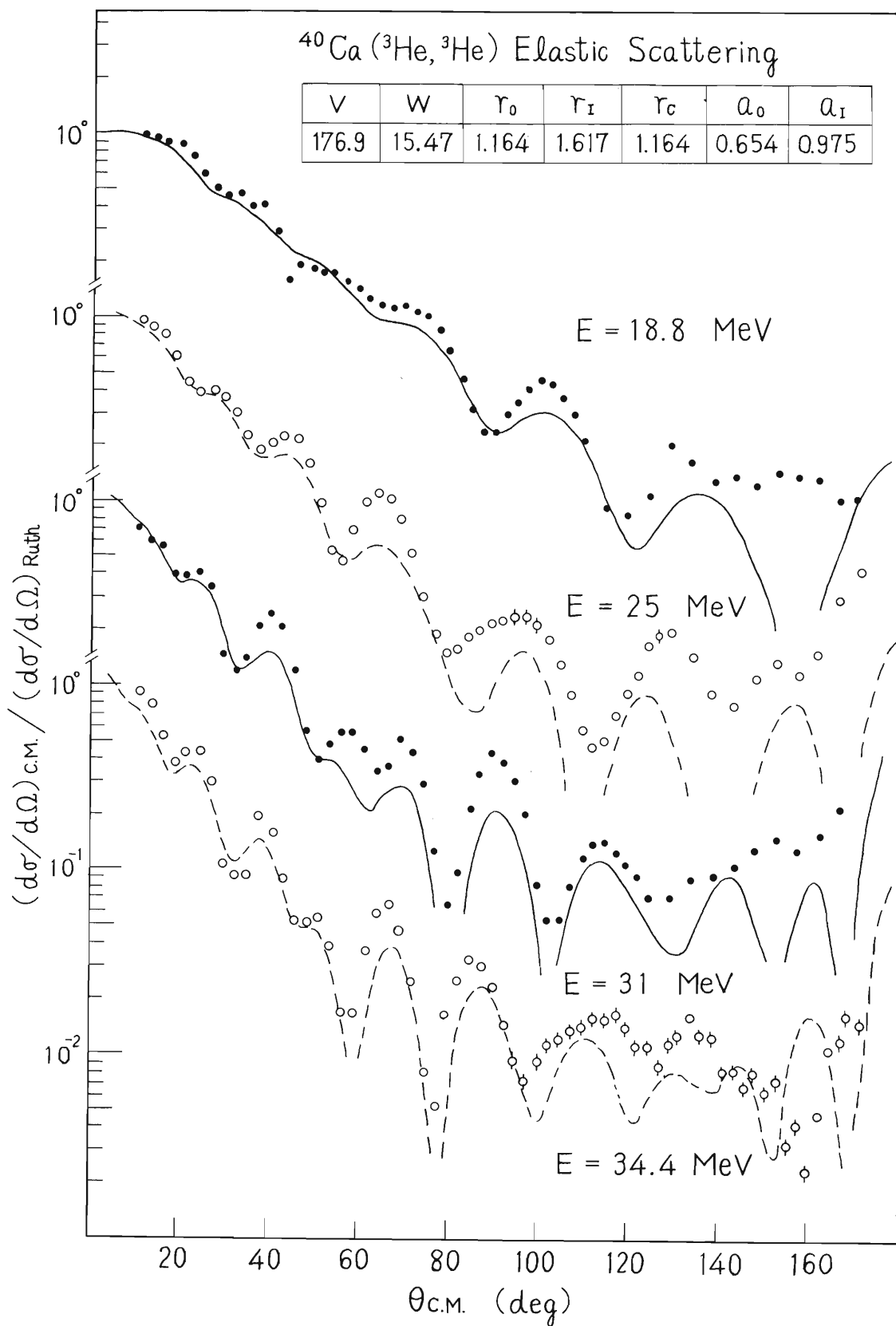


Fig. 2 (5-3) A preliminary fit of the angular distribution.

5-4. Coulomb Excitation with Alpha-particles

A. Hashizume, H. Kamitsubo, T. Inamura,
Y. Tendow, T. Kato, and K. Matsuda

The method of Coulomb excitation has been used extensively to explore the properties of the low-lying excited states. Especially the collective states of even-even nuclei have been widely studied by this method. In general the energy levels of odd nucleus are more complicated than those of even nucleus and the improvement of the energy resolution of the detector is important to distinguish the small differences of transition energies. We repeated the investigation of the Coulomb excitation of ^{197}Au by alpha-particles employing a lithium drifted germanium detector for the observation of gamma-rays. This nucleus has been studied by many authors and the transitions of 77, 191, 278 and 549 keV are known.

Since the transition probabilities and the low-lying energy level structure of ^{181}Ta are well known, this nucleus was chosen in the study as a check on the technique used.

Other targets, natural silver, palladium indium and platinum has been tested.

The beam of alpha-particles accelerated from 11 to 15 MeV have been transported by an ion optics system in a small irradiation room and focused into a spot of approximately 1 cm^2 in area. The beam current obtained on the target was about $0.1\ \mu\text{A}$.

Gamma-ray spectra were observed with a liquid-nitrogen-cooled lithium-drifted germanium detector of dimensions 10 mm in diameter and 4 mm in thickness, coupled to a low-noise pre-amplifier (TMC 100 c). The pulse heights were analyzed by a 1600 channel pulse height analyzer. The over-all energy resolution of this system was 7 keV (FWHM) for the 662 keV gamma-ray. The detector was placed at an angle of 70° to the direction of the beam, at a distance of 87 mm from the targets. The targets were placed in a vacuum chamber made of brass. The thickness of the window was 1.5 mm. The thickness of the detector window made of aluminum attached to the cryostat was 1 mm.

Figs. 1 and 2 (5-4) show the typical gamma-ray spectra for Ta and Ag excited with 11 MeV alpha-particles respectively. For Ta, the cascade gamma-rays, 165 keV and 135 keV, from $11/2^+$ state at 303 keV excited by E2 are completely resolved. For Ag, four prominent peaks are observed. The 325 keV and 427 keV gamma-rays are originated from ^{107}Ag . The 311 keV and 418 keV gamma-rays are emitted from ^{109}Ag . The origin of weak gamma-rays observed at 274 keV remains uncertain.

Fig. 3 (5-4) shows the gamma-ray spectra for Au excited with the same energy of alpha-particles. The known excited levels in ^{197}Au are shown in Fig. 4 (5-4).

The 77, 191, 279 and 549 keV gamma-rays have been observed by previous Coulomb excitation experiments. In addition to these gamma-rays, 93, 155, 199 and 267 keV photons are observed. The 267 keV gamma-ray is the cross over transition from 268 keV to ground state. It is likely that there exists the 270 keV transition from 539 keV state to 279 keV state but the corresponding gamma-ray is not resolved. The 199 keV gamma-ray is the transition from the 279 keV state to the first excited state. It is possible that 155 keV gamma-ray is the photon observed by Friesacker and Roy in the

study of ^{197m}Pt decay. But this gamma-ray has not been observed in the more detailed work of Haverfield et al.

For the levels in ^{197}Au , Braunstein and de-Shalit have proposed a core excitation model in which the quadruplet ($1/2, 3/2, 5/2, 7/2$) arises from the coupling of a $2+$ core-excitation with $d_{3/2}$ proton. Kisslinger and Sorensen have also discussed these levels from the point of view of the shell model taking into account of the Q-Q interaction. The determination of E2 transition probabilities may become the sensitive test of these models for ^{197}Au .

Table 1 shows the relative gamma-ray intensities of these thick targets at 70° . These intensities are normalized in each spectrum to the most intense gamma-ray.

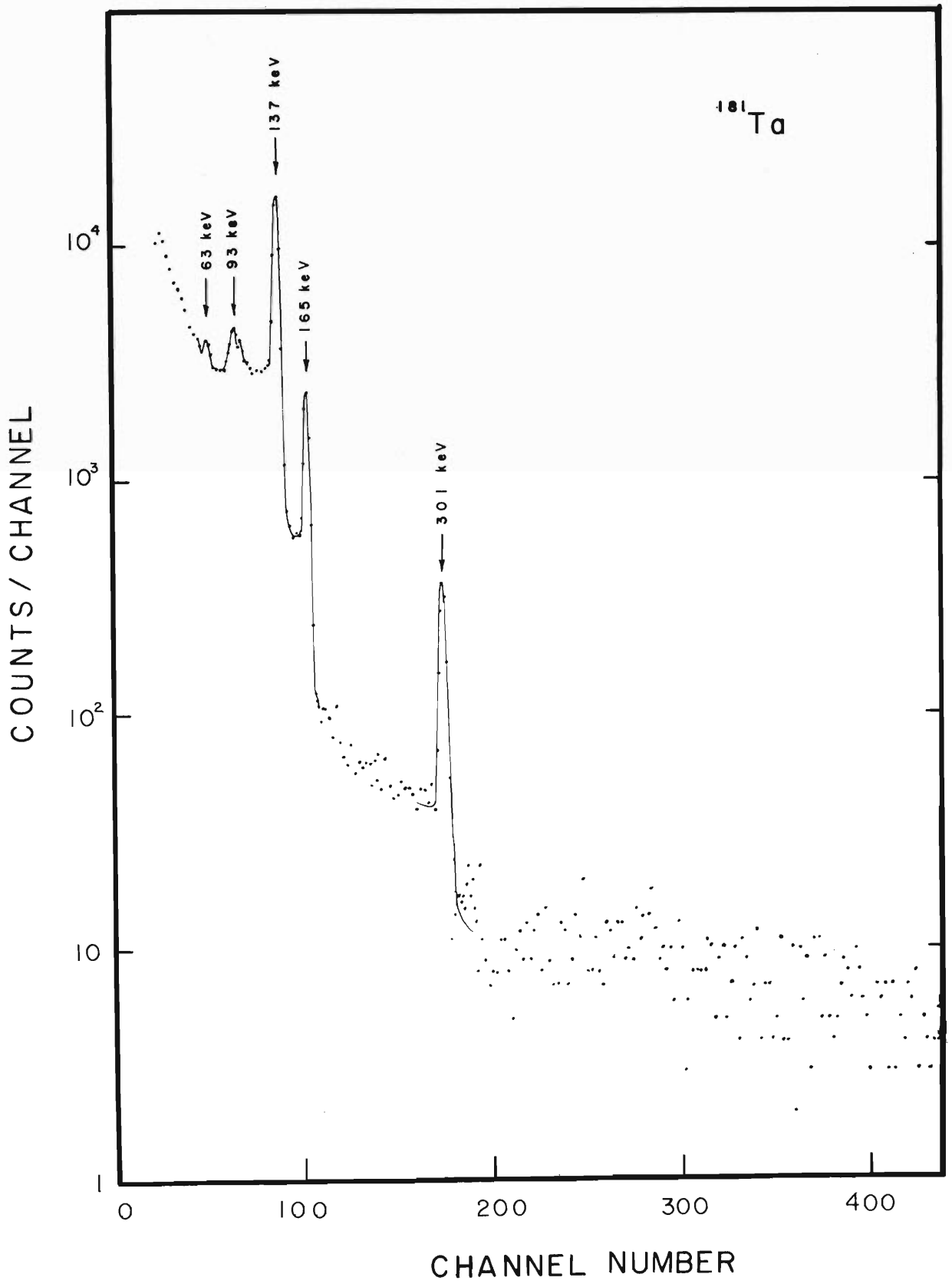


Fig. 1 (5-4) Gamma-ray spectrum of ^{181}Ta .

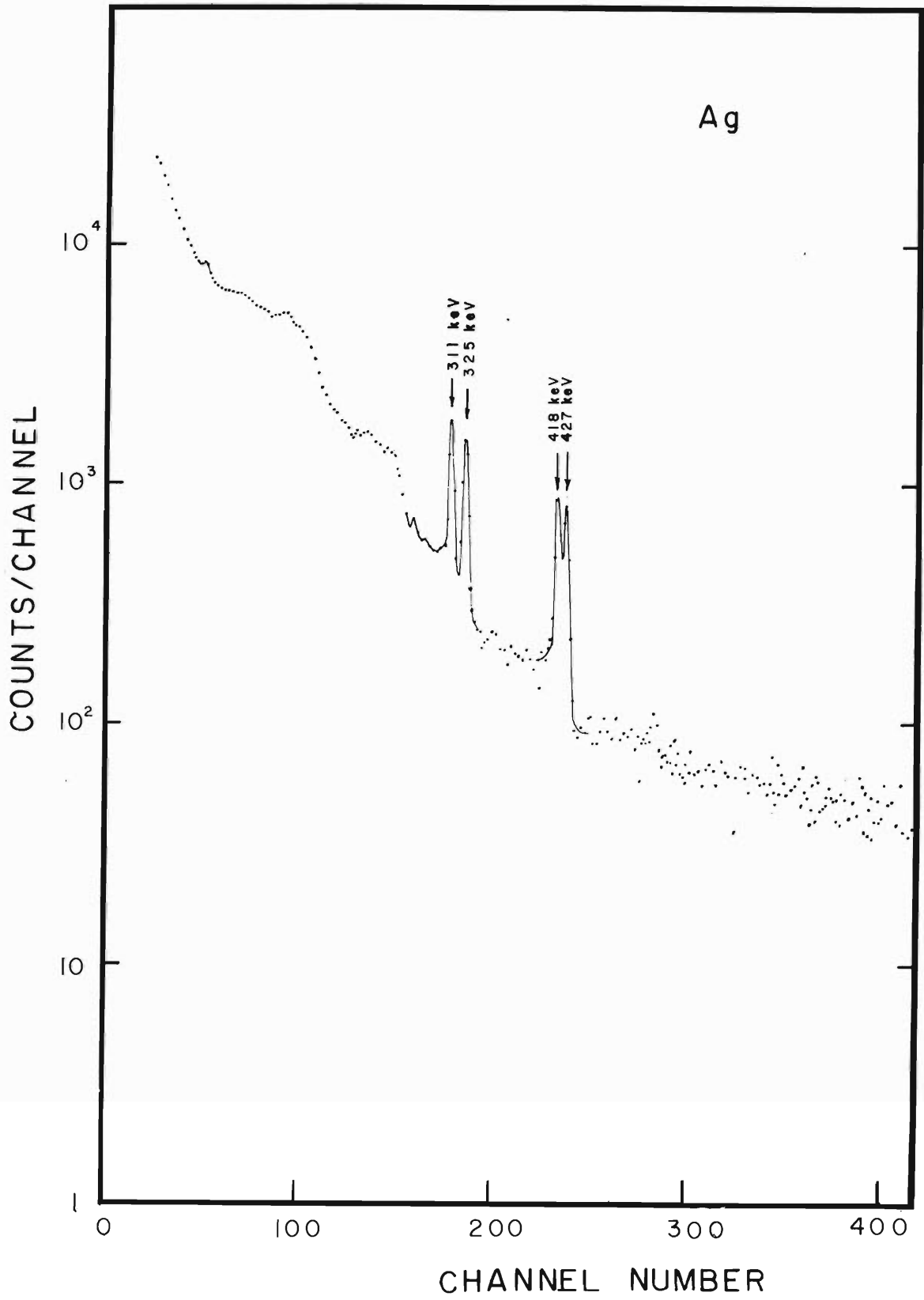


Fig. 2 (5-4) Gamma-ray spectrum of Ag.

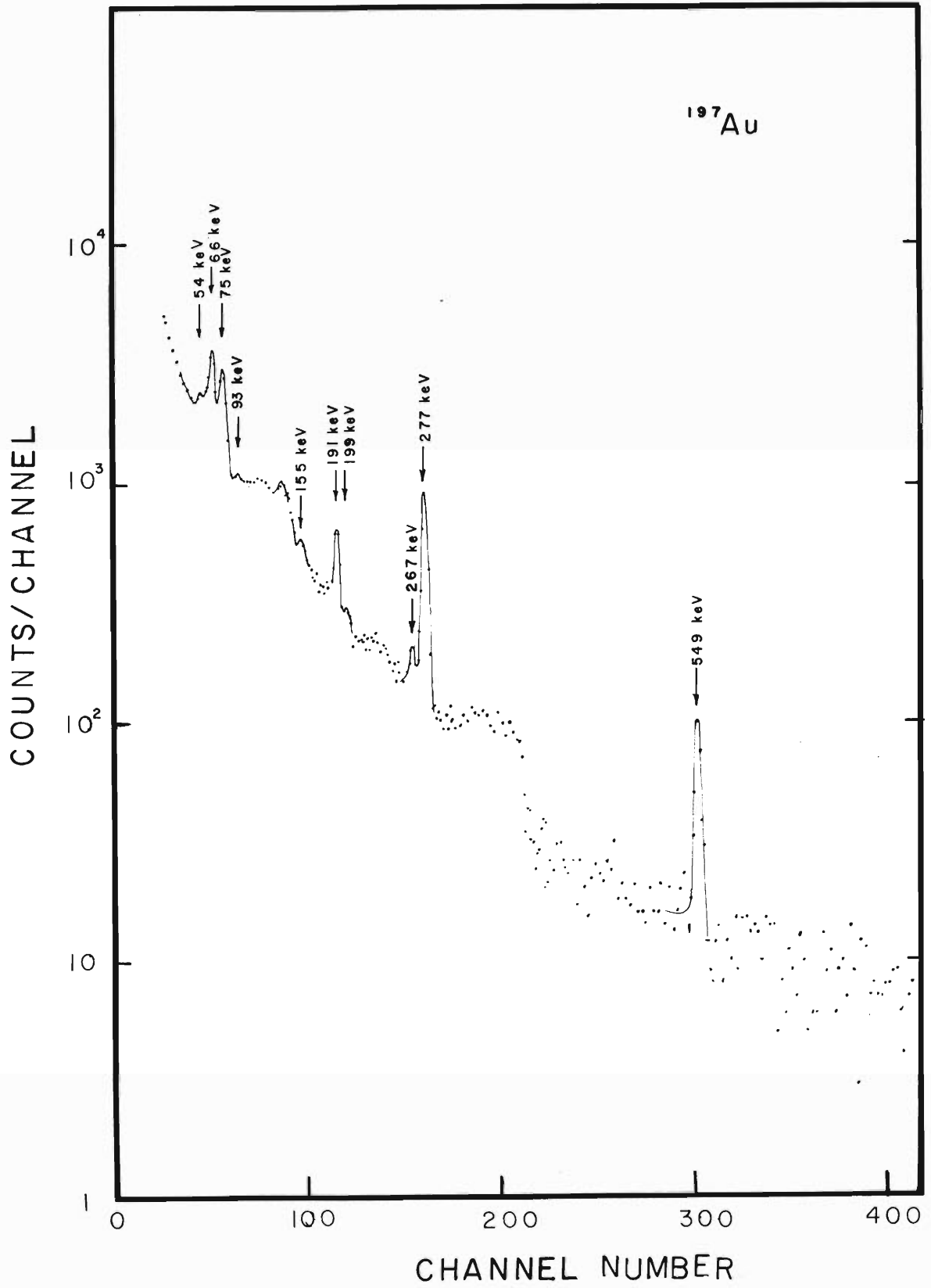


Fig. 3 (5-4) Gamma-ray spectrum of ^{197}Au .

6. NUCLEAR PHYSICS

Nuclear Spectroscopy and its Applications

6-1. Measurements of Internal Conversion Electrons

Y. Tendow and A. Hashizume

Recently a high precision, high resolution air-core beta-ray spectrometer has been completed in the cyclotron laboratory and its performances and characteristics are now under extensive examination. The spectrometer was originally intended to be used for routine work with a resolution of $\sim 0.05\%$ region. But this resolution already surpasses the values attainable with iron-core spectrometers by five times or in some cases by ten times. According to preliminary data, a $\sim 0.03\%$ FWHM resolution in momentum can be attained constantly without special efforts using the 661.59 keV transition in ^{137m}Ba . The source was made by a liquid drop deposition method.

It is now possible to study internal conversion electrons in a more detailed manner than previously known. In consequence, a possibility of obtaining new informations is promised in nuclear spectroscopy. Among them, the L-subshell conversion coefficient ratios are especially useful for removing ambiguities in nuclear spin parity assignments. The results of precise measurements of subshell ratios and transition energies together with some necessary coincidence data are enough to establish a reliable level scheme in ordinary cases. Precise measurements of subshell ratios also give a means to search for fine nuclear structure effects on conversion process, such as the penetration effects and electric monopole transitions.

Prior to routine operations, the spectrometer have to be calibrated with several standard conversion electron lines. The 411.795 keV transition in ^{198}Hg was used to calibrate the potentiometer readings with respect to magnetic rigidity $B\rho$ for electrons. The source was made by evaporating natural Au on an aluminum foil and irradiating with neutrons of 2×10^{13} n/sec/cm² for a week in the JRR-2 reactor of Japan Atomic Energy Research Institute. Source dimensions are 0.3 mm in width and 20 mm in length. The source thickness is difficult to estimate but it may be presumed to be less than 0.1 microns.

The K, L_I, L_{II} and L_{III} line measurements were made in the current range 3 (from 8A to 32A). A typical line spectrum measured is shown in Fig. 1 (6-1). The ultimate resolution attained with this source was 0.026% with a baffle of 20 mm and a slit of 0.25 mm.

Table 1.

	$B\rho$ (G · cm) ¹⁾	Potentiometer readings
K	2222.521	0.25426
L _I	2503.384	0.32852
L _{II}	2505.955	0.32918
L _{III}	2513.716	0.33126

The magnetic rigidities and the potentiometer readings of four conversion lines of 411.795 keV transition are shown in Table 1. The relation between $B\rho$ and the potentiometer reading N in the current range 3 (3A to 32A) derived from the values in the table is given by

$$B\rho = 3282.4 N + 1260.8 \text{ G} \cdot \text{cm},$$

where N is zero for 8 A and 1 for 32 A. The constant term in the right-hand side of the equation corresponds to the $B\rho$ value for 8 A. This calibration relation is valid only in the range 3. In other current ranges calibration must be made by using pertinent transitions.

The L-subshell ratios are obtained from the spectrum in Fig. 1 (6-1). The transition is known to be of pure electric quadruple (E2). The theoretical subshell ratios are interpolated referring to the Sliv's table, and given by

$$L_I : L_{II} : L_{III} = 22 : 23 : 10.$$

The experimental values in the present work are

$$L_I : L_{II} : L_{III} = 21.9 : 23.6 : 10,$$

which are in good agreement with pure E2 values.

Reference

- 1) G. Murray, R. L. Graham and J. S. Geiger: Nucl. Phys., 63, 353 (1965).

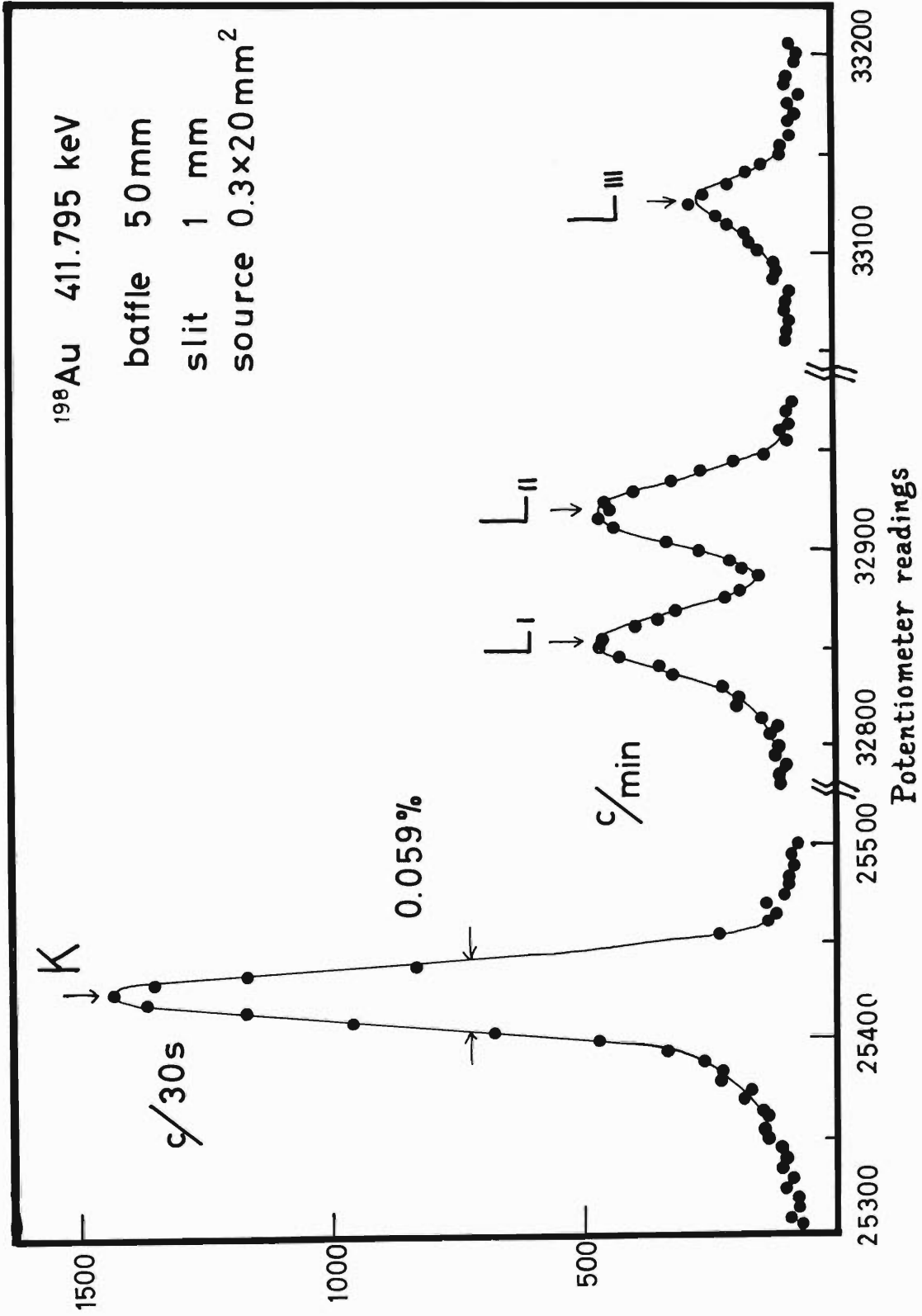


Fig. 1 (6-1) Momentum spectrum of the conversion electrons from ^{198}Au .

6-2. Nuclide Analysis using Nuclear Reactions

T. Hamada, M. Okano, A. Hashizume,
Y. Awaya, Y. Tendow, and T. Kato

The characteristics of radiations accompanying nuclear reaction and/or coming from the produced radioactive nuclei are specific for the reaction and the target nuclide involved. A preliminary experiment on the nuclide analysis based on the above principle has been made.

The gamma-ray energies were measured mainly with a scintillation gamma-ray spectrometer having two types of the scintillation detectors: one is a 3 in ϕ x 3 in NaI (Tl), and the other a 1 \sim 3/4 in ϕ x 2 in NaI (Tl) combined with a 6 in ϕ x 6 in NaI (Tl) annular crystal for the pair spectroscopy.

Several light nuclides of practical interest were bombarded in the small irradiation room by 8 MeV protons through a No.5 beam duct, and the effect of background radiations were studied. The background contribution was found to be fairly reduced by the lead shield except for that of neutrons.

7. NUCLEAR INSTRUMENTATION AND TECHNIQUES

7-1. The 75 cm Scattering Chamber

T. Fujisawa and Y. Awaya

The scattering chamber has been designed and constructed for universal use in the experiments on nuclear scattering and reaction. A sectional view of the scattering chamber is shown in Fig. 1 (7-1). The chamber is 75 cm in inner diameter and 54 cm in inner depth and its main parts are made of chromium plated steel. The whole scattering chamber can be rotated around the direction of the incident beam and moved horizontally and vertically. The side and top views of the scattering chamber are shown in Figs. 2 and 3 (7-1).

The side wall, the bottom plate and the top lid of the chamber have five, three and four windows, respectively. The chamber contains a supporter of the target holder, a turn table and a turn arm. The axes of them are concentric within an accuracy of 0.1 mm. These three parts are connected to the lower lid through a bellows and are not fixed to the lid, but are supported by the frame. Thus the essential parts of the scattering chamber are not influenced by the shrinkage of the vacuum chamber. The detectors and other equipments used in the experiments can be attached to the turn table, turn arm and windows. By using the turn table and/or turn arm, the emitted particles and radiations can be observed at any angle except at an extreme one, with respect to the incident beam continuously. The turn table is supported by the side wall at its rim and under a concentrated load of 50 kg. The adjustments of the vertical position of the target, and of the angles of the turn table and the turn arm can be made without opening the vacuum system. The angle of the turn table can be read with accuracy of 0.05° and the angles of the target and the turn arm can be read with accuracy of 0.5° . The chamber also contained a collimating system of the incident beam but it has been removed now.

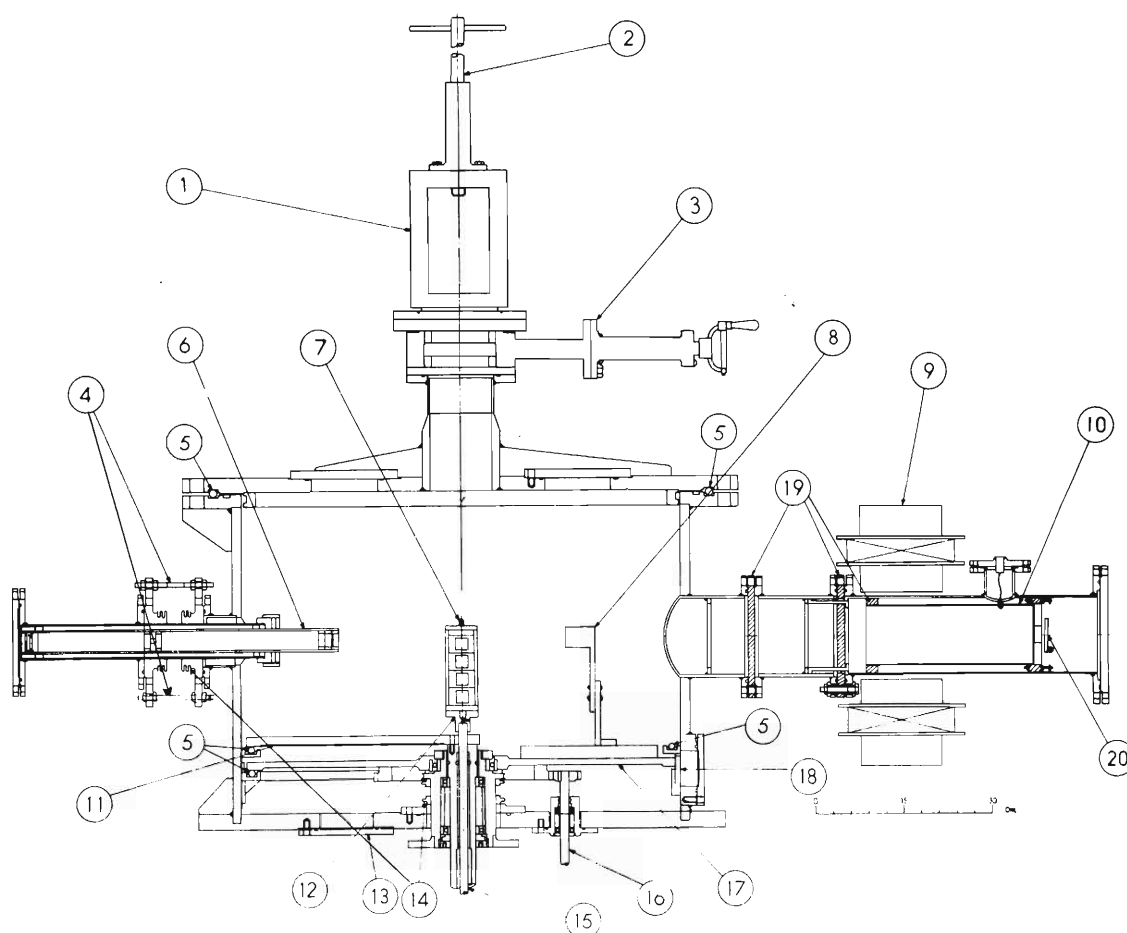
The Faraday cup which is insulated from other parts is connected to the chamber to measure the beam current. The resistance of the insulator is more than $2,000 M\Omega$ at 500 DC.V. The aperture of the cup is 10 cm in diameter and 30 cm in length. The distance between the target and the entrance of the Faraday cup is about 70 cm. In order to take away the effects of the recoiled electrons, a magnet (300 Gauss) is placed at the entrance of the cup.

On the top lid of the chamber, a target box is connected through a gate valve. The target holder can be drawn into the box and the target is changed without destroying the vacuum. This box can be used as the evaporating system also when the targets are mounted on the holder without being exposed to the atmosphere.

The chamber is evacuated by a series of mechanical booster pump and rotary pump to a vacuum of about 10^{-2} mmHg. Then the chamber is connected directly to the vacuum system of the beam transporting system which maintains the vacuum under 10^{-4} mm Hg.

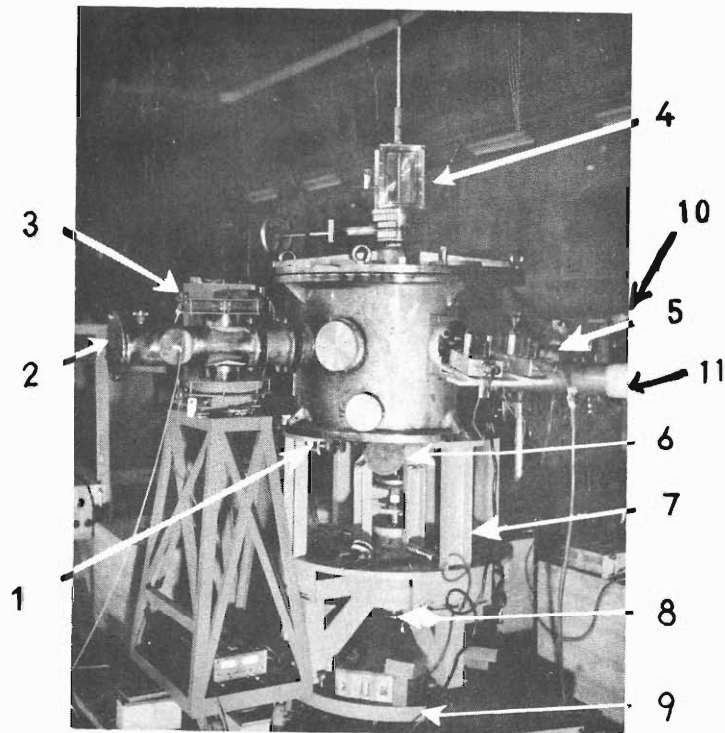
Acknowledgments

We wish to thank Dr. Y. Hashimoto for his kind advice, Mr. T. Wada for his help in making accurate measurement, and Mr. S. Fujita for his trouble in drawing Fig. 1 (7-1).



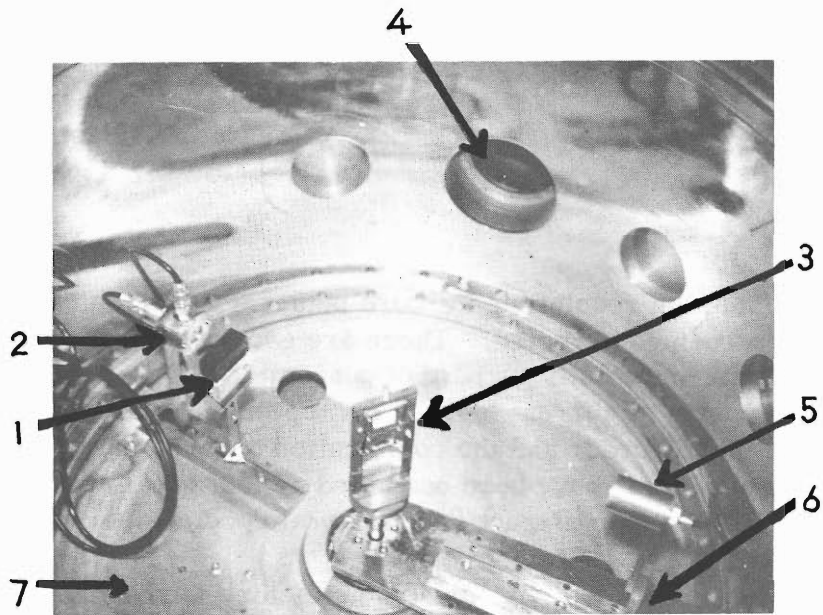
(1) Target box (stainless steel), (2) Rod for introducing and taking out targets (stainless steel), (3) Gate valve (stainless steel), (4) Bolts for adjusting the collimator, (5) Ball bearings, (6) Collimator of incident beam, (7) Target holder which can hold four kinds of targets at the same time, (8) Holder of the solid state detector, (9) Magnet which produces magnetic field of about 300 gauss and takes away the effects of recoiled electrons yielded at a target and the Faraday cup in the measurement of the transmitted beam, (10) Faraday cup, (11) Turn arm, (12) Base of the target holder, (13) Flange with vacuum tight BNC connector, (14) Bellows, (15) Target stanchion which can be slid up and down at about 10 cm and rotated at 360°, (16) Shaft for turning the turn table, (17) Turn table which can support the load of 50 kg rigidly and can be rotated at 360°, (18) Vernier of turn table which can be read with an accuracy of 0.05°, (19) Acryl insulator, (20) Beam stopper (copper) which can be opened to see the slit of the beam transporting system to adjust the alignment of the chamber.

Fig. 1 (7-1) Sectional view of chamber.



(1) Handle to drive the turn table, (2) Faraday cup, (3) magnet for the Faraday cup, (4) Target box, (5) Pre-amplifier of the solid state detector, (6) Handle to drive the turn arm, (7) Turn base to rotate the chamber, (8) Handle to slide up and down the target station, (9) Base plate to move the center of the chamber horizontally and vertically, (10) Beam duct to the cyclotron, (11) Duct to the pumping system.

Fig. 2 (7-1) Side view of chamber.



(1) Permanent magnet to take away the effect of recoiled electrons produced at a target, (2) E and ΔE solid state detectors, (3) Target holder on which a Ni target and a disk of quartz are mounted. The beam spot on the quartz can be seen with T.V. at the counting room, (4) Aperture to the Faraday cup, (5) Solid state detector for monitor, (6) Turn table, (7) Turn arm.

Fig. 3 (7-1) Top view of chamber.

7-2. An Air-core Beta-ray Spectrometer

Y. Tendow, A. Hashizume, and Y. Awaya

Instrumental

A high precision, high resolution air-core beta-ray spectrometer with a mean radius of 50 cm has been constructed. There are two ways to create a double focusing magnetic field with air-core coils: a pair of concentrically coupled solenoid coils or an array of several pairs of current loops. An "optimum field" which makes the aberrations zero to the higher order and the combination of three pairs of current loops to generate the "optimum field" have been computed up to a great accuracy¹⁾. Such an exact computation has led to construction of several spectrometers of the current loop type in the world.

We adopted the current loop type spectrometer for the reason that it is possible to fit the magnetic field to "optimum" one to the higher order and to access easily to the source and detector regions. The mean radius of 50 cm is a compromise between contradictory requirements: a demand for a larger mean radius to gain a higher luminosity and that for a smaller radius to limit the cost and to attain easy handling. The spectrometer is aimed at to work with line widths of some 0.05 % region in momentum rather than to attain an extremely high resolution. A resolution better than $\sim 0.02\%$ is rarely needed in practice because of the low counting rates.

The coil array consists of three pairs of current loops: large pair, medium pair and small pair. The current conductor is an aluminum strip of 32 mm in width and 2.475 mm in thickness, which is wound on water-cooled aluminum bobbins with glass fiber sheets as insulators and myler strips between each turns. The large coil and medium coil have four sections and each section has 56 and 24 turns respectively. The total turns are 448 and 192 respectively. The small coil has two sections of 25 turns each and 100 turns in total. The field expansion coefficients a_n with the actually manufactured coil array fit to those of "optimum field" to the fourth order within acceptable tolerances.

The vacuum chamber is made of aluminum and has three baffles, one radially adjustable and two non-adjustable. The radially adjustable baffle is placed at the midway of the electron path and has an aperture edge profile of 0.04 % resolution iso-aberration contour. The chamber is evacuated to a pressure of 5×10^{-6} mmHg with an 8-inch diffusion pump located at 8.5 meters from the center of the spectrometer.

A transistor-controlled stabilized current power supply of 140 V, 100A at maximum is employed as an exciting current source. The exciting current is stabilized to 10^{-5} per an hour. Five current ranges can be selected by knife switches by shunting the standard resistor stepwise. The current is increased by a precision automatic stepping potentiometer with a minimum step of 7.5×10^{-6} of the maximum current in a selected range. In an automatic scanning performance the starting value, the goal value and the stepping amount of the current can be selected arbitrarily by a matrix of push buttons.

A closed circuit cooling system with distilled water controls the coil temperature.

The distilled water coolant flows successively through a heater, a heat exchanger, cooling channels in coil bobbins, a reservoir and an ion-exchanger column. The coolant exchanges heat in the heat exchanger with city water chilled to a temperature of 10°C. The temperature rises in the coils with a current of 85 A (3.5 MeV for electron energy) do not exceed 2.5°C.

A side-window type G. M. tube with a ~ 1 mg/cm² mica window is used as a detector. The counting and printing are automatically controlled in connection with the current scanning operation.

Because of the high resolution and the low magnetic field of the spectrometer, the earth's field (0.35 gauss for vertical component and 0.3 gauss for horizontal) and other stray fields cannot be ignored especially for low energy electrons. The degaussing coil system consists of a pair of current loops for vertical component: two pairs of current loops for south-north and a pair of rectangular coils for east-west. The vertical component is eliminated to less than 5×10^{-4} gauss.

The spectrometer is installed in a specially designed non-ferrous building located at about 100 meters from the magnet of the IPCR 160 cm cyclotron. The spectrometer room is 6.3 meters by 6.3 meters in area and 3.2 meters above the floor and 1.3 meters below the floor. A portion of the degaussing coil system is installed under the floor. The cyclotron leakage field at the maximum excitation of 2×10^4 gauss is about 3×10^{-3} gauss at the spectrometer site. The earth field nullification is performed manually before the measurement of electron momenta with monitoring by a flux-gate type fieldmeter. A system for automatic cancellation of external field is now being planned.

Performances

As has been stated, the spectrometer is aimed at operating with a resolution of ~ 0.05 % FWHM in momentum. The dimensions of actually manufactured coils, however, turned out well with tolerances of much smaller than previously permitted and therefore the resolution of about ~ 0.02 % became expectable in some favorable conditions.

The spectrometer performances were examined by using K, L and M conversion lines of 661.59 keV transition in ¹³⁷Ba. A drop of CsCl solution was deposited on an Au evaporated mylar film and heated to dryness with a flood lamp. The source thus manufactured was 0.4 mm in width and 10 mm in height. Although the thickness and the uniformity of the source were not so satisfactory, the ultimate resolution attained was 0.025 % FWHM with a baffle aperture of 10 mm and a slit width of 0.2 mm. The transmission measurements and the current-momentum calibration are now being undertaken using ¹³⁷Cs, ¹⁹⁸Au and ²⁰³Hg sources.

Reference

- 1) G. E. Lee-Whiting and E. A. Taylor: Can. J. Phys., 35, 1 (1957), AECL No. 381 (1958).

7-3. A Broad Range Magnetic Analyzer

N. Nakanishi, S. Motonaga,
M. Hemmi and K. Matsuda

A magnetic analyzer for nuclear reaction particles has been designed and is under construction. Various types of reaction particle analyzing magnets have been developed to meet the need for high precession in nuclear physics. In general, a magnetic analyzer is required to attain brighter luminosity, higher resolution and broader energy range. Certain types of a single magnet such as the Browne-Buechner type¹⁾, the Elbek type²⁾ and the Siegbahn type³⁾ have been widely used.

The magnetic analyzer newly designed will be installed for the IPCR cyclotron and an array of multiple detectors will be employed as a detector system. The following points are considered in designing the analyzer; (1) remarkable dispersion, (2) small vertical magnification, (3) linearity of focusing line and (4) high luminosity and high resolution. More optical parameters are required to realize better conditions in optical properties. So a combination of two homogeneous sectorial magnets with circular pole boundaries was considered.

In such a complex configuration of magnetic fields it is difficult to find an intuitive or a simple analytical relation between the parameters and the ion optical properties. So calculations were made by the trial and error method with a computer. The approximation of a sharp cut-off boundary is assumed throughout this work.

A magnetic field configuration obtained is shown in Fig. 1 (7-3) and notations used are summarized in the same figure. The optical properties of the magnetic analyzer are as follows: The energy range covers from E_{\max} to $0.67 E_{\max}$. The average energy resolution calculated is less than 1×10^{-3} when the solid angle is 2.5×10^{-3} steradian. The vertical magnification is about 2 and the dispersion factor about 6.

Both of the magnets have an air gap of 58 mm and their maximum $B \cdot \rho$ and magnetomotive force are 110×10^4 gauss \cdot cm and 7.5×10^4 ampere-turns, respectively. One of them (PA-I) is 32 t and the other (PA-II) is 30 t in total weight.

The analyzing magnet will be rotated over an angle from -15° to 150° around the center of a 460 mm ϕ scattering chamber.

Several shims, which approximate to a circular boundary by stepped one, are mounted at the entrance and exit with a curved boundary. Paramagnetic spacers of 5 mm are installed to homogenize the magnetic field at the upper and lower sides between a pole piece and a yoke. The grade of parallelism of the pole face is achieved at 0.01 mm and therefore it is expected that the grade of inhomogeneity of the field is less than 5×10^{-3} . Stretch-wire method will be employed in examining ion optical properties of the magnet.

References

- 1) C. P. Browne and W. W. Buechner: *Rev. Sci. Instr.*, 27, 899 (1956).
- 2) J. Borggreen, B. Elbek and L. P. Nielsen: *Nucl. Instr. and Meth.*, 24, 1 (1963).
- 3) N. Svartholm and K. Siegbahn: *Ark. Mat. Astr. Fysik*, 33, No.21 (1946).

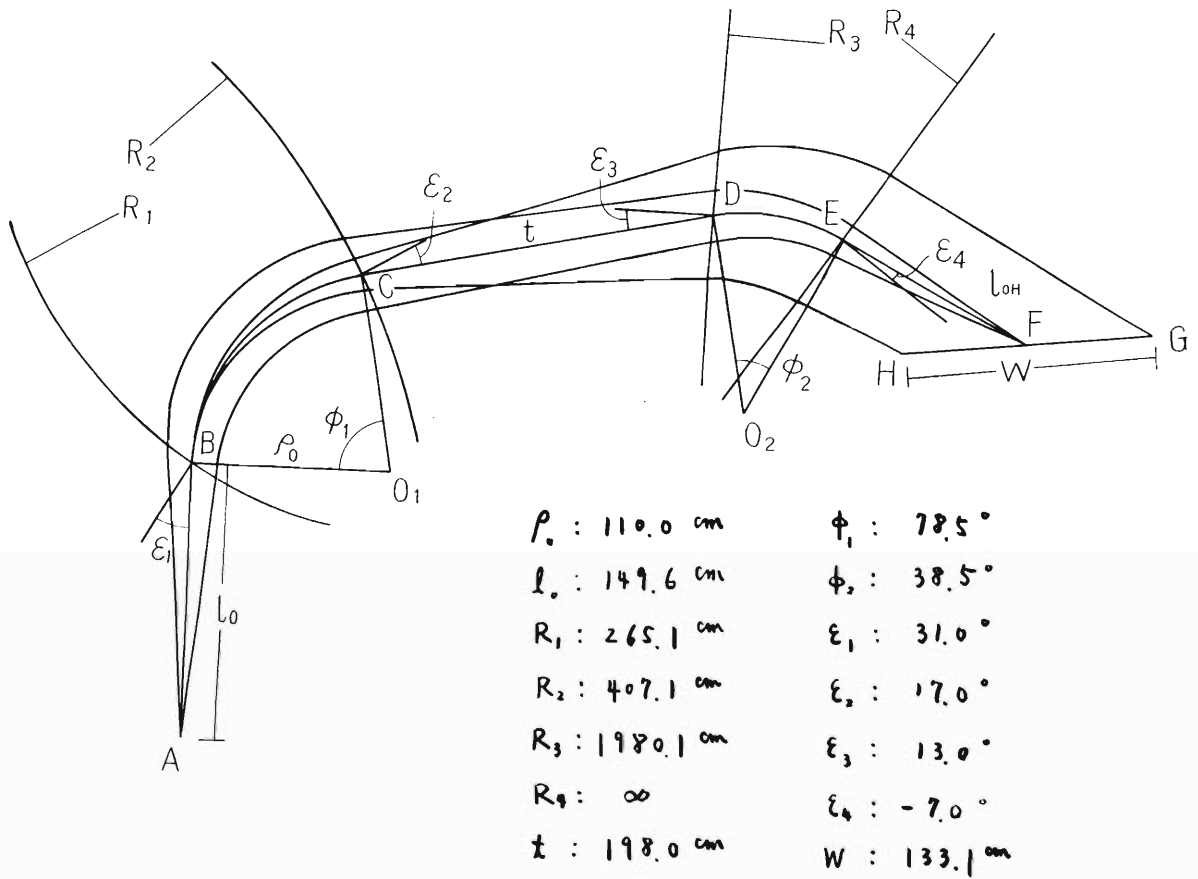


Fig. 1 (7-3). Upper drawing shows a designed magnetic field configuration in the median plane of magnets and typical particle trajectories. In the lower side calculated values are tabulated.

7-4. Data Processing System

T. Wada, Y. Chiba, K. Matsuda
and M. Yoshimizu*

As described in other section, the main features of our cyclotron are that the particle energy is variable in a wide range and that many kinds of particles are available.

Using such particles, the nuclear data are abundant and complicated. To acquire and process the data, a large multi-channel analyzer is needed. But recently the cost and the memory capacity of such analyzer do not differ substantially from those of small general purpose computers. Because of the enormous data-processing capability and the flexibility of operation, many experimenters prefer the small on-line computers to multi-channel analyzers^{1,2}.

We selected DDP-124 of Computer Control Company (now Computer Control Division of Honeywell) of U.S. A. At that time (1965), the DDP-124 was the only small computer made of IC with low cost, high speed and high reliability. The specifications of this computer are as follows:

Type

Binary, core memory, parallel, single address with indexing, and indirect addressing.

Word length

24 bits, sign/magnitude code.

Speed

Adding 3.5 μ sec.
Multiplying 14 μ sec. (avg.)

Memory

8192 words 1.75 μ sec cycle time

Input/Output

24 bits parallel buffered or unbuffered channel.
Direct memory access channel, control pulse lines, sense input lines, and priority interrupt lines.

Software

FORTRAN 4 compiler with Boolean statements,
DAP 2 Symbolic Assembly Program,
Utility Routines.

Installation

Power 3.5 kVA single phase 115 ± 10 V 60 cps.
Operating temperature 10° to 40° C.
Humidity 0 to 90 %

The plug-in type units of Technical Measurement Corporation were selected as the A/D converter of input signals, because in the case of double parameter PHA, the coincidence analysis between analogue and digital data was also intended. The digital data will be obtained from the detector array of the magnetic particle analyzer which is now

under construction.

When a computer is used as a PHA system, there are two problems, one of which is that the dead time is very long. Using a priority interrupt line and coding the program as rapid as possible, the dead time can be reduced to about 30μ sec. Because the clock pulse of A/D converter is 4 Mc, the total dead time per one input signal is $0.25N + 30\mu$ sec, where N is the channel number into which the input signal is to be sorted.

To reduce the dead time loss, the best method is to close the current integrator during the dead time of the PHA system. We are now designing this circuit.

Another problem is that the treatment of the computer is not so easy as a wired program PHA system. Hence, we have designed a PHA Control Unit, which is composed of many switches. By setting these switches same as in the case of a wired program system, the experimenter can specify any functions of PHA, for example the type of CRT display or the memory region into which the data is stored.

The computer program reads the status of each switch and accomplishes the corresponding function. Some of the switches are not read but used to interrupt the computer program or to set the sense lines. Our system has 8 level priority interrupt lines, 8 sense lines and 16 control pulse lines. The priority interrupt lines are as follows:

- # 7 spare
- # 6 Accumulate Stop
- # 5 Accumulate Start
- # 4 A/D Conversion Complete
- # 3 DMA Channel End of Range
- # 2 Data Output Start
- # 1 Data Output Stop
- # 0 spare

The power failure interrupt has the highest priority over all of these lines. The configuration of whole system is shown in Fig. 1 (7-4).

* Kyokuto Boeki Co., Ltd.

References

- 1) "On line Computers in Nuclear Research", Nucleonics Vol. 22, No. 12, (1964).
- 2) "Automatic Acquisition and Reduction of Nuclear Data", Proceedings of a Conference organized by EANDC at Karlsruhe, (1964).

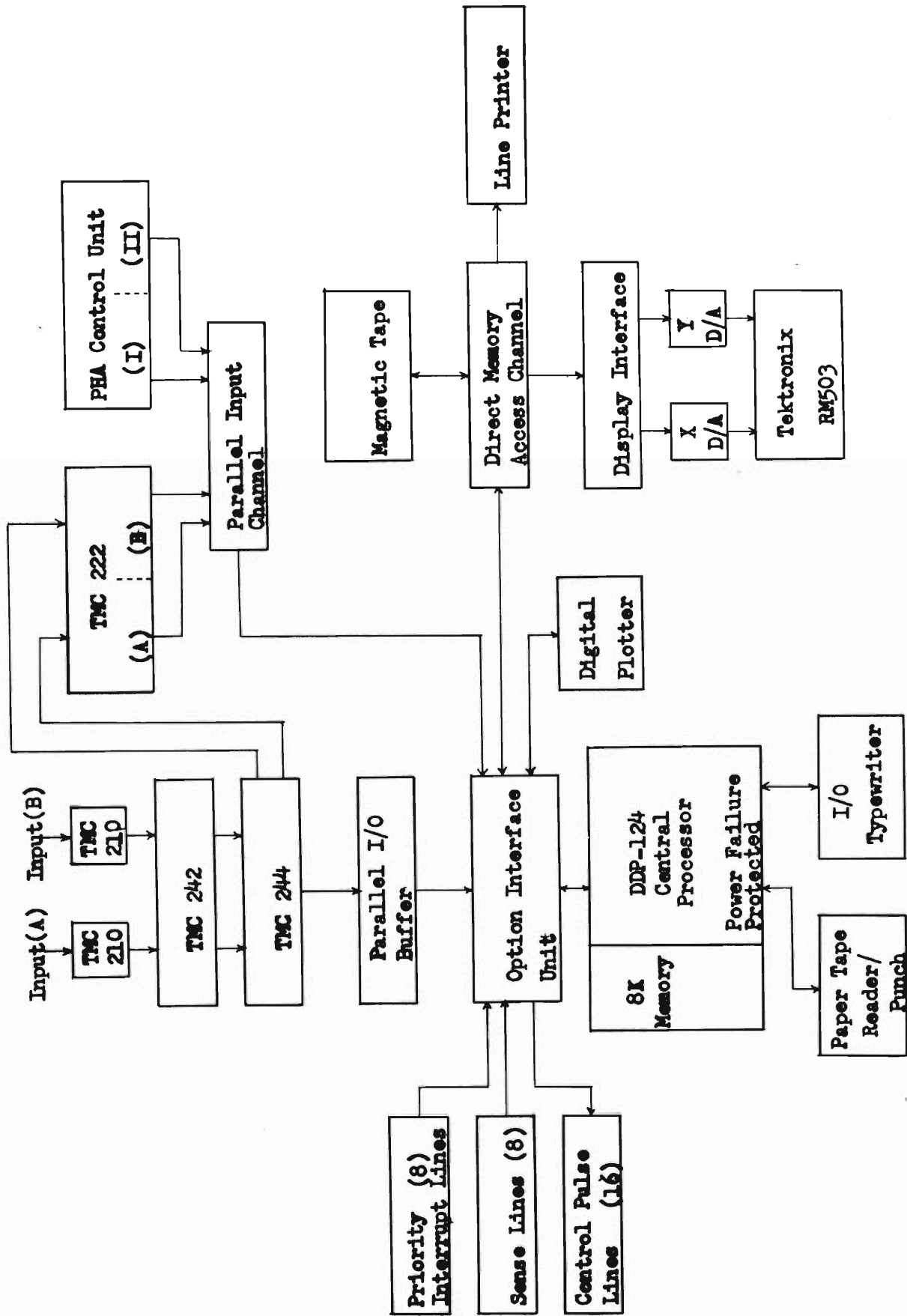


Fig. 1 (7-4). DDP-124 PHA system configuration

7-5. A Charge Spectrometer

N. Saito and M. Aratani

As one of the nuclear instruments related with the IPCR cyclotron a charge spectrometer is now under construction. It is a specially designed mass spectrometer for studying multicharged ions produced by nuclear transformations. The charge spectrometer is the first machine of this type constructed in our country. It consists of the source chamber, the differential pumping system, the analyzer and the detection system.

The source volume is one of the technical features of the charge spectrometer. It is a cone-shaped chamber of approximately 30 ℓ . Twenty-stage ring electrodes of gradually decreasing radii are installed inside the chamber in order to focus the ion beam produced in the cone without any volume effect.

The ions entering the analyzer tube through an entrance slit are deflected by means of a 90° sector magnet of 20 cm deflection radius.

The detection system is required to be of high sensitivity due to the extremely low intensity of the multicharged ion beam. Therefore, the pulse counting method using electron-multiplier is adopted.

An X-ray ionization source chamber is provided for the study of the multicharged ions artificially produced by X-ray irradiation of non-radioactive samples.

8. RADIOCHEMISTRY

8-1. Charged-particle Activation Analysis

T. Nozaki

Semiconductor silicons of various origins were analyzed for carbon by the $^{12}\text{C} (^3\text{He}, \alpha) ^{11}\text{C}$ reaction. Although beryllium and boron also give ^{11}C by the ^3He -bombardment, it was sure, from their preparation procedures and electrical properties, that the samples contained less than 10 ppb of them.

The sample disks (3 cm diameter, 0.5 mm thickness) were bombarded by a deflected ^3He -beam (22 or 14 MeV, $0.5 \sim 1 \mu\text{A}$) for about 20 min, with the beam current being integrated and read by an integrator. After 10 min, during which ^{30}P formed mainly by the $^{28}\text{Si} (^3\text{He}, p) ^{30}\text{P}$ reaction almost decayed away, the sample surface ($10 \sim 15 \mu$) was etched off to remove the possible surface contaminations. A simple equipment was devised for undertaking the HF- HNO_3 decomposition of the sample with in a closed system; two bottles of flexible polyethylene were connected by a silicone-rubber tube, one of them being used as the decomposition vessel and the other as the container of a solution of NaOH and carrier Na_2CO_3 . Air in the both bottles was squeezed out just before the decomposition, which was started by adding HNO_3 to the decomposition vessel containing the sample and HF. Gas evolving during the decomposition was caught by the NaOH, and, when the decomposition was completed, the contents of the both bottles were mixed to give an alkaline mixture. Then, CO_2 containing ^{11}C was liberated from the mixture by adding HCl and converted into BaCO_3 . The annihilation radiation from it was measured by a scintillation counter with a single channel analyzer, and the decay was followed. The carrier recovery was determined by the acid-alkali titration and found to be usually about 60%. A graphite disk was bombarded similarly but with a much lower beam flux and used as the activation standard.

When the ^3He energy was 14 MeV and the surface contaminations were carefully removed, the measured ^{11}C activities corresponded to carbon contents of less than 300 ppb, varying according to the origins of the samples. For this ^3He energy and $1 \mu\text{A}$ flux, the detection limit was several tens ppb of carbon. When the ^3He energy was 22 MeV, the ^{11}C activities were much higher, corresponding to apparent carbon contents of $7 \sim 11$ ppm for all of the seven different samples; this was due either to an unexpected occurrence of the $^{28}\text{Si} (^3\text{He}, ^{20}\text{Ne}) ^{11}\text{C}$ or $^{16}\text{O} (^3\text{He}, 2\alpha) ^{11}\text{C}$ reaction or to an incomplete removal of the surface contaminations. (With the $^{28}\text{Si} (^3\text{He}, ^{20}\text{Ne}) ^{11}\text{C}$ reaction, the threshold is 11.3 MeV, and the penetrabilities of the ^{11}C through the Coulomb barrier are of the order of 10^{-2} and 10^{-20} for the ^3He energies of 22 MeV and 14 MeV respectively.) Further efforts are now being made to establish more reliable conditions for the analytical practice and to analyze more of the samples.

8-2. Recoil Chemistry

N. Saito, F. Ambe and S. Ambe

The behavior of recoil atoms is determined by the following three factors: the type of the nuclear reaction inducing the recoil, the nature of the recoil atom itself and the physical and chemical properties of the media in which the recoil takes place. Therefore, one of the most fundamental methods of approach to recoil chemistry is to study in a systematic way the effect of the three factors on the chemical fate of the recoil atoms. From this point of view, we have been studying the recoil reaction of halogen atoms following neutron-induced nuclear reactions in halates and related compounds^{1,2}). In the present investigation, iodic acid and several iodates were irradiated with slow and fast neutrons, and the oxidation state of the recoil iodine atoms arising from the $^{127}\text{I}(n, \gamma)^{128}\text{I}$ and $^{127}\text{I}(n, 2n)^{126}\text{I}$ reactions was studied.

Fast neutrons were produced by bombarding a thick beryllium target by 16 MeV deuterons accelerated in the 160 cm cyclotron. The maximum energy of the neutrons obtained is estimated to have amounted to 19.5 MeV. The beam current of the deuterons was 0.5 – 1.5 μA . The flux of neutrons with energy higher than the threshold of the $^{127}\text{I}(n, 2n)^{126}\text{I}$ reaction was $10^7 \sim 10^8$ neutrons/cm²·sec at the site of irradiation. Slow neutrons were obtained by moderating the fast neutrons through a paraffin block 10 cm thick. The flux was $10^6 \sim 10^7$ neutrons/cm² sec. The cadmium ratio for iodine was 2.1 in this condition of irradiation, which indicates a fairly large contribution of resonance neutrons in the $^{127}\text{I}(n, \gamma)^{128}\text{I}$ reaction.

Iodic acid and iodates listed in Tables 1 and 2 (8-2) were irradiated for 1 hr. at dry ice temperature by slow or fast neutrons to induce the (n, γ) or (n, 2n) reaction, respectively. The irradiated iodic acid was dissolved in an aqueous solution containing a large excess of sodium hydroxide and the solution was neutralized carefully with dilute nitric acid. Iodates were dissolved in water. Potassium iodide or sodium periodate was added as carriers. Radioactive cations were eliminated by an ion exchange resin. Iodine atoms in lower oxidation states were separated by the precipitation of silver iodide or by the exchange extraction of molecular iodine. Periodate ions were separated as potassium periodate precipitate. The radioactivity of ^{128}I and ^{126}I was measured by means of a sodium iodide scintillation counter. In case of ^{126}I , the distribution of activity was determined from the photo peak area of 390 and 670 γ -rays to eliminate the contribution of ^{124}Sb and $^{127\text{m}}\text{Te} - ^{127}\text{Te}$ produced by fast neutrons.

The results are given in Tables 1 and 2 (8-2). The "retention" means the percentage of recoil atoms found in the chemical form identical with the starting material, in this case, the iodate ions. In all the compounds studied, almost no activity was found in the periodate fraction.

It is seen from Table 1 (8-2) that the retention of the hydrates is lower than the value for the corresponding anhydrous salts. A similar effect was reported by Saito and Tomita for arsenates³). In the anhydrous salts, cesium iodate shows an exceptionally high retention. This anomaly is thought to come from a difference in the crystal structure or the close resemblance of the mass of iodine and cesium atoms. Comparison of the data in Tables 1 and 2 (8-2) indicates that for both iodic acid and iodates the retention of the iodine recoil atoms is fairly different for the (n, γ) and

(n, 2n) reactions. This is in agreement with the report of Aten and his coworkers for potassium iodate⁴) and presents a striking contrast to our result on bromate¹). For sodium bromate almost no difference was observed between the retention for the $^{79}\text{Br}(n, \gamma)^{80}\text{Br}$ and $^{79}\text{Br}(n, 2n)^{78}\text{Br}$ reactions. A possible internal conversion process accompanying one of the nuclear reactions may have caused such difference in iodic acid and iodates.

Further work is in progress on other compounds and other nuclear reactions.

Table 1 (8-2). The Retention of ^{128}I Following the $^{127}\text{I}(n, \gamma)^{128}\text{I}$ Reaction in Iodic Acid and Iodates

Compounds	Retention
HIO_3	$50 \pm 1 \%$
LiIO_3	58 ± 1
NaIO_3	57 ± 1
$\text{NaIO}_3 \cdot \text{H}_2\text{O}$	38 ± 1
KIO_3	57 ± 1
CsIO_3	65 ± 2
$\text{Mg}(\text{IO}_3)_2$	60 ± 3
$\text{Mg}(\text{IO}_3)_2 \cdot 4\text{H}_2\text{O}$	42 ± 2

Table 2 (8-2). The Retention of ^{126}I Following the $^{127}\text{I}(n, 2n)^{126}\text{I}$ Reaction in Iodic Acid and Iodates

Compounds	Retention
HIO_3	$42 \pm 1 \%$
NaIO_3	37 ± 2
$\text{NaIO}_3 \cdot \text{H}_2\text{O}$	30 ± 1
KIO_3	39 ± 1

References

- 1) N. Saito, F. Ambe and H. Sano: *Nature*, 205, 688 (1965).
- 2) N. Saito, F. Ambe and H. Sano: *Nature*, 206, 505 (1965): N. Saito, F. Ambe and H. Sano: *Radiochim. Acta*, in press.
- 3) N. Saito and I. Tomita: *Bull. Chem. Soc. Japan*, 35, 1127 (1962).
- 4) A. H. W. Aten, Jr., M. Lindner-Groen and L. Lindner: "Chemical Effects of Nuclear Transformations", Vol. 2, p. 125, IAEA, Vienna, 1965.

9. RADIATION CHEMISTRY AND RADIATION BIOLOGY

9-1 LET Effects in the Radiation Chemistry and Radiation Biology

M. Matsui, T. Karasawa, M. Imamura, H. Seki,
K. Nakano, A. Matsuyama, and S. Kitayama

The chemical effects of radiation generally depend upon the nature of the radiation and its energy. It is called LET effect. A convenient parameter to use in characterizing various kinds of radiations is the amount of energy lost per unit distance along the track of the charged particles which constitute the radiation. This energy loss parameter, perhaps best represented by the symbol $-dE/dX$, has often been called "linear energy transfer" or LET. For the stopping of the charged particles, it is given by the Bethe formula $-dE/dX = 4\pi z^2 e^4 N Z / m v^2 \ln(2mv^2/I)$. Then LET is proportional to the electron density NZ of the sample and the square of the charge ze of particles, and increases with decreasing velocity v of particles. I is the mean excitation potential, which is $I = 66$ eV for water.

In the radiolysis of liquids, it is assumed that the primary products such as ions, free radicals and excited molecules are localized in the so-called "spur". The radiolysis of an aqueous solution was well explained by assuming the diffusion of the spur. Consequently, two types of products, i.e., "molecular" and "radical" products are considered. The former is produced by the interaction of the primary products in the spur region, and the latter is formed after homogeneous distribution of the primary products is completed. The difference in the reactions caused by the various kinds of radiations is thought to be attributed to the difference in the above-described spacial distribution of the primary products.

The irradiation of the high LET radiation is very important in view of the fundamental studies of effective utilization of atomic energy and of its effects on the living body. The studies on the LET effects carried out in our laboratories using the recoil particles have shown many interesting features. These are: (1) the increase in $G(\text{CH}_2\text{O})$ and the decrease in $G(\text{CH}_2\text{OH})_2$ with increasing LET in the radiolysis of liquid methanol, (2) the variation of the yield of solvated electrons with LET in liquid methanol, (3) that of the yield of "molecular" hydrogen from methanol and tetrahydrofuran, (4) that of $G(\text{H}_2\text{O}_2)$ from the neutral aqueous solutions containing Cl^- , and (5) the relation between LET and killing or mutational effect on microorganisms. Further studies necessitate the use of the cyclotron radiation with intermediate LET to obtain a systematic information. We have, therefore, attempted to establish a method of determination of the dose rate of these radiations using ordinary Fricke solutions in comparison with a suitable physical method.

The solutions contained 10 mM of ferrous ammonium sulfate, 1 mM of NaCl and 0.4 M of H_2SO_4 . The concentration of ferric ion was determined directly from the optical absorption at $305 \text{ m}\mu$; the molar extinction coefficient was taken as 2174 at 23.7°C .

Generally, in the experiments with an accelerator, it is important technically to have a suitable beam onto the target. Irradiation was performed through a thin glass window set on the irradiation cell, after passing a thin aluminum window and an air layer. Since the beam profile was about 3~5mm, the intensity was relatively small, $(1\sim 10) \times 10^{-9} \text{A}$, but the density became $0.2 \mu \text{A}/\text{cm}^2$.

Irradiation was made at the end of an evacuated pipe through which the deflected beam from the IPCR 160 cm cyclotron passed. Solution was magnetically stirred in the cell. The input charge in the solution was monitored by reading the current by means of a platinum wire dipped into the solution and connected to ground through a current integrator. Since no correction for the production of secondary electrons has been made in the current measurement, the result shown in Fig. 1 (9-1) is essentially relative in nature. However, this relation between the physical and the chemical measurements may be used practically with an accuracy of $\pm 10\%$. The determination of $G(\text{Fe}^{3+})$ in the radiolysis with a variety of heavy ions and ${}^3\text{He}^{++}$ (15 ~ 45 MeV), and the examination of LET effects in the radiolysis of methanol, furan and biological systems will be our main projects in the future.

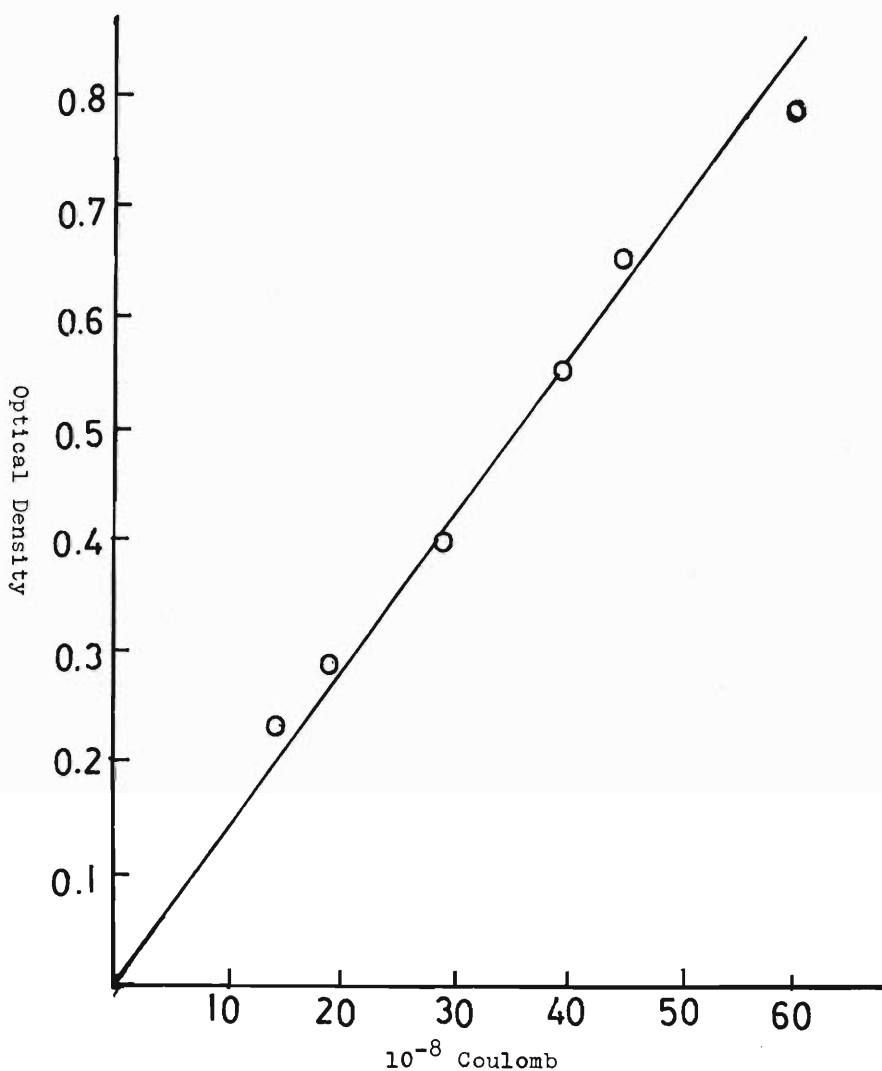


Fig. 1 (9-1) Relation between optical density (Fe^{3+}) and total charge input.

10. SOLID STATE PHYSICS

10-1. Radiation Damage in Solids

R. R. Hasiguti, M. Sugimoto, H. Sakairi,
N. Shiotani, and T. Okada

The behavior of lattice defects created by particle irradiation and their effects on material properties are the main subjects of this research.

For the present we can make experiments only at room temperature, but a cryostat for irradiation at liquid nitrogen temperature is now being prepared.

The problems to be studied in this year are as follows:

(1) Annealing process of vacancies in metals.

Quenching, a usual technique to introduce vacancies into crystals, is not adequate for the study of the annealing process of single vacancies, because some parts of quenched-in vacancies cluster during quenching. We study, therefore, the annealing process of single vacancies introduced into crystals by particle irradiation by measuring the electrical resistivity. We are also interested in interaction of vacancies with other lattice defects such as dislocations.

(2) A mechanism of swelling of irradiated metals.

Some materials irradiated by neutrons show swelling due to the formation of gas bubbles such as of helium or xenon, as products of nuclear reaction. In neutron irradiation experiments, however, detailed experimental analyses of materials are obstructed by residual radioactivity. We are going to observe the formation process of bubbles by the transmission electron microscopy, by making simulative experiments with α -particle irradiation. We consider that lattice defects such as dislocation may play an important role in the process.

(3) Damage in ferrite.

There are only a few experiments about the irradiation effects on the magnetic properties of solids. We start the study of changes of magnetic susceptibility and coercive force of ferrimagnetic ferrites by particle irradiation.

11. RI PRODUCTION AND ITS APPLICATIONS

11-1. The Irradiation System

A. Hashizume and A. Shimamura

The ever-increasing interest in cyclotron produced radio-isotopes has necessitated an irradiation system. To minimize the irradiation hazards in RI handling, it is desirable to treat this system by remote control.

These radio-isotopes lie in general on the neutron deficient side of the nuclear stability line, in contrast to the nuclei formed by neutron capture or as fission products. They are usually of chemical elements different from those of the targets. So we can obtain by suitable chemical techniques the high specific activity which can accede to the demands in various parts.

For handling automatically the RI target system, a problem arises regarding the removal of intensely radioactive targets from the vacuum chamber of the cyclotron. We have constructed a target system in which the target can be withdrawn from the vacuum chamber and demounted from the cooling system by remote control. The target-mounting assembly is attached to a cylinder which has hydraulic pipes. This cylinder brings the target by a screw mechanism to a proper position of the beam in the cyclotron and withdraws it at the end point of bombardment. The target can be removed by another screw mechanism. This withdrawing or removing operation of the target can be done at the control room of the cyclotron. Thus there occurs no irradiation hazard.

Before attaching the system to the cyclotron, the cooling efficiency has been tested by setting a 1 kW heater on the target position. No appreciable rise of temperature was observed in the aluminum plate which was cooled with water. A bombardment of alpha-particles of 30 MeV with 15 μ A has been safely carried out. We are going to test the maximum thermal capability of the target by using ion beams. Fig. 1 (11-1) illustrates the target system.

The construction of a transport system of the irradiated targets by remote control to the next room where the chemical handling can be done is in project.

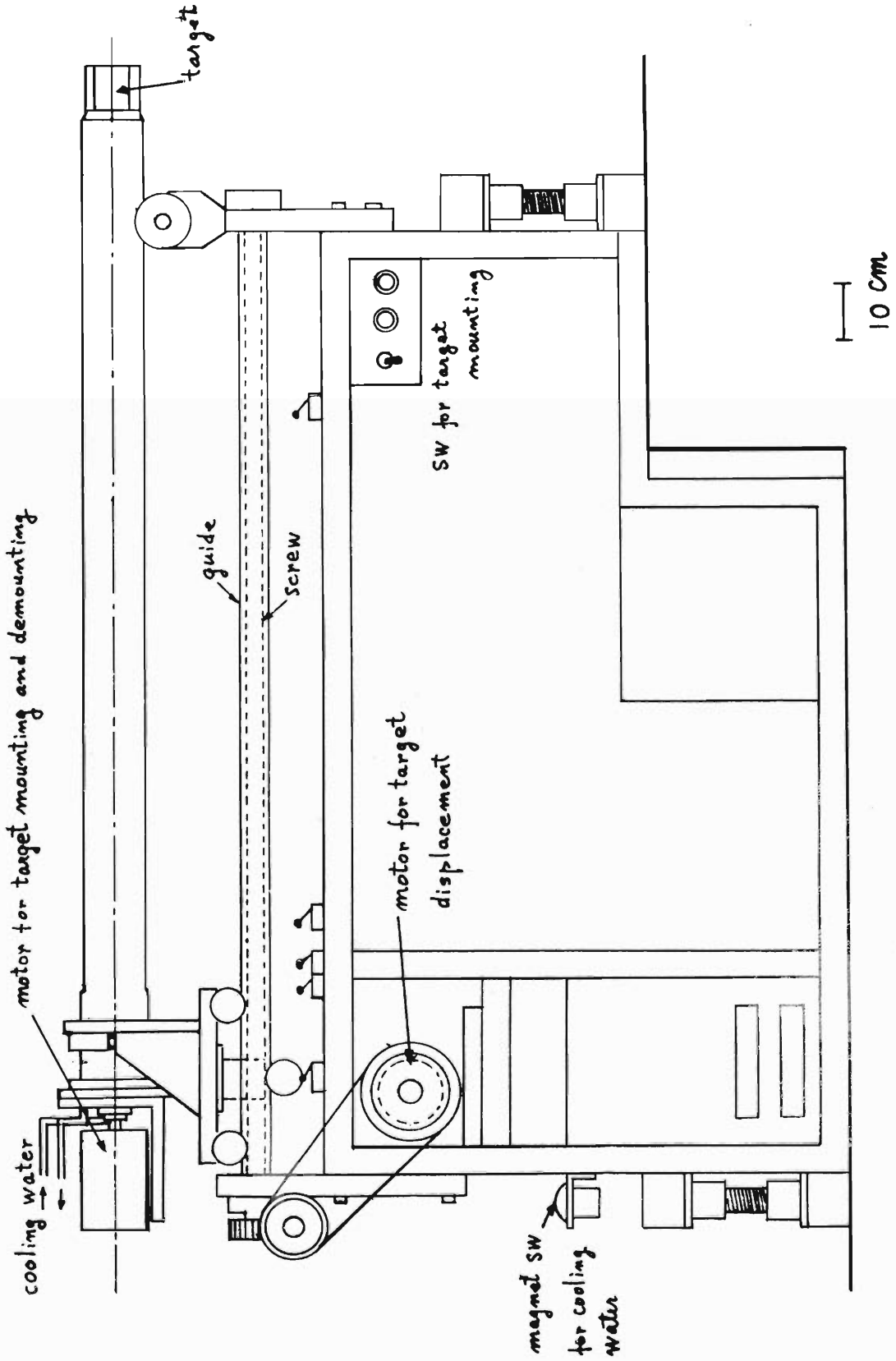


Fig. 1 (11-1) Irradiation system for RI production.

11-2. Safe Handling of Irradiated Targets

T. Hamada and T. Nozaki

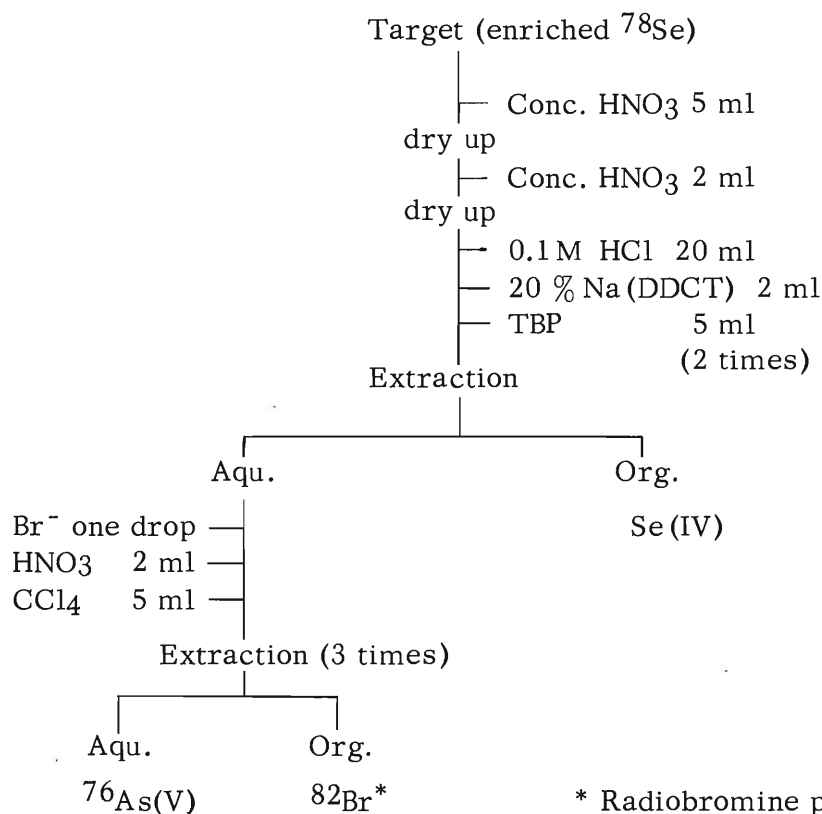
A hot cell of 3.90 m wide x 1.05 m long x 1.85 m high, consisting of three compartments, has been designed and its construction is under way. The irradiated target is carried remotely from the cyclotron room into one of the compartments by a transfer system, removed from the holder with ball-joint manipulators and processed in the neighboring two compartments. Gamma activity of up to 50 mC of Na-24 equivalent will be handled safely in the cell.

11-3. Preparation and Isolation of Carrier-free ^{76}As from ^{78}Se

M. Inarida

The present paper deals with the radiochemical isolation of carrier-free ^{76}As produced by bombarding ^{78}Se with 14 MeV deuteron-particles.

The target composed of enriched ^{78}Se metal powder wrapped in a $10\ \mu$ thick nickel foil was bombarded for 15 min at a beam intensity of $0.5\ \mu\text{A}$ with 14 MeV deuterons by the 160-cm cyclotron. After bombardment, 20 mg of the target were dissolved in 5 ml concentrated HNO_3 . The separation method of carrier-free ^{76}As from ^{78}Se is schematically shown as follows:



* Radiobromine produced by the reaction of deuterons with ^{82}Se in the target.

The activity in the carrier-free arsenic fraction was identified by the 26.5-hour half-life and by the 0.559 and 1.22 MeV gamma-rays reported for ^{76}As .

11-4. Preparation of ^{18}F -labelled Compounds

T. Nozaki

Anhydrous H^{18}F was prepared very efficiently by the ^3He - or α -bombardment of an oxygen gas stream to produce ^{18}F and the occasional elution of the ^{18}F with gaseous HF. The ^{18}F formed in the stream is adsorbed almost quantitatively on the inner surface of the bombardment vessel and eluted easily by gaseous HF mixed with the oxygen stream to give H^{18}F . Hence, the bombardment can be continued throughout the elution. Fig. 1 (11-4) gives the yields of ^{18}F calculated from the reported excitation functions, and Figs. 2 and 3(11-4) show the block diagram of the equipment and an elution curve of ^{18}F respectively. A more detailed report will be published in the Int. J. Appl. Radiat. Isotopes.

The bombardment of a streaming gas target, in general, has the following advantages; (1) a gas target has a much larger surface area for cooling than a solid target, (2) the stream itself continuously carries away the evolved heat and radiation-produced substances (e.g. O_3), and (3) any gaseous substance (e.g. anhydrous HF) can be transported through the bombardment vessel with the stream. Thus, the bombardment technique is also useful for preparing many kinds of ^{18}F -labelled compounds including fluorosteroids- ^{18}F and benzotrifluoride- ^{18}F .

Studies are now being undertaken to prepare cholesteryl fluoride- ^{18}F ; a suspension of AgF in acetonitrile is added to a silver bombardment vessel adsorbing ^{18}F and, after shaking the vessel for 20 min, cholesteryl iodide dissolved in xylene is added to the vessel and made to react with the Ag^{18}F to give the desired product. Crude cholesteryl fluoride- ^{18}F can thus be obtained with a satisfactory yield, but its purification involves some difficulty which should be overcome in future. Benzotrifluoride- ^{18}F has been obtained quite satisfactorily by the following procedure: (1) the inside of a polyethylene bombardment vessel is coated with SbF_3 by evaporating up its ethanolic solution, (2) the oxygen stream is ^3He -bombarded in the vessel, and (3) the SbF_3 labelled spontaneously with ^{18}F is collected mechanically and made to react with benzotrifluoride to give benzotrifluoride- ^{18}F .

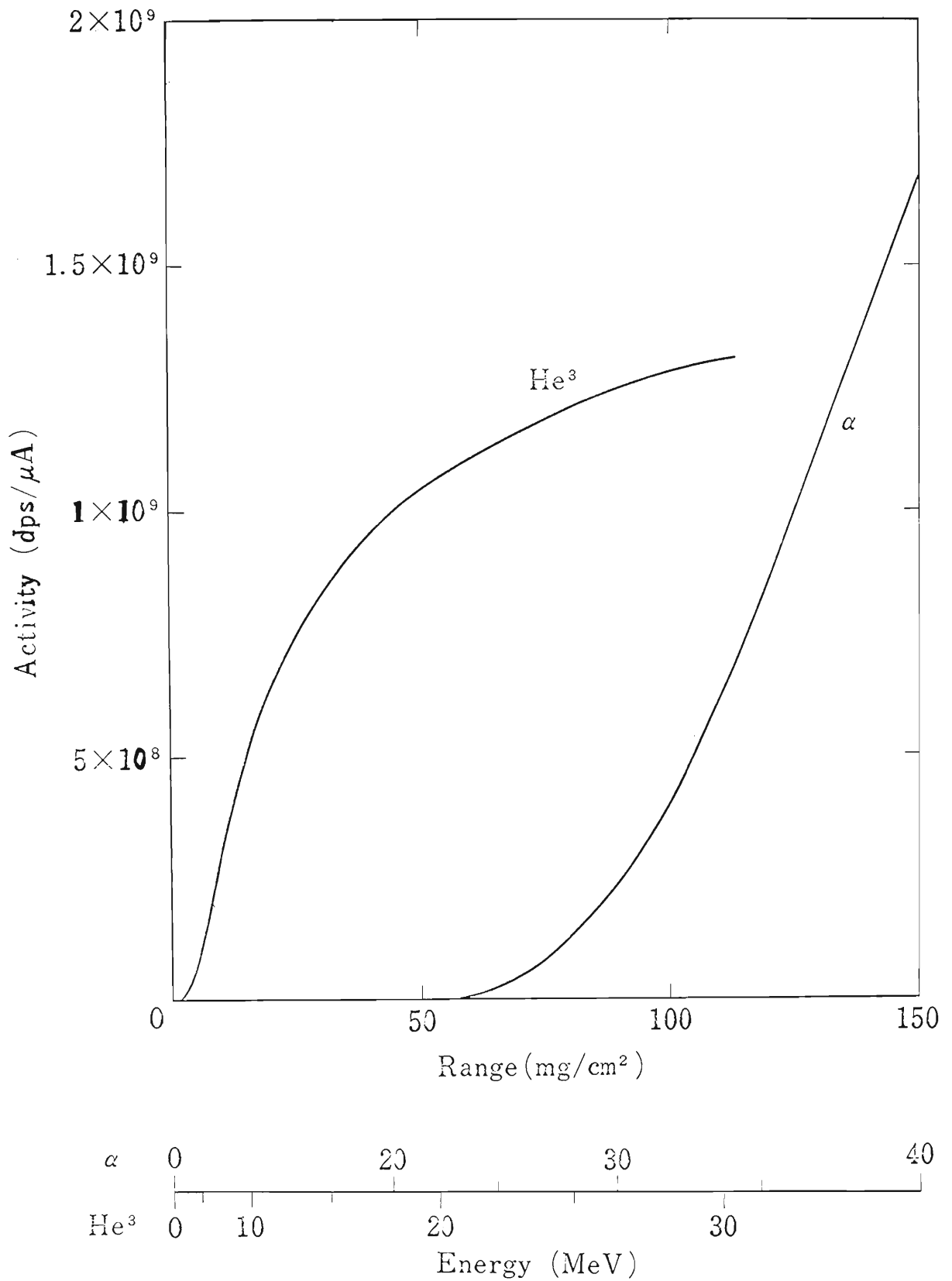
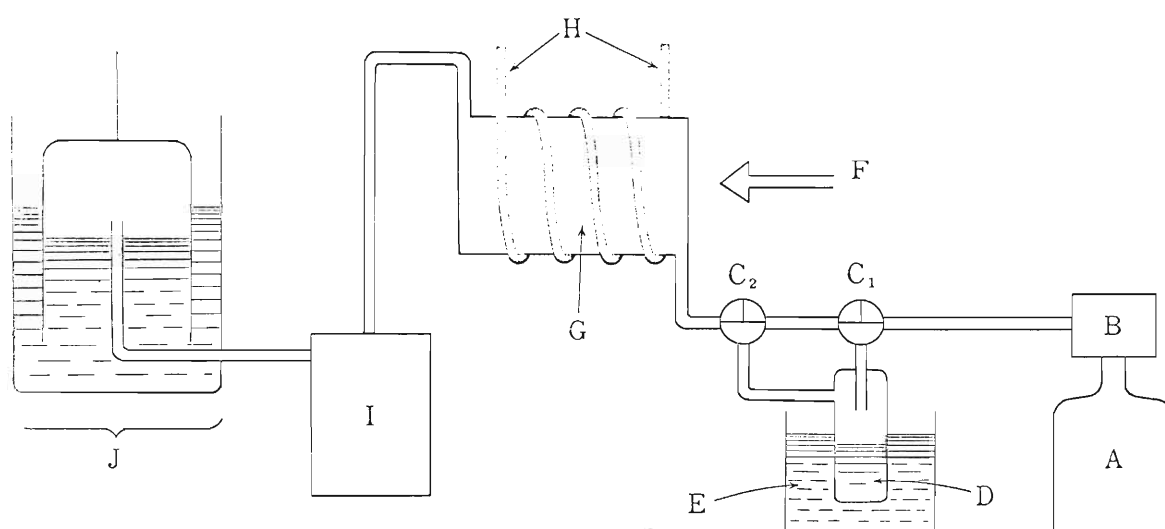
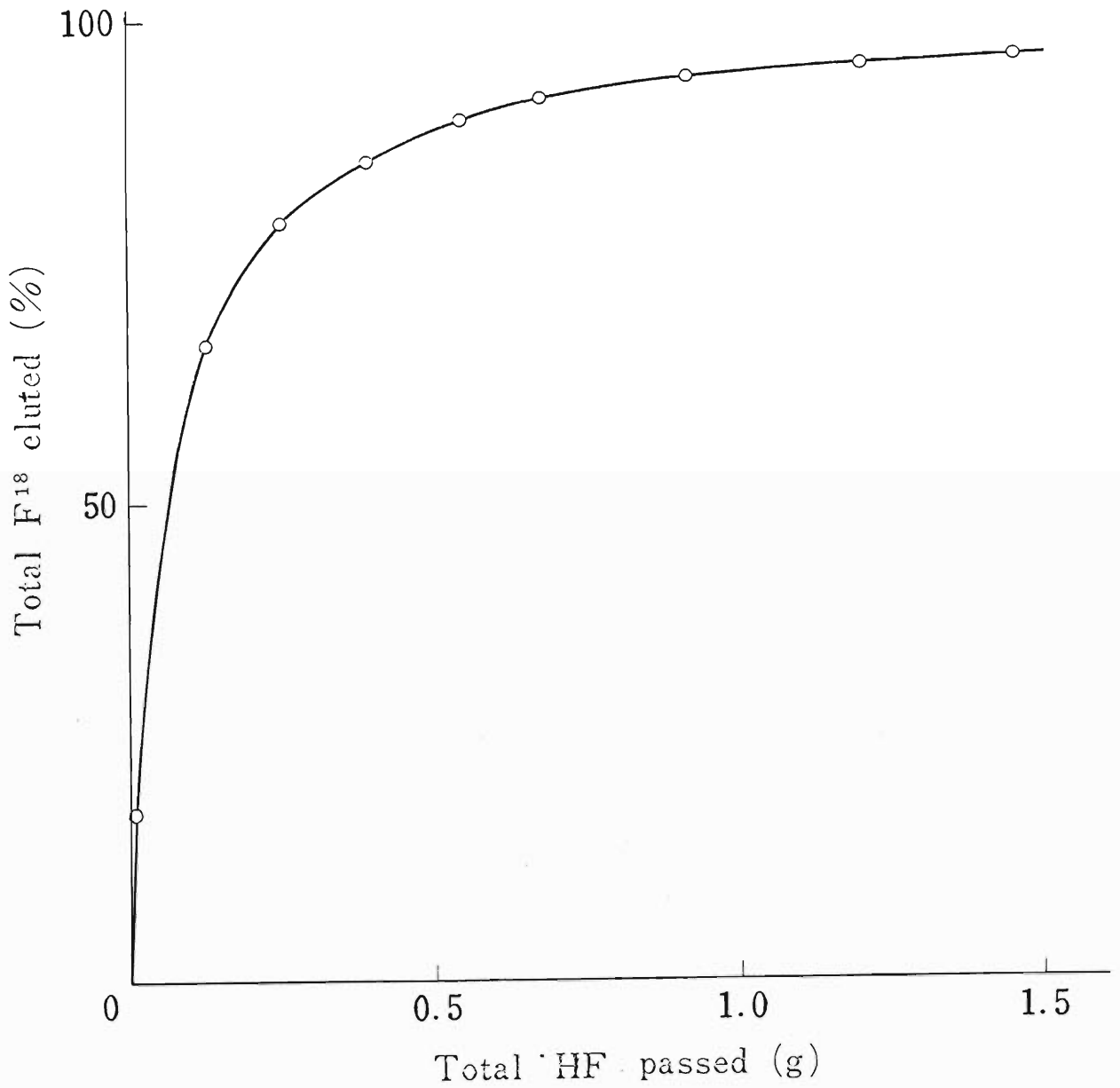


Fig. 1 (11-4). Thick-target saturation activities for the $^{16}\text{O} + \alpha \rightarrow ^{18}\text{F}$ and the $^{16}\text{O} + ^3\text{He} \rightarrow ^{18}\text{F}$ reactions in O_2 .



A: Oxygen cylinder, B: Flow-rate controller and flow-rate meter, C: Cock, D: HF reservoir, E: Bath, F: Charged-particle beam, G: Bombardment vessel, H: Cooling-water tube, I: Cold trap, J: Waste-gas reservoir.

Fig. 2 (11-4). Equipment for preparing anhydrous H^{18}F by charged particle bombardment of an oxygen stream.



Vessel size: 2 x 7 x 20 cm

Flow rate : O₂, about 150 ml/min; HF, about 0.1 g/min.

Fig. 3 (11-4). Elution curve of H¹⁸F from a silver bombardment vessel.

12. RADIATION MONITORING

12-1. Radiation Monitoring Station

T. Hamada, M. Okano and M. Ota

A radiation monitoring station has been built at about 85 m apart from the cyclotron and operated since Oct. 1966.

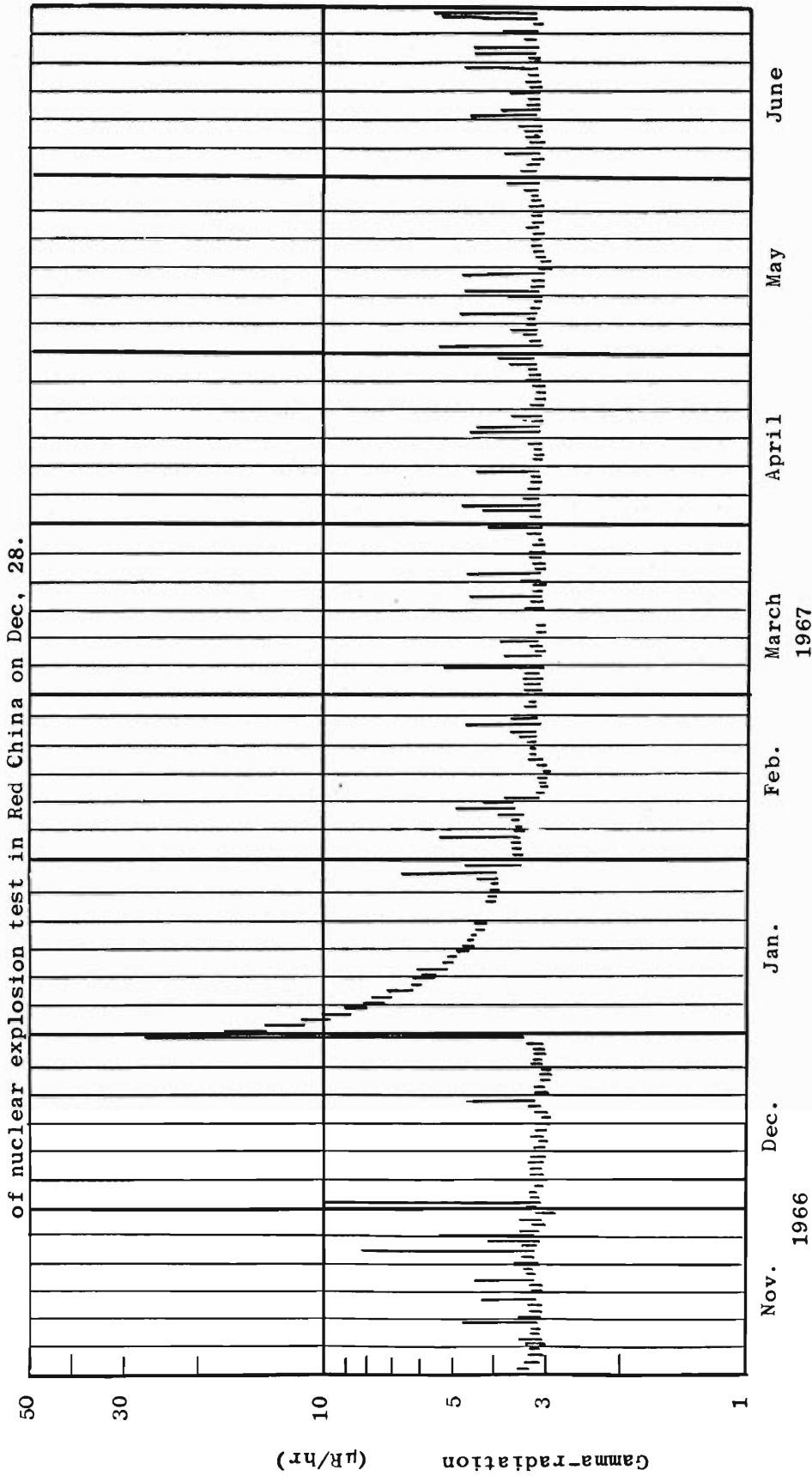
Two scintillation detectors and a BF₃ counter are used to measure the radiation level at that position. One of the scintillation detectors is a 1~1/2 in ϕ x 1~1/2 in NaI(Tl) which has a compensation shield specially designed for the gamma-ray dose measurement. The other is a 3 in ϕ x 3 in NaI(Tl) which is used for spectroscopic analysis of gamma-rays. The analysis is considered to be essential to distinguish the radiations leaking from the cyclotron room and other artificial sources from those of the natural background.

The BF₃ counter has effective dimensions of 50 mm ϕ x 236 mm and is filled with enriched BF₃ gas at 600 mm Hg, covered with 1 mm Cd and 10 cm paraffin, and made sensitive only to fast neutrons.

The pulses from the small scintillation detector and the BF₃ counter are fed to the scaler and the counts, scaled down to 1/100 and 1/10 respectively, and printed at 15 min intervals.

A record of monitoring during the period from Nov. 1966 to June 1967 is shown in the figure, where the radiation level is given in the unit of μ R/h which includes the contribution of soil radioactivity (2.5 μ R/h) as well as the apparent dose rate equivalent to 0.6 μ R/h due to cosmic rays and the detector contamination.

The leakage radiations from the cyclotron were not detected during this period, while the radioactive fallout due to the nuclear explosion test in Red China on Dec. 28, 1966, was sharply detected as indicated in the figure.



Each bar represents the range of variation of the dose rate during 24 hrs. Higher dose rates observed from time to time are due to radon daughters falling down with rain or snow. The sudden increase on Dec. 30, 1966, and the following decay indicate the effect of nuclear explosion test in Red China on Dec. 28.

Fig. 1 (12-1). Record of radiation monitoring at the station 85 m apart from the cyclotron

12-2. Health Physics

K. Koda and I. Sakamoto

(1) Radiation Shielding

The shield walls provided for the IPCR cyclotron and the associated equipments are made of ordinary concrete 1.0 ~ 2.3 m thick and able to keep the outside radiation levels (gamma-rays plus neutron) below the values permissible to non-occupational people even when a thick Be target is bombarded by 200 μ A beam of 25 MeV deuterons. The entrances to the cyclotron room and the experimental areas are equipped with shielding water tanks. The cyclotron rooms and the experimental areas are accessible from the control room through an underground passage.

In the early stage of test working, rather high radiation levels as much as $10^3 \sim 10^4$ cpm of fast neutrons and 10 mR/h of gamma rays were observed at a point of the underground passage, that is in the vicinity of the loopholes and the shielding doors. Shielding was somewhat increased afterwards and the latest data show satisfactory results as given in Fig. 1 (12-2). The results imply that in this case the main radiation source is the cyclotron and not the target.

(2) Residual Activity

A dose map of the controlled area measured 3 hrs after machine shutdown is shown in Figs. 2 and 3 (12-2). In Fig. 2 (12-2), it is shown that the cyclotron itself, the slits and the beam stopper are the main radiation sources. The surface dose rate of the beam stopper was 100 mR/h just after machine shutdown, falling to 80 mR/h after 6 min. The nature of the induced radio-nuclide is not yet identified. Fig. 3 (12-2) shows the residual dose rate distribution around the cyclotron. Higher dose rate near the stairs are due to the solid wastes stored there.

(3) Contamination

"Dusting-off" of loose surface contamination ($2 \times 10^{-6} \mu\text{C} / \text{cm}^2$ beta + gamma) has been observed only on the floor near the cyclotron.

(4) Personnel Monitoring

The gamma film badge was issued to all staffs and some of them had a pocket dosimeter which indicated the sum of fast neutron and gamma dose. Table 1 (12-2) shows the accumulated dose distribution of the staffs during 6 months.

Table 1 (12-2). Accumulated dose distribution of the staffs
from Oct. '66 to Mar. '67

Rank of Accumulated dose	A	B	C	D	E
No. of staffs	2	10	3	6	1

Average dose per person: 85 mrem

Maximum dose: 370 mrem

Rank A: undetectable, B: 10 ~ 180 (mrem), C: 61 ~ 220 (mrem),
D: 101 ~ 420 (mrem), E: more than 300 (mrem).

(THIS INCLUDES 0.02 mR/h BACKGROUND RADIATION.)
 (MEASURED ON MAY 8 '67.)

OPERATING CONDITIONS.
 $E\alpha = 29 \text{ Mev}$
 BEAM COURSE #5
 TARGET: SILICA

DOSE UNIT.
 NEUTRON = CPM (UNDERLINE)
 GAMMA = mR/h

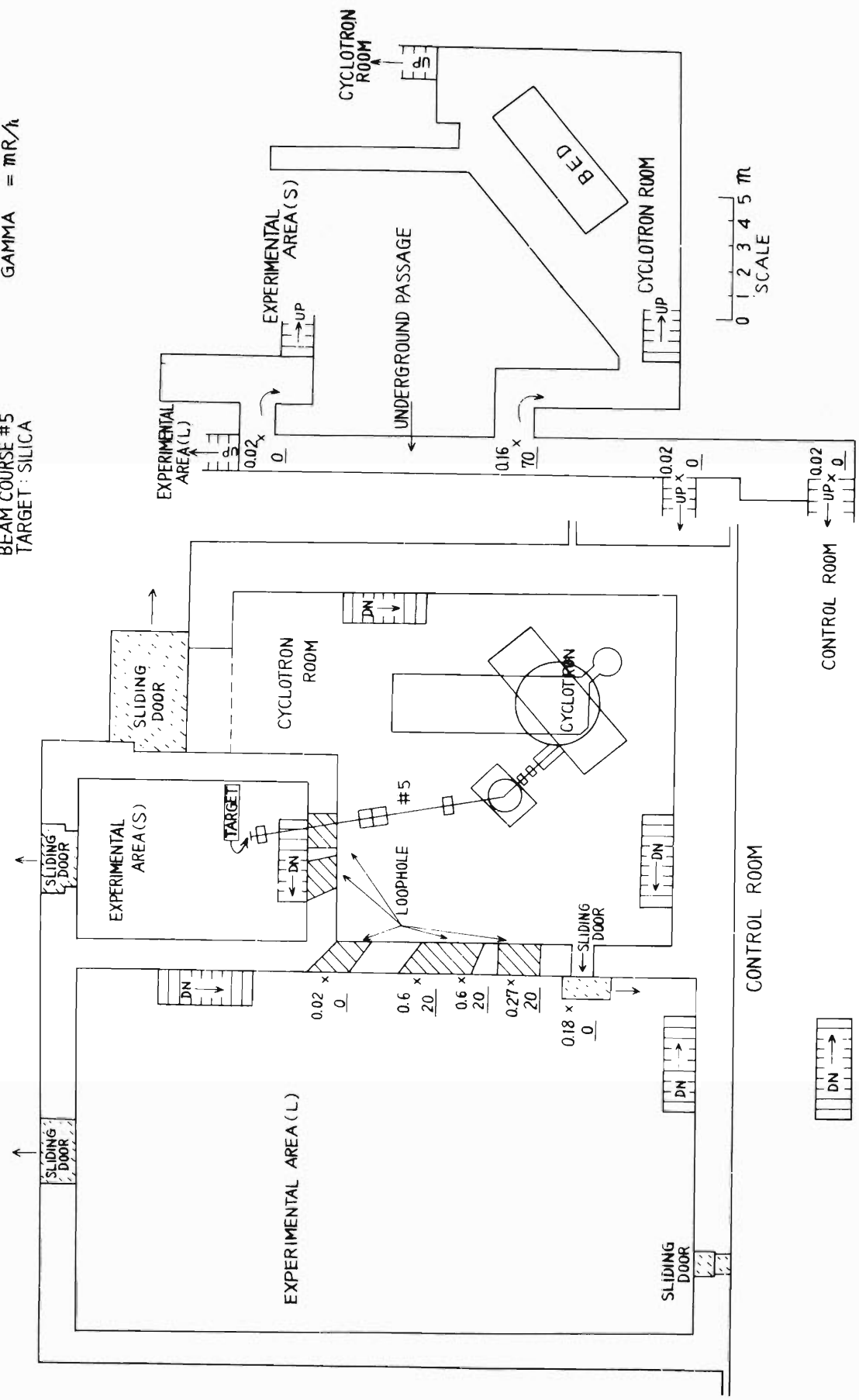


Fig. 1 (12-2) Machine leakage radiation (neutron and gamma).

13. LIST OF PERSONNEL

the IPCR Cyclotron Construction Committee

熊谷寛夫	Hiroo KUMAGAI (chairman)
千谷利三	Toshizo TITANI
橋口隆吉	Ryukiti R. HASIGUTI
菊池正士	Seishi KIKUCHI
野中到	Itaru NONAKA
斉藤信房	Nobufusa SAITO
瀬藤象二	Shoji SETO
篠原健一	Kenichi SHINOHARA
菅義夫	Yoshio SUGE
柘植芳男	Yoshio TSUGE
山崎文男	Fumio YAMASAKI

the IPCR Cyclotron Administration Committee

山崎文男	Fumio YAMASAKI (chairman)
橋口隆吉	Ryukiti R. HASIGUTI
熊谷寛夫	Hiroo KUMAGAI
今村昌	Masashi IMAMURA
唐沢孝	Takashi KARASAWA
松田一久	Kazuhisa MATSUDA
松山晃	Akira MATSUYAMA
斉藤信房	Nobufusa SAITO
杉本光男	Mitsuo SUGIMOTO
田中穰	Yutaka G. TANAKA

Managers of Users Group

浜田達二	Tatsuji HAMADA
小寺正俊	Masatoshi ODERA

the IPCR Cyclotron Constructing Personnel

Leader

熊谷寛夫 Hiroo KUMAGAI

Magnet

元永昭七	Shoshichi MOTONAGA,	唐沢孝	Takashi KARASAWA
逸見政武	Masatake HEMMI,	宮沢佳敏	Yoshitoshi MIYAZAWA
中西紀喜	Noriyoshi NAKANISHI		

Oscillator

小寺正俊	Masatoshi ODERA,	千葉好明	Yoshiaki CHIBA
藤沢高志	Takashi FUJISAWA,	寺島為	Osamu TERASHIMA

Vacuum System

唐沢孝	Takashi KARASAWA,	宮沢佳敏	Yoshitoshi MIYAZAWA
戸沼正雄	Tadao TONUMA	吉田喜作	Kisaku YOSHIDA

Ion Source

河野功	Isao KOHNO,	中島諄二	Shunji NAKAJIMA
戸沼正雄	Tadao TONUMA		

Control

河野功	Isao KOHNO,	井上敏彦	Toshihiko INOUE
竹田繁	Shigeru TAKEDA		

Beam Transport

上坪宏道	Hiromichi KAMITSUBO,	逸見政武	Masatake HEMMI
松田一久	Kazuhisa MATSUDA,	元永昭七	Shoshichi MOTONAGA
中西紀喜	Noriyoshi NAKANISHI		

RI System

浜田達二	Tatsuji HAMADA,	橋爪朗	Akira HASHIZUME
野崎正	Tadashi NOZAKI,	島村旻	Akira SHIMAMURA

General Management

浜田達二	Tatsuji HAMADA,	松田一久	Kazuhisa MATSUDA
------	-----------------	------	------------------

the IPCR Cyclotron Operating Personnel

Management

唐沢孝	Takashi KARASAWA,	小寺正俊	Masatoshi ODERA
元永昭七	Shoshichi MOTONAGA,	河野功	Isao KOHNO
宮沢佳敏	Yoshitoshi MIYAZAWA		

Operator

藤田新	Shin FUJITA,	池上九三男	Kumio IKEGAMI
中島尚雄	Hisao NAKAJIMA,	萩原清	Kiyoshi OGIWARA
大沢信道	Nobumichi OSAWA,	寺島為	Osamu TERASHIMA
吉田喜作	Kisaku YOSHIDA		

Scientific and Engineering Personnel

Cyclotron Lab.

熊谷寛夫	Hiroo KUMAGAI,	千葉好明	Yoshiaki CHIBA
藤沢高志	Takashi FUJISAWA,	藤田二郎	Jiro FUJITA
逸見政武	Masatake HEMMI,	井上敏彦	Toshihiko INOUE
上坪宏道	Hiromichi KAMITSUBO.	唐沢孝	Takashi KARASAWA
河野功	Isao KOHNO,	松田一久	Kazuhisa MATSUDA
宮沢佳敏	Yoshitoshi MIYAZAWA,	元永昭七	Shoshichi MOTONAGA
中島諄二	Shunji NAKAJIMA,	中西紀喜	Noriyoshi NAKANISHI
小寺正俊	Masatoshi ODERA,	島村旻	Akira SHIMAMURA
竹谷繁	Shigeru TAKEDA,	戸沼正雄	Tadao TONUMA
和田雄	Takeshi WADA		

Radiation Lab.

山崎文男	Fumio YAMASAKI,	粟屋容子	Yohko AWAYA
浜田達二	Tatsuji HAMADA,	橋爪朗	Akira HASHIZUME
稲村卓	Takashi INAMURA,	加藤武雄	Takeo KATO
岡野真治	Masaharu OKANO,	太田光子	Mitsuko OTA
天道芳彦	Yoshihiko TENDOW		

Analytical Chemistry Lab.

斉藤信房	Nobufusa SAITO,	荒谷美智	Michi ARATANI
野崎正	Tadashi NOZAKI		

Nuclear Chemistry Lab.

斉藤信房	Nobufusa SAITO,	安部文敏	Fumitoshi AMBE
安部静子	Shizuko AMBE,	稻荷田万里子	Mariko INARIDA

Geochemistry Lab.

島誠	Makoto SHIMA,	天野貞代	Sadayo AMANO
岡田昭彦	Akihiko OKADA		

Biochemistry I Lab.

田中穰	Yutaka G. TANAKA		
-----	------------------	--	--

Radiobiology Lab.

松山晃	Akira MATSUYAMA,	服部行彦	Yukihiko HATTORI
北山滋	Shigeru KITAYAMA		

Radiation Chemistry Lab.

今村昌	Masashi IMAMURA,	松井正夫	Masao MATSUI
中野和城	Kazushiro NAKANO,	関博之	Hiroshi SEKI

Microbiology Lab.

賀田恒夫 Tsuneo KADA

Metal Physics Lab.

橋口隆吉 Ryukiti HASIGUTI,
坂入英雄 Hideo SAKAIRI,

岩崎邦彦 Kunihiro IWASAKI
塩谷亘弘 Nobuhiro SHIOTANI

Magnetic Materials Lab.

杉本光男 Mitsuo SUGIMOTO,

岡田卓也 Takuya OKADA

Precision Engineering Lab.

水野万亀雄 Makio MIZUNO

Plastic Working Lab.

宮内邦雄 Kunio MIYAUCHI

Radiation Monitors

甲田陸男 Kugao KOODA,

坂本一郎 Ichiro SAKAMOTO

Editors of the Progress Report

松田一久 Kazuhisa MATSUDA,
田中穰 Yutaka G. TANAKA

野崎正 Tadashi NOZAKI

IPCR Cyclotron Progress Report 1967

理化学研究所サイクロトン年次報告 第1巻(1967) 奥付

印刷 昭和42年(1967) 11月25日

発行 昭和42年(1967) 11月30日

発行者 理化学研究所

代表者 赤 堀 四 郎

埼玉県北足立郡大和町大字下新倉4775番地

電話 0484-62 1111番

編集者 理化学研究所サイクロトン運営委員会

委員長 山 崎 文 男

印刷所 有限会社 丸 星 印 刷 社

東京都千代田区神田神保町1-42

定価 1,000円

理化学研究所

埼玉県 北足立郡 大和町